工學博士學位論文

Fabrication of Multidimensional Metal/Conducting Polymer Hybrid Nanoparticles and Their Chem/Bio Sensor Applications

다차원구조 금속/전도성 고분자 하이브리드 나노입자의 제조 및 화학/바이오 센서로의 응용

2015年 8月

서울大學校 大學院

化學生物工學部

李 準 燮

Fabrication of Multidimensional Metal/Conducting Polymer Hybrid Nanoparticles and Their Chem/Bio Sensor Applications

다차원구조 금속/전도성 고분자 하이브리드 나노입자의 제조 및 화학/바이오 센서로의 응용

指導敎授: 張 正 植

이 論文을 工學博士 學位論文으로 提出함

2015年 6月

서울大學校 大學院

化學生物工學部

李 準 燮

李準燮의 工學博士 學位論文을 認准함

2015年 6月

委 員 長 趙 在 英 (인)

副委員長 張 正 植 (인)

委 員 李 鍾 贊 (인)

委 員 金 榮 奎 (인)

委 員 林 淳 皓 (인)

Fabrication of Multidimensional Metal/Conducting Polymer Hybrid Nanoparticles and Their Chem/Bio Sensor Applications

by

Lee Junseop

Submitted to the Graduate School of Seoul National University

in Partial Fulfillment of the Requirements

for the Degree of Doctor of Philosophy

August, 2015

Thesis Adviser: Jang Jyongsik

ABSTRACT

In recent decades, the synthesis of novel materials with improved properties and performance is a continually expanding frontier at the material science. In this regard, hybrid nanomaterials, composed of organic/inorganic hybrid, exhibit beneficial properties originated from each component and satisfy economical and environmental challenges of industry. Among diverse hybrid nanomaterials, metal-containing polymer hybrid nanomaterials are great interest in various applications including energy storage system, catalyst, and sensing device. Although various preparation methods have been devoted to the synthesis of metal/polymer hybrid nanomaterials, there is still lack of studies on the maximization surface area of nanomaterials through morphology control.

This dissertation describes the fabrication of diverse multidimensional metal/conducting polymer hybrid nanoparticles with facile approaches and characterizes of as the prepared hybrid materials for sensor transducer application. Firstly, multidimensional FeOOH nanoneedle-decorated hybrid polypyrrole nanoparticles (PFFs) were fabricated using dual-nozzle electrospray and heat stirring steps for ultrasensitive nerve agent simulant

(DMMP) chemical sensor. Multidimensional urchin-like polypyrrole (U_PPy) hybrid nanoparticles were fabricated through pyrrole monomer vapor deposition polymerization (VDP) of the PFFs and applied as hazardous gas (NH_3/MeOH) chemical sensor. Aptamer-functionalized multidimensional carboxylated polypyrrole nanoparticles (A_M_CPPyNPs) were synthesized by using 3-carboxylated pyrrole monomer VPD on the PFFs surface and binding aptamer functionalization for sensing endocrine disruptor (bisphenol A) molecule. Secondly, multidimensional noble metal architecture decorated conducting polymer nanoparticles also suggest by using chemical reduction process. Multidimensional platinum particle decorated carboxylated polypyrrole nanoparticles (Pt_CPPys) were fabricated through chemical process using reducing agent ($NaBH_4$) for detecting neurotransmitter molecule (dopamine). Multidimensional porous palladium architecture decorated carboxylated polypyrrole nanoparticles (M_PdCPPys) were also synthesized through alkylation and following reduction process to apply hydrogen gas detect sensing system.

This dissertation provides the possibility of various types of metal/conducting polymer hybrid nanomaterials exhibited maximizing surface

area through multidimensional architecture. The nanomaterials presented in this dissertation could be applied diverse sensing systems such as hazardous gas chemical sensor, non-enzyme field-effect-transistor (FET) sensor, and aptamer FET sensor. In addition, this dissertation suggests innovative methodological insight to simple preparation of various nanomaterials.

KEYWORDS: conducting polymers; inorganic; noble metal; metal oxide; hybrid nanomaterial; sensor; hydrogen; nerve agent; dopamine; endocrine disruptor

STUDENT NUMBER: 2010–24101

List of Abbreviations

6F : 4,4’-(hexafluoroisopropylidene)diphenol

A : adenine

AA : ascorbic acid

AAO : aluminium oxide

A_CPPyNP : alkyl functionalized carboxylated polypyrrole nanoparticle

Ag : silver

A_M_CPPyNP : binding aptamer-functionalized multidimensional carboxylated polypyrrole nanoparticle

APS : 3-aminopropyltrimethoxysilane

Au : gold

BET : Brunauer-Emmett-Teller

BP : 4,4’-bisphenol

BPA : bisphenol A or 4,4’-(isopropylidene)diphenol

BPB : bisphenol B or 4,4’-(1-methylpropylidene)diphenol

C : cytosine

C6 : hexyl carbonyl

C10 : decyl carbonyl

C16 : hexadecyl carbonyl

CPPy : carboxylated polypyrrole

CPPyNP : carboxylated polypyrrole nanoparticle

$CuCl_2$: copper(II) chloride

DA : dopamine

DCNP : diethyl cyanophosphonate

DCP : diethyl chlorophosphonate

DEPC : diethyl pyrocarbonate

DMMP : dimethyl methylphosphonate

DMT-MM : 4-(4,6-dimethoxy-1,3,5-triazin-2-yl)-4-methyl-morpholinium chloride

ED : endocrine disruptor

EDX : energy dispersive X-ray

EELS : electron energy loss spectroscopy

EP : epinephrine

ER : estrogen receptor

fcc : face-centered-cubic

$FeCl_3$: iron (III) chloride

FE-SEM : field-emission scanning electron microscopy

FET : field-effect-transistor

G : guanine

GC-MS : gas chromatography coupled with mass spectrometry

HPLC : high-pressure liquid chromatography

HR-TEM : high-resolution transmission electron microscopy

I : measured real-time current

I_0 : measured initial current

IDA : interdigitated array

I_{SD} : source-drain current

JCPDS : joint committee on powder diffraction standards

M_CPPyNP : multidimensional carboxylated polypyrrole hybrid nanoparticle

MDL : minimum detectable level

MFC : mass flow controller

M_PdCPPy : multidimensional palladium decorated carboxylated polypyrrole

nanoparticle

$NaBH_4$: sodium borohydride

NaOH : sodium hydroxide

NP : norepinephrine

NT : neurotransmitter

PANI : polyaniline

PBS : phosphate-buffered solution

PC : polycarbonate

Pd : palladium

$PdCl_2$: palladium (II) chloride

PdCPPy : palladium decorated carboxylated polypyrrole nanoparticle

PEDOT : poly(3,4-ethylenedioxythiophene)

PFF : multidimensional polypyrrole/iron oxyhydroxide hybrid nanoparticle

ppb : parts per billion

ppm : parts per million

PPV : poly(para-phenylene vinylene)

PPy : polypyrrole

Pt : platinum

PT : polythiophene

$PtCl_4$: platinum (IV) chloride

Pt_CPPy : multidimensional platinum decorated carboxylated polypyrrole nanoparticle

p-type : positive type

PVA : poly(vinyl alcohol)

R : real-time measured resistance

R_0 : initial measured resistance

S : sensitivity

sccm : standard cubic centimeters per minute

slm : standard liters per minute

STEM : scanning transmission electron microscopy

T : thymine

TEM : transmission electron microscopy

TGA : thermogravimetric analysis

UA : uric acid

U_PPy : multidimensional urchin-like hybrid polypyrrole

VA : valeric acid or 4,4-bis(4-hydroxyphenyl)valeric acid

VDP : vapor deposition polymerization

V_G : gate potential

V_{SD} : source-drain voltage

XPS : X-ray photoelectron spectroscopy

XRD : X-ray diffraction

List of Figures

List of Tables

Table of Contents

1. INTRODUCTION

1.1. Background

1.1.1. Conducting polymer

Over the last several decades, conducting polymers have received much attention from the viewpoint of both fundamental and applied studies by virtue of the exclusive natures originated from their unique π-conjugated system.[1-3] Since the discovery of polyacetylene in 1977, various kinds of conducting polymers have been continuously investigated, including polypyrrole (PPy), polyaniline (PANI), polythiophene (PT), poly(3,4-ethylenedioxythiophene) (PEDOT), and poly(para-phenylene vinylene) (PPV) (Figure 1).[4] In general, conducting polymers exhibit polyconjugated chains consisting of alternating single (σ bond) and double (π bond) bonds, and these π-conjugated systems play an essential role in determining the electrical and optical properties of conducting polymers. It is known that the significant parameters governing the physical properties of conducting polymers involve the conjugated length, the intra-/inter-chain interaction, and the extent of disorder.

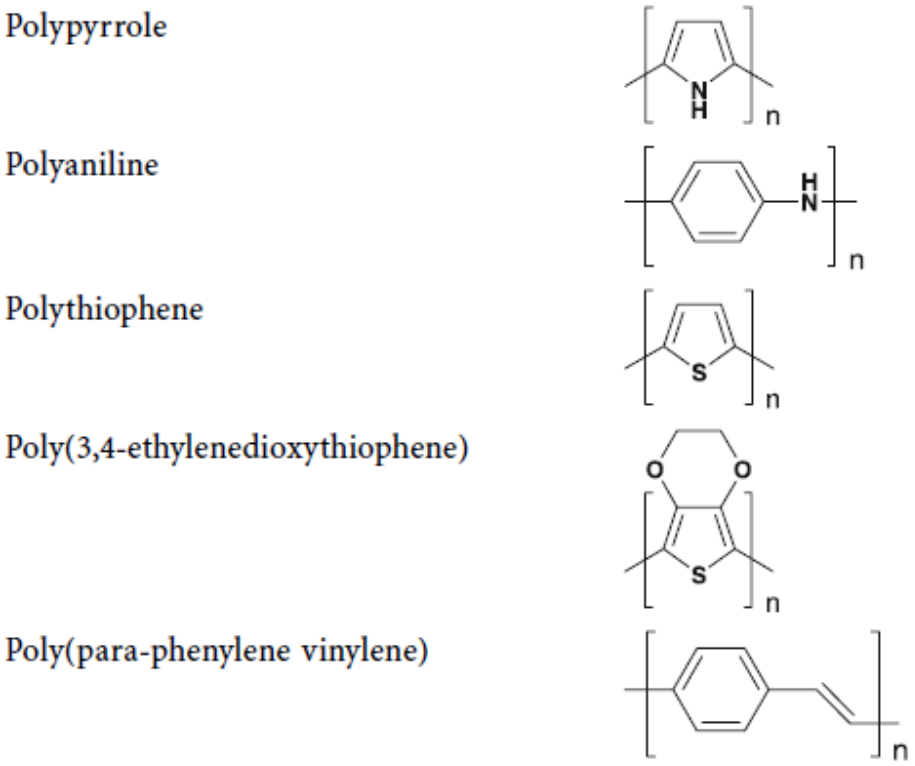

Figure 1. Typical conducting polymer structures (undoped form).[4]

1.1.1.1. Polypyrrole

Polypyrrole is one of the most well-known conducting polymers composed of five membered heterocyclic rings and represented beneficial characteristics including high electrical conductivity, redox property, and environmental stability.[5] Polypyrrole can be readily prepared by electrochemical and chemical approaches in both aqueous and nonaqueous solutions.[6] Electrochemical polymerization commonly occurs films deposited on substrates, on the other hand, chemical polymerization produces powders. The repeating units of polypyrrole are liked predominatly through α-α coupling and thus the polypyrrole chains are intrinsically planar and linear. However, as illustrated in Figure 2, many conformational and structural defects can be formed during polymerization process.[7] Conformational defects are α-α bonds with nonregular rotation and structural defects involve α-β bonds, hydroxyl groups, and carbonyl groups. The hydroxyl and carbonyl groups can be introduced into the polymer chain due to overoxidation, and the α-β coupling leads to brancing and crosslinking. These defects introduce structural disorders in the polymer chain and hence affect the conjugation length and conductivity.

Polypyrrole has four different electronic band structures with changing the doping level of the polypyrrole chain (Figure 3).[5,8] In the neutral state,

polypyrrole is an insulator with a large π- π* band gap of *ca*. 3.16 eV. However, the polypyrrole chain is doped with counterions (mostly anions) to maintain electroneutrality during polymerization. When a negative charge is extracted from a neutral segment of a polypyrrole chain by the doping process, a local deformation from benzenoid to quinoid structure occurs to form a polaron (a radical cation) (Figure 4a and b). The formation of a polaron gives rise to two localized electronic levels (bonding and antibonding cation levels) within the band gap while the unpaired electron occupies the bonding state (S = 1/2). As the oxidative doping proceeds further, another electron is removed from a polypyrrole chain, resulting in the formation of a double charged bipolaron (a dication S = 0) as described in Figure 4c. At higher oxidation level (a doping level of *ca*. 33 %), the overlap between bipolarons is occurred, leading the formation of two narrow bipolaronic bonds.

The highest conductivity of polypyrrole was achieved with a thin film prepared by electrochemical polymerization using PF_6 as a dopant at -40℃.[9] The conductivity was 4×10^2 S cm^{-1} and could be enhanced up to 1.6×10^3 S cm^{-1} by stretching.

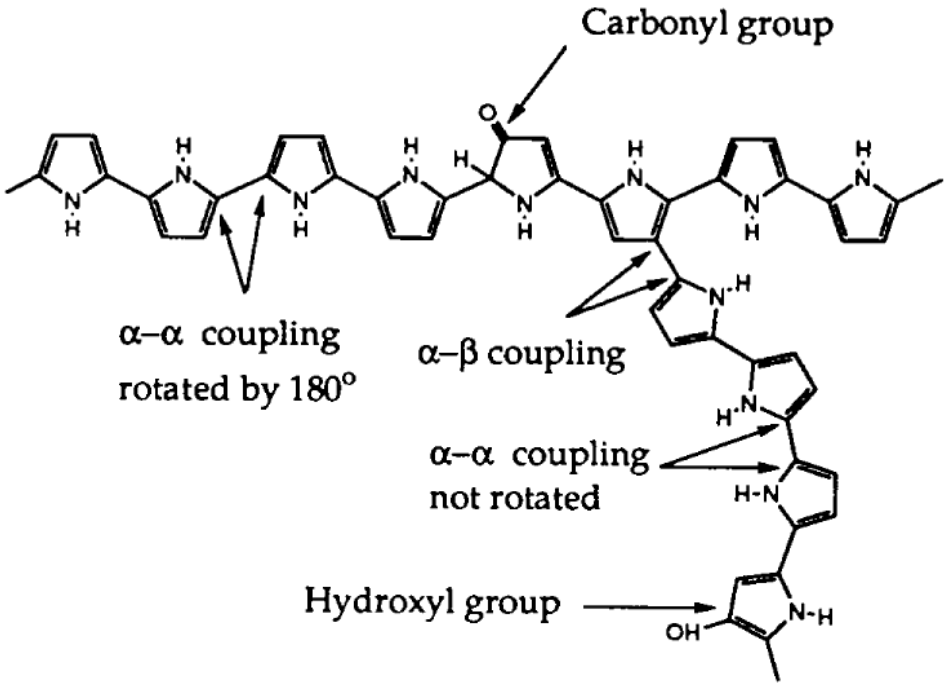

Figure 2. Possible chemical structures in polypyrrole chains: the hydroxyl and carboxyl groups result from overoxidation.[7]

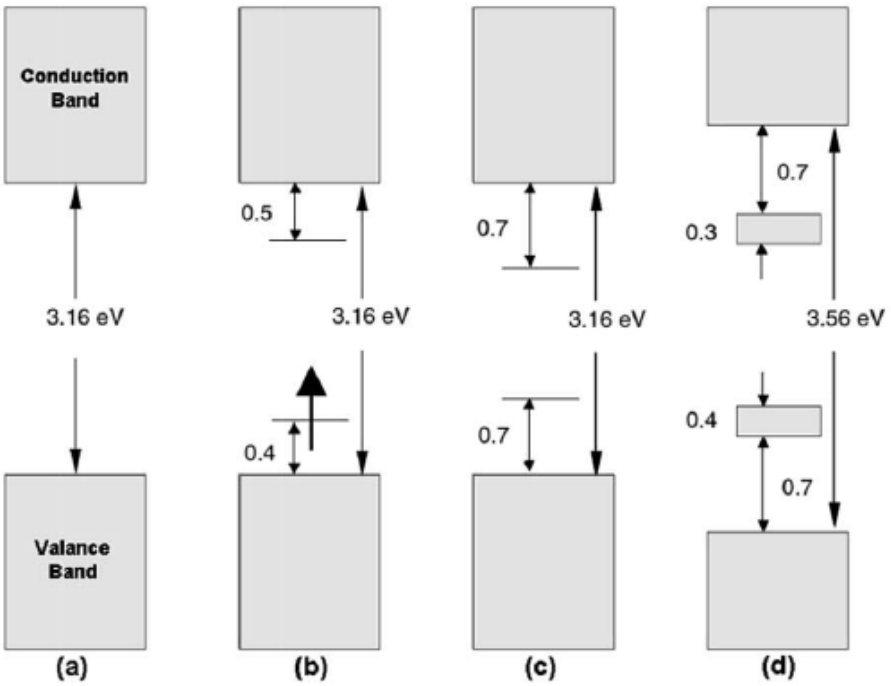

Figure 3. Electric energy diagrams for (a) neutral, (b) polaron, (c) bipolaron, and (d) fully doped polypyrrole.[5]

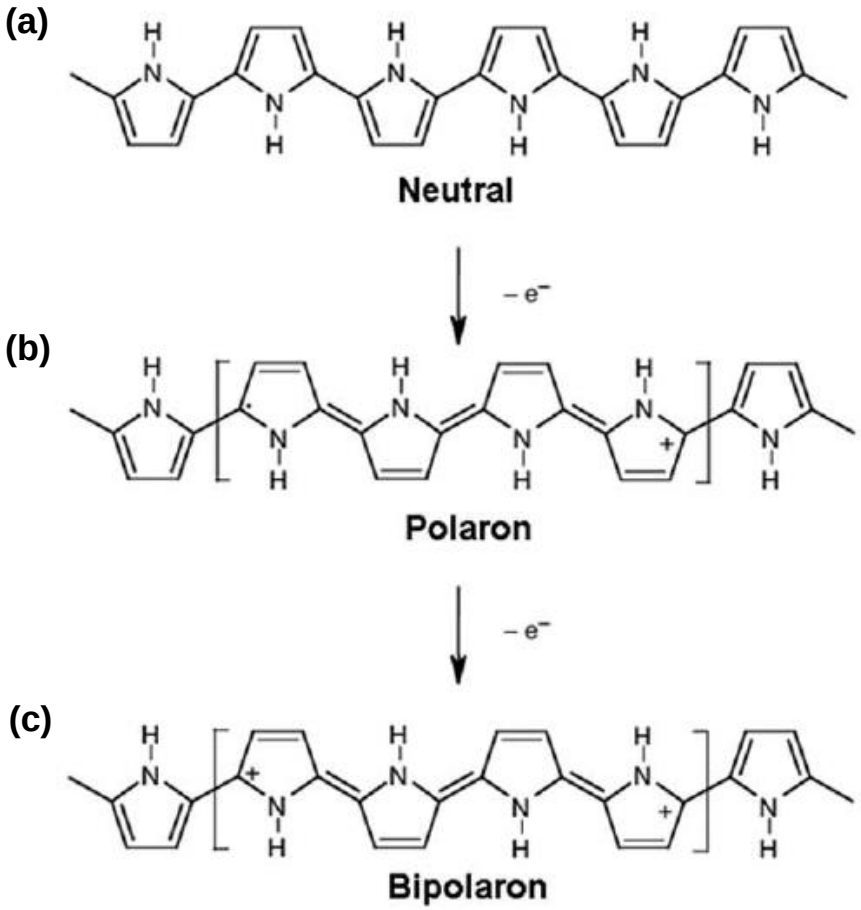

Figure 4. Electronic structures of (a) neutral, (b) polaron in partially doped, and (c) bipolaron in fully doped polypyrrole.[5]

1.1.2. Nanomaterial

From a material viewpoint, the advancement of science and technology provides the smaller and smaller dimensions with higher precision and enhanced performance. Currently, nanotechnology is concerned with fabrication and various applications of functional materials and structures in the range of 1-100 nm using chemical and physical methods.[10–12] Nanoscale size control of material leads to superior physical and chemical properties with molecular and supermolecular structures. Assembling the nanostructures into the ordered array is often necessary to render them functional and operational. Novel nanostructured materials and devices with the enhanced capabilities can be generated by a combination of nanobuilding units and strategies for assembling them. Nanomaterials include nanoparticle, core-shell nanostructure, hollow nanosphere, nanofiber, nanotube, nanopattern, nanocomposite, *etc* (Figure 5).[13]

Nanomaterials are divided into nanosized metal, metal oxide, semiconductor, biomaterial, oligomer and polymer, *etc*. The widespread interest in nanostructured materials mainly originates from the fact that their properties (optical, electrical, mechanical and chemical performance) are usually different from those of the bulk materials.[14,15] These phenomena arise from the quantum chemical effects including quantum confinement and

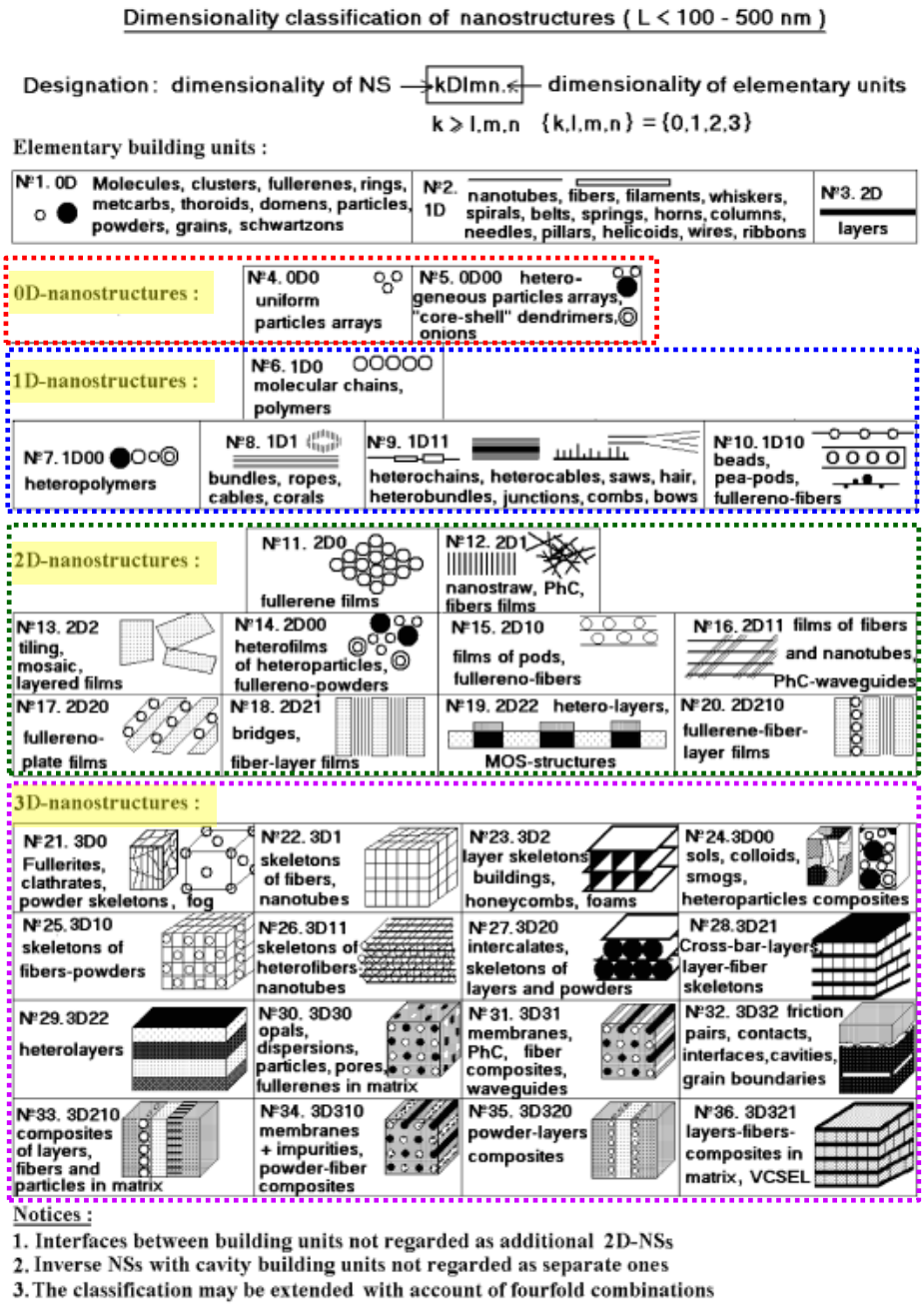

Figure 5. Dimensionality classification of nanostructures.[13]

finite size effect as well as the nano-sized filler effect.[16] The ability to selectively tune defects, electronic states, and surface chemistry has motivated the development of diverse methods to fabricate metallic, inorganic, and polymeric nanomaterials.

1.1.2.1. Conducting polymer nanomaterial

Polymer nanomaterials can find a variety of advantages over other materials in that they have a wide range of source materials and the tunable surface functionalities. Among the polymer materials, conducting polymer nanomaterials are of great interest because of their availability in diverse important applications in current technology including electroluminescence materials, electromagnetic interference (EMI) shielding materials, photovoltaic cells, displays, supercapacitors, batteries, molecular wires, nano-sized transistors, sensors, *etc*.[17-24]

A variety of fabrication methods have been developed for conducting polymer nanomaterials. Among the various synthetic stratagies, template method is a very promising and powerful tool to fabricate conducting polymer nanomaterials. Template method involves the inclusion of guests such as inorganic or organic constituents inside the void spaces of a host material. These voids act as the template, deforming the shape, size, and orientation of

the compound produced. In general, template method is classified into three types: hard template, soft template, and template free. First, hard template process conducted to fabricate 1-D nanostructures (*e.x.*, nanotube and nanorod) by using anodic aluminium oxide (AAO) membrane, track-etched polycarbonate (PC), and zeolite (Figure 6).[25,26] Second, soft template method has been used for the fabrication of various morphologies of conducting polymer nanomaterials. There are several template such as surfactant, liquid crystalline polymer, cyclodextrin, and functionalized polymer.[27-35] Among them, surfactants, which imply cationic, anionic and non-ionic amphiphiles, are mostly used for the formation of micelle as a nanoreactor (Figure 7).[36-41] Third, template-free technques have been extensively studied for the fabrication of conducting polymer nanomaterials fabrication. Compared with hard and soft template methods, these methodologies provide a facile and practical route to produce pure, uniform, and high quality nanofibers. Template-free methods encompass various methods such as electrochemical systhesis, chemical polymerization, aqueous/organic interfacial polymerization, radiolytic synthesis, and dispersion polymerization.[42-46]

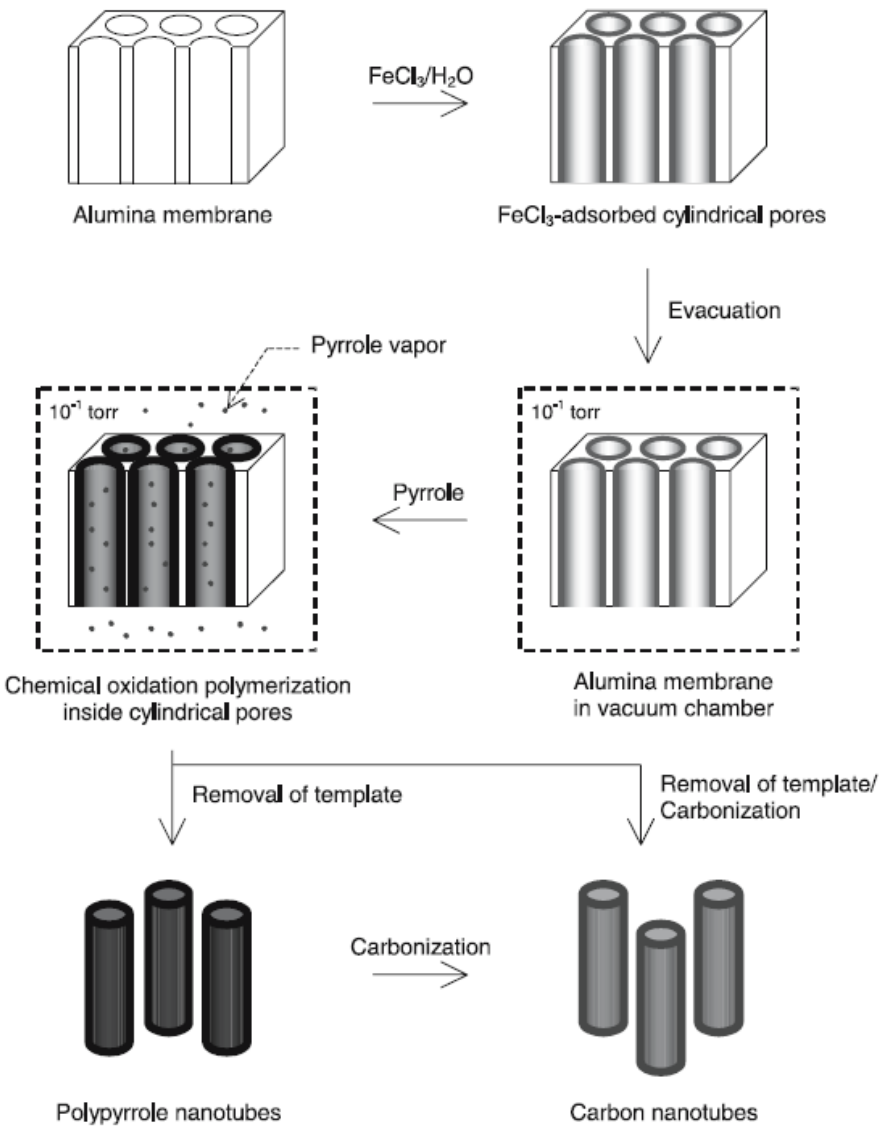

Figure 6. Polypyrrole nanotube, one of conducting polymer nanomaterials, fabrication using hard template (AAO) method.[5]

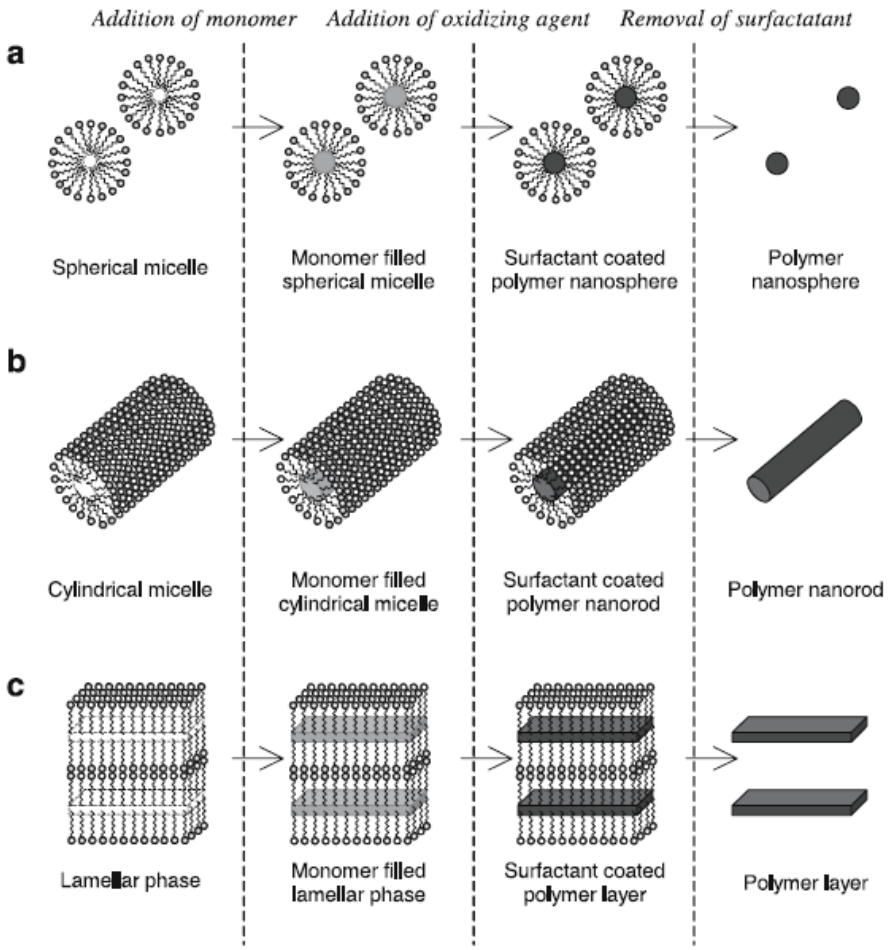

Figure 7. Schematic diagram of the surfactant templating of (a) nanosphere, (b) nanorod, and (c) layered assemblies.[5]

1.1.2.1.1. Polypyrrole nanoparticle

Polypyrrole, one of the most promising conducting polymers, has been extensively explored to fabricate nanoscale architecture because of their easy synthesis, tunable conductivity, reversible redox property, and environmental stability. In particular, spherical polypyrrole nanoparticles have been prepared by several methods. Above all, microemulsion polymerization has been extensively utilized to synthesize various nanometer-sized conducting polymer particles.[47-49] A typical example is the synthesis of polypyrrole nanoparticles with diameter of several nanometers using low temperature polymerization.[50] Another approach to synthesize polypyrrole nanoparticles was self-assemble using the evaporation process of the liquid medium.[51] Dispersion polymerization has been also carried out to prepare polypyrrole nanoparticle by several research groups.[52-54] The synthesis of sterically stabilized polypyrrole colloid was carried out using a tailor-made reactive polymeric stabilizer. Hong *et al*. described the preparation of polypyrrole nanoparticles with the diameter of 20-100 nm by using $FeCl_3$ in aqueous solutions containing PVA as a stabilizer.[55]

1.1.2.2. Metal oxide nanomaterial

A variety of semiconductor nanomaterials have been successfully synthesized to apply future nanoscale electronic, optoelectronic, and sensing device applications. Among the semiconductors, metal oxides emerge as one of the most versatile materials, owing to their diverse properties, *e.x.* superconductivity, ferroelectrocity, magnetism, colossal magneto resistivity, conductivity, and gas-sensing capabilities.[56-60] The metal oxide nanostructures not only inherent the fascinating properties from their bulk form such as piezoelectricity, chemical sensing, and photodetection, but also possess unique properties associated with their highly anisotropic geometry and size confinement.

There are various methods to synthesize metal oxide nanostructures. Accoding to the synthesis environment, they can be mainly devided into two categories: vapor phase growth and solution phase growth. Most of the metal oxide nanostructures are grown *via* the well-developed vapor phase technique, which is based on the reaction between metal vapor and oxygen gas (Figure 8a).[61,62] The governing mechanisms are the vapor-liquid-solid process, with catalyst, and vapor-solid process, without catalyst. On the other hand, solution-phase growth methods provide more flexible synthesis process (*e.x.* electrochemical deposition, sol-gel deposition, surfactant-assisted growth,

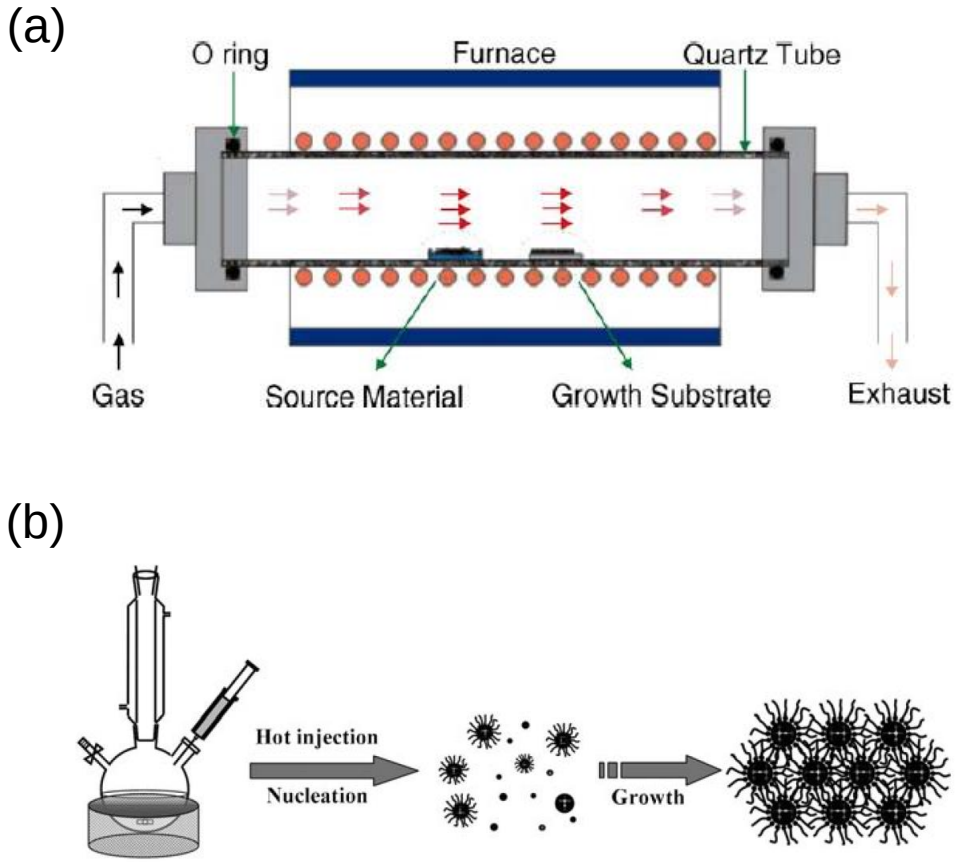

Figure 8. Schematic diagram of metal oxide nanomaterials through (a) vapor-phase growth and (b) solution phase growth method.[61,63]

sonochemical method, and hydrothermal process) and an alternative to achieve lower cost (Figure 8b).[63-67]

1.1.2.3. Noble metal nanomaterial

Noble metal nanomaterials (*i.e.*, Au, Ag, Pt, and Pd) have been attracted increasing attention because of their potential use in catalysis, electronics, and biological applications.[68-70] Among them, platinum nanocrystals are invaluable key catalyst to many industrial processes as following: 1) CO/NO_x oxidation in catalytic converters; 2) hydrogen (or alcohol) oxidation and oxygen reduction reactions in fuel cells; 3) nitric acid production; 4) petroleum cracking.[71,72] Palladium nanocrystals are also widely used as primary catalysts for the low-temperature reduction of automobile pollutants, hydrogenation reactions, and organic reactions such as Suzuki, Heck, and Stille coupling.[73,74] In addition, palladium is well-known for its remarkable capacity in hydrogen absorption.[75]

There are two fundamental strategies used to prepare noble metal nanomaterials: bottom-up and top-down. The bottom-up approach is a basic technique to prepare the noble metal nanostructures by reducing their ions and the growing of the nanoarchitectures is usually stopped by an agent such as a surfactant or stabilizer. Bottom-up techniques include chemical reduction,

photochemical reduction, electrochemical reduction, templating, and thermal methods.[76-80] On the other hand, the top-down approach involves removing materials from the bulk substrate to leave behind the desired nanostructures. Common top-down methods include photolithography, electron beam lithography, and nanosphere lithography.[81,82]

1.1.2.4. Hybrid nanomaterial

The synthesis of novel materials with improved properties and performance is a continually expanding frontier at the material science. In general, polymeric nanomaterials themselves display poor mechanical properties such as brittleness and deficient processibility.[83,84] On the other hand, inorganic (metal and metal oxide) nanomaterials have some lack of stability due to the Ostwald ripening process of low dimensional nanaomaterials, leading to large aggregated nanoparticles.[85,86] The combination of inorganic materials with polymeric compounds provide an excellent functionality with high performance as well as ehnaced stability and good processability. Therefore, many efforts have been devoted to synthesize novel functionalized hybrid nanomaterials for their potential applications.[87.88]

1.1.2.4.1. Metal oxide/conducting polymer

Hybrid nanomaterial consisted of conducting polymer and metal oxide semiconductor has been recognized as one of the attractive combinations for the organic/inorganic hybrid.[89,90] Owing to semiconducive property originated from each component and flexibility stem from conducting polymer structure, they are extensively implemented in various applications, such as photovoltaics, electrochemical capacitors, transistors, sensors, and electrochromic devices.[91-94]

There are two main approachs to fabricate metal oxide/conducting polymer hybrid nanomaterials. First approach is conducting polymer coating on the metal oxide surface to form core-shell architecture through coating process such as electrodeposition and vapor deposition polymerization (VDP).[95,96] These core-shell morphology composites are applied to energy storage and electrochemical devices on account of coated conducting polymer acted as protecting layer to reduce collapse of metal oxide structure during electrochemical reaction.[97,98] Another approach is introduction metal oxide nanostructure to the conducting polymer matrix through sonochemistry and solution redox process.[99,100] The introduced metal oxide architecture conducted as active site to react with other analyte in sensing application.[101]

1.1.2.4.2. Noble metal/conducting polymer

Noble metal/conducting polymer nanostructures have been extensively studied because of their potential applications ranging from electronic and optical devices to sensing and catalyst.[102-104] Generally, there are two synthetic approaches for the preparation of noble metal/conducting polymer nanostructures: in-situ and ex-situ methods.[105] The ex-situ method involves noblel metal architecture formation first and then dispersing them into polymer matrix.[106] In the case of in-situ approach, metal nanoparticles can be coincidently generated inside a polymer by reduction of metallic precursor which is dissolved into the polymer or polymerizing solution.[107]

Recently, Chujo *et al*. synthesized silver dendritic structures *via* redox reaction between conducting polymer and silver ions in solution.[108] They pointed out that π-conjugated polymer containing the strong electron-donating unit could reduce silver ions. Moreover, Zinovyeva and co-workers uniformly fabricated palladium particle embedded polypyrrole nanoparticles by in-sity mechanism through electron exchange between palladium ion and pyrrole monomer. They explained that palladium cations (Pd^{2+}) was responsible for formation of polypyrrole nanoparticle as initiator with reduced to palladium (Pd^{0}).[109] Additionally, in-sity formation of noble metal particles occurred onto polymer surfaces due to the recution potential of generated radical.[110]

1.1.3. Sensor application

Sensor is a transducer device to detect some characteristic environmental elements.[111] This device composed of an active sensing material with a signal transducer. The role of these two important components in sensor system is to transmit signal without any amplification from a selective compound or from a change in a reaction.[112] The sensor devices produce any one of the electrical, thermal or optical output signals, which could be converted to digital signals for subsequent processing. There are two type sensor devices with source of target anlayte: chemical sensor and biosensor. The chemical sensor is a self-contained analytical device that can provide information about the chemical composition of its environment with a liquid or gas phase. The information is provided in the form of measureable physical signal that is correlated with the concentration of a certain analyte. On the other hand, the biosensor is a device which detects biological component analytes such as cells, protein, nucleic acid or biomimetic polymers.

There are several critical elements for highly effective sensor detecting system: 1) high sensitivity; 2) selectivity to target analyte; 3) fast response/recovery time; 4) cycle stability; and 5) low working temperature.[113,114] To satisfy these demands, nanomaterial based sensor electrode has been emerged as promising candidates on count of its small size

such as high surface to volume ratio and unique optical/electrical properties. Furthermore, recentely, multidimensional conductive nanoarchitectures are suggested as sensing transducers to maximize sensitivity for target analyte through enhancing active surface area.[115]

1.1.3.1. Resistive chemical sensor

Within the realm of chemical sensing, resistive chemical sensors (*i.e.*, chemiresistive sensor), which interpret chemical information by means of two point contact electrical resistance changes, are among the most studied and promising transduction mechanisms for conductive nanomaterials based systems (Figure 9a).[116,117] This is largely due to the fact that current of electrical resistance is one of the simplest of electric signals to analyze requiring minimal supporting electronics, for compact, deployable, self-contained systems.

Among diverse chemiresistive sensing systems, interdigitated array (IDA) based chemiresistive sensors have several strengths to apply chemical sensing device (Figure 9b).[113,118] First, it displays high sensitivity and fast response time than other detection approaches in air on account of fast signal transfers from transducer materials to the electrode. Other strength is the simple measurement with real-time changing resistance of the electrode without

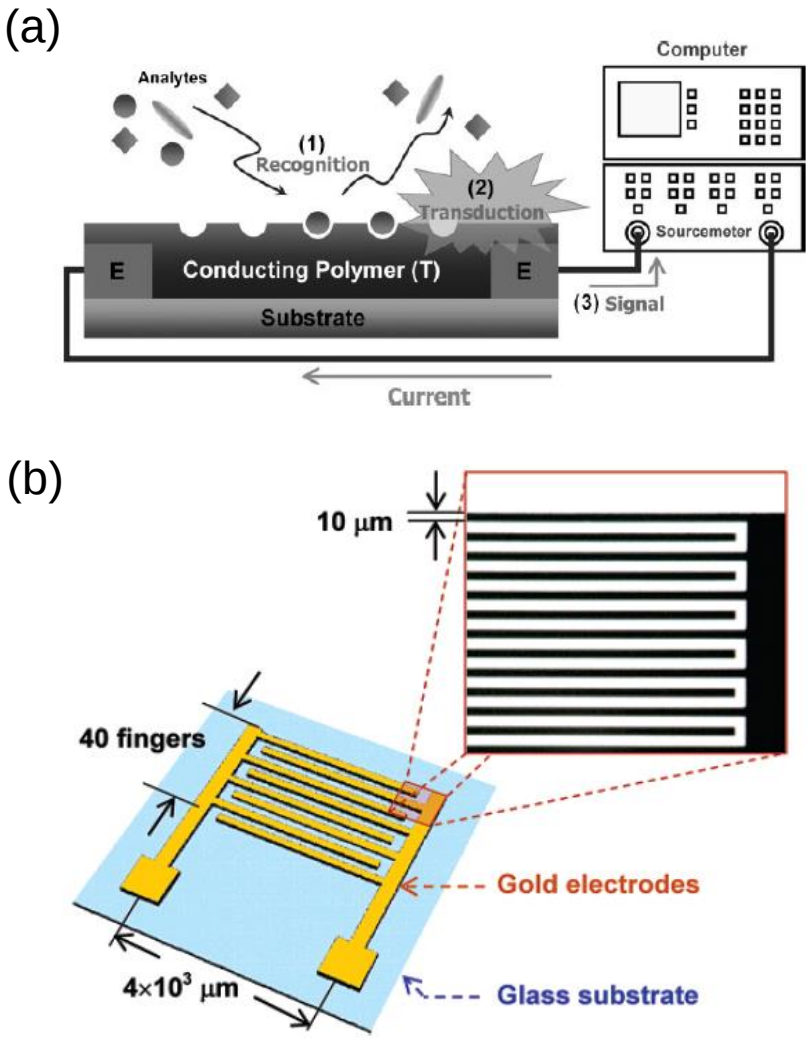

Figure 9. (a) Schematic illustration of an electrochemical sensor consisting of a transducer (T), electrode (E), and substrate. The overall sensing process involves 1) analyte recognition, 2) signal transducer, and 3) electrical readout.[116] (b) Schematic illustration and optical micrograph of a gold microelectrode array on glass substrate (finger dimensions: 10 μm width, 50 nm thickness, 4×10^3 μm length, 10 μm inter-electrode spacing).[113]

additional measurement steps during target analyte detection. The cycle ability is the other strength of the IDA sensing device without any defect during repeated target chemical sensing.

1.1.3.1.1. DMMP sensor

The development of chemical warfare has produced weapons used to terrorize people in times of war and peace, for example, the attack on the Tokyo subway in 1995, in particular, odorless, colorless, chemical warfare agents (CWAs), such as Sarin, Soman, and Tabun, composed of organophosphorous compounds that disrupt the mechanism by which nerves transfer messages to organs in the body.[119,120] Therefore, these toxic chemicals have motivated intensive research in the development of sensitive, selective, portable chemical sensors. However, there are several limitations to detect these nerve agents in air owing to their dangerous and fatal impact to humans. Thus, instead of toxic nerve chemicals, simulants for nerve agents that have similar chemical structure and the same sensing mechanism are used to detect in air.[121] Among chemical nerve agent simulants, dimethyl methylphosphonate (DMMP) has a similar structure to Sarin, is used to detect for simulant for Sarin, and also requires a method for its detection in air. Recently, several scientific approaches have been devised to detect these nerve agents, such as colorimetric analysis, mass spectroscopy, enzymatic assay, gas

chromatography, molecular imprinting, and photoacoustic spectroscopy.[122-126] Although all of these methods have advantages, critical limitations remain, including low sensitivity, slow response time, high cost, and limited portability, particularly, operational complexity for colorimetric analysis and temperature-dependent for enzymatic assay.

1.1.3.1.2. Hazardous gas sensor

Environmentally hazardous gases, including toxic gases (*e.x.* hydrogen sulfide (H_2S), carbon monoxide (CO), and ammonia (NH_3)) and volatile organic compounds (VOCs) (*e.x.* acetone (CH_3COCH_3), ethanol (C_2H_5OH), and ethane (C_2H_6)) have been detected in the exhaled breath of healthy subjects and patients with respiratory diseases.[127–134] In particular, NH_3 is a colorless, widely used gas with a characteristic pungent odor. It contributes significantly to the nutritional needs of terrestrial organisms by serving as a precursor for food and fertilizer, and it is a common building block in the synthesis of many pharmaceuticals and industrial materials.[135,136] Despite its usefulness, it is both caustic and hazardous to humans, especially when its concentration exceeds the threshold limit value (TLV) of 25 ppm.[137,138] Therefore, effective and inexpensive systems for detection and quantification of hazardous gases like NH_3 are needed to prevent adverse effects.

1.1.3.1.3. Hydrogen gas sensor

Hydrogen is a non-toxic, non-poisonous, colorless, odorless, and tasteless gas that combusts in air to produce water. Therefore, hydrogen gas is widely used in industrial applications, including fossil-fuel production, chemical compound synthesis, power plant operation, fuel-cell applications and in the aerospace and automotive industries.[139-141] In recent years, hydrogen energy has received a great deal of attention for nextgeneration applications, such as hydrogen-based zero-carbon emission vehicles. However, because of the wide explosive range of concentration (4 to 75 vol%), safe storage is a critical issue when working with gases containing hydrogen.[142,143] Additionally, the hydrogen can also cause asphyxiation with displacing oxygen/air when higher concentration than normal level.[144,145] Thus, rapidly responsive sensors with high sensitivity are necessary to monitor hydrogen concentration levels.

1.1.3.2. Liquid electrolyte gated FET sensor

To detect bio-target analyte, biosensor consists of a biological sensing element such as antibody, cell, receptor, and aptamers, which are binded to transducers (*e.x.*, conductive nanomaterials).[146,147] Measurement of a target analyte can be achieved by selectively converting the molecular recognition occurring at the analyte-biological element binded to transducers from a nonelectrical domain to an electrical signal.[148,149] The binding of the analyte is then detected through a change in the electrical property at the sensing transducer (Figure 10a).[150]

Among various types of biosensors, field-effect transistors (FETs) have attracted increasing interests as primary candidates to fabricate state-of-the art sensor platforms because they are capable of achieving high current amplification and sustaining an enhanced signal-to-noise (S/N) ratio.[151-154] In particular, conducting polymer based nanomaterials have been attracted much attention as promising building blocks for FET sensor applications.[155, 156] Compared with conventional films, conducting polymer nanomaterials have remarkable characteristics derived from anisotropic electronic properties, high surface area, and small dimensions.[157,158] Yoon *et al*. reported the electronic nose based on a liquid-ion gated field-effect transistor configuration in which human olfactory receptor-functionalized PPy nanotubes are employed

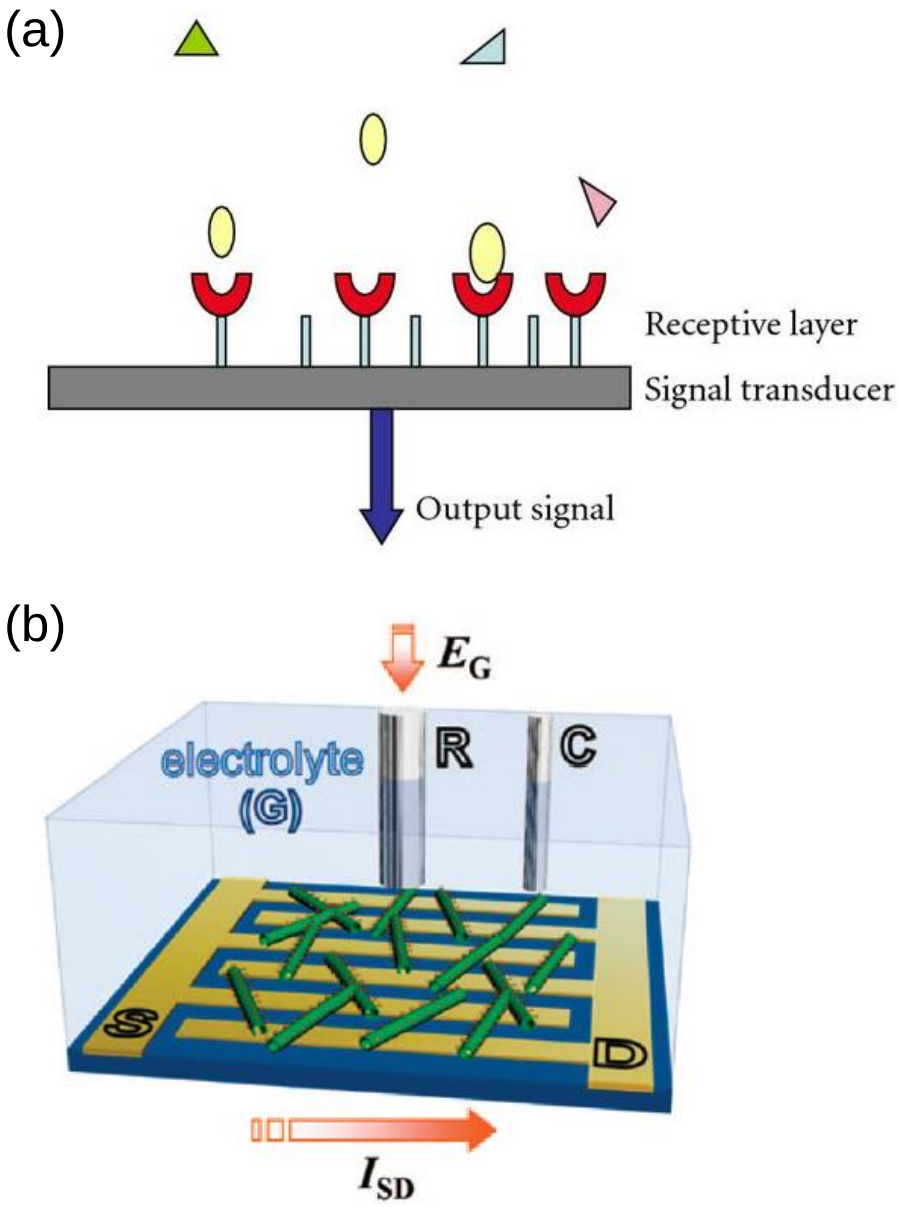

Figure 10. (a) Specific biomolecule detection mechanism of biosensor.[146] (b) Schematic diagram of a liquid-ion gated FET sensing system.[159]

as the conductive channel (Figure 10b).[159]

1.1.3.2.1. Bisphenol A aptamer FET sensor

Recently, xenobiotic compounds have been detected in large quantities in the human environment and in various chemical product fabrications.[160–163] One such type of xenobiotic compounds, endocrine disruptors (EDs) has a structure that is similar to estrogen. EDs show an affinity for human estrogen receptors (ERs), such as ER-α and ER-β, and have been linked to serious diseases related to the estrous cycle, such as male infertility and various types of cancer.[164–169] Among EDs, bisphenol A (BPA) has emerged as a particularly harmful material, due to its widespread use in the raw materials of plastics and its release from polycarbonate bottles at high temperatures.[170–173] ERs associated with the cell membrane can simulate physiological responses at low BPA concentrations (100 pM).[174–176] In addition to its association with infertility and cancer, BPA is also linked to cardiovascular disease and diabetes.[177–179] Therefore, the release of BPA from plastic packaging or cups should be accurately monitored on site for human health. Several analytical methods have been examined for the detection of BPA at low concentrations.[180–183]

Nucleic acid aptamers, which are synthetic molecules of single-stranded

DNA (ssDNA) or RNA, have been receiving significant attention since 1990.[184,185] Aptamers can detect small molecules, such as environmental pollutants, food toxicants, and disease-related metabolites in solution, through conformational changes after binding with a target.[186–189] Compared with antibodies, aptamers are better capture agents for small molecules, for the following reasons. First, their small structure more accurately discriminates between the functional groups of similar structures. Second, small molecules can be targeted in vitro, without the need for hapten, which is often required to facilitate the selection of antibodies among other molecules.

1.1.3.2.2. Nonenzyme dopamine FET sensor

Neurotransmitters (NTs) are chemical messengers through secretion from one neuron to the next until binding onto specific receptors located on the membranes of target cell.[190–194] Among various NTs, dopamine (DA) has been widely studied since 1950s due to its important role in the functions of central nervous system, renal, hormonal, and cardiovascular system.[195–197] In particular, abnormal level of DA is believed to be associated with certain neurological disorders known as sleeping and eating disorders, Parkinson's disease, and addictive behaviors associated with drug abuse.[198–201] However, the clinical concentration of DA is very low; for example, the DA

levels in plasma, urine, and single adrenal chromaffin cell are in the range of nM (10^{-9} M), μM (10^{-6} M), and fM (10^{-15} M), respectively.[202–204] Therefore, rapid and sensitive detection of DA in biological system is important for the routine analysis and diagnosis of neurological disorders.

Several analytical methods have been conducted for detection DA at low concentrations.[205–209] Among them, enzymatic-assay-based methods have attracted considerable attention due to their high sensitivity for DA and comparable low cost.[210,211] However, these techniques are not used as frequently owing to accurate DA detection depends strongly on the quality of the prepared enzyme and nonspecific binding to analytes having a similar structure. In this regard, electrochemical sensing technique based on field effect transistors (FETs) without enzyme contained for dopamine detection is an attractive method on account of low cost, easy operation, fast response, high sensitivity, and feasibility of miniaturization. [212,213]

1.2. Objectives and Outlines

1.2.1. Objectives

The aim of this dissertation is providing novel methods to fabricate multidimensional metal/conducting polymer hybrid nanomaterials for highly sensitive sensor application. Different kinds of metal such as iron oxyhydroxide (FeOOH), platinum (Pt), and palladium (Pd) were adopted to produce hybrid nanomaterials. Conducting polymers of polypyrrole (PPy) and carboxylated polypyrrole (CPPy) nanoparticles were used for the polymeric structure agent. Through facile and innovative methods in each experimental condition, the multidimensional hybrid nanomaterials could be obtained with unique potential properties. The as prepared multidimensional hybrid materials applied several chemical/bio sensor applications such as chemical nerve agent simulant (DMMP), hazardous gas (NH_3/MeOH), hydrogen (H_2), endocrine disruptor (Bisphenol A), and neurotransmitter molecule (dopamine), respectively.

1.2.2. Outlines

This dissertation could be devided following two categories; multidimensional metal oxide- and noble metal-based conducting polymer hybrid nanomaterials. In the metal oxide based hybrid nanoparticles, multidimensional iron oxyhydroxide/polypyrrole nanoparticles, multidimensional polypyrrole hybrid nanoparticles, and aptamer-functionalized multidimensional carboxylated polypyrrole nanoparticles were synthesized *via* dual-nozzle electrospray and vapor deposition polymerization methods. On the other hand, noble metal decorated multidimensional hybrid nanoparticles (*i.e.*, platinum/carboxylated polypyrrole and porous palladium/carboxylated polypyrrole) were synthesized through facile redox chemical processes. From fabrication of nanomaterials and their sensor applications field points, this dissertation involves the following subtopics:

I. Multidimensional iron oxyhydroxide/polypyrrole hybrid nanoparticles
  I-1. Fabrication of multidimensional iron oxyhydroxide/polypyrrole hybrid nanoparticles
  I-2. Application for nerve agent simulant chemical sensor

II. Multidimensional polypyrrole hybrid nanoparticles
  II-1. Fabrication of multidimensional polypyrrole hybrid nanoparticles
  II-2. Application for hazardous gas chemical sensor

III. Aptamer-functionalized multidimensional carboxylated polypyrrole hybrid

2. EXPERIMENTAL DETAILS

2.1. Multidimensional metal oxide/conducting polymer hybrid nanoparticles

2.1.1. Multidimensional polypyrrole/iron oxyhydroxide hybrid nanoparticles

2.1.1.1. Fabrication of multidimensional polypyrrole/iron oxyhydroxide hybrid nanoparticles

Poly(vinyl alcohol) (PVA, Mw 9000) and $FeCl_3$ (97%) were purchased from Aldrich Chemical Co. and used without further purification. Pyrrole monomer (98%) and NaOH were also obtained from Aldrich Chemical Co. and used as received.

Uniformly sized polypyrrole (PPy) nanoparticles were previously prepared with PVA, $FeCl_3$, and pyrrole monomer in distilled water, as following (Figure 11). A variable amount of PVA was magnetically stirred in distilled water. PVA was dissolved in distilled water at room temperature. The concentration of aqueous PVA solution contained was 7.50 wt% relative to the amount of water. After dissolution of PVA in distilled water, $FeCl_3$ was added into the aqueous PVA solution. The molar ratio of $FeCl_3$ to pyrrole was 6.9. The system evolved from a limpid state to a viscous orange state in appearance. After 1 h to allow equilibration, pyrrole monomer was introduced into the aqueous PVA/$FeCl_3$

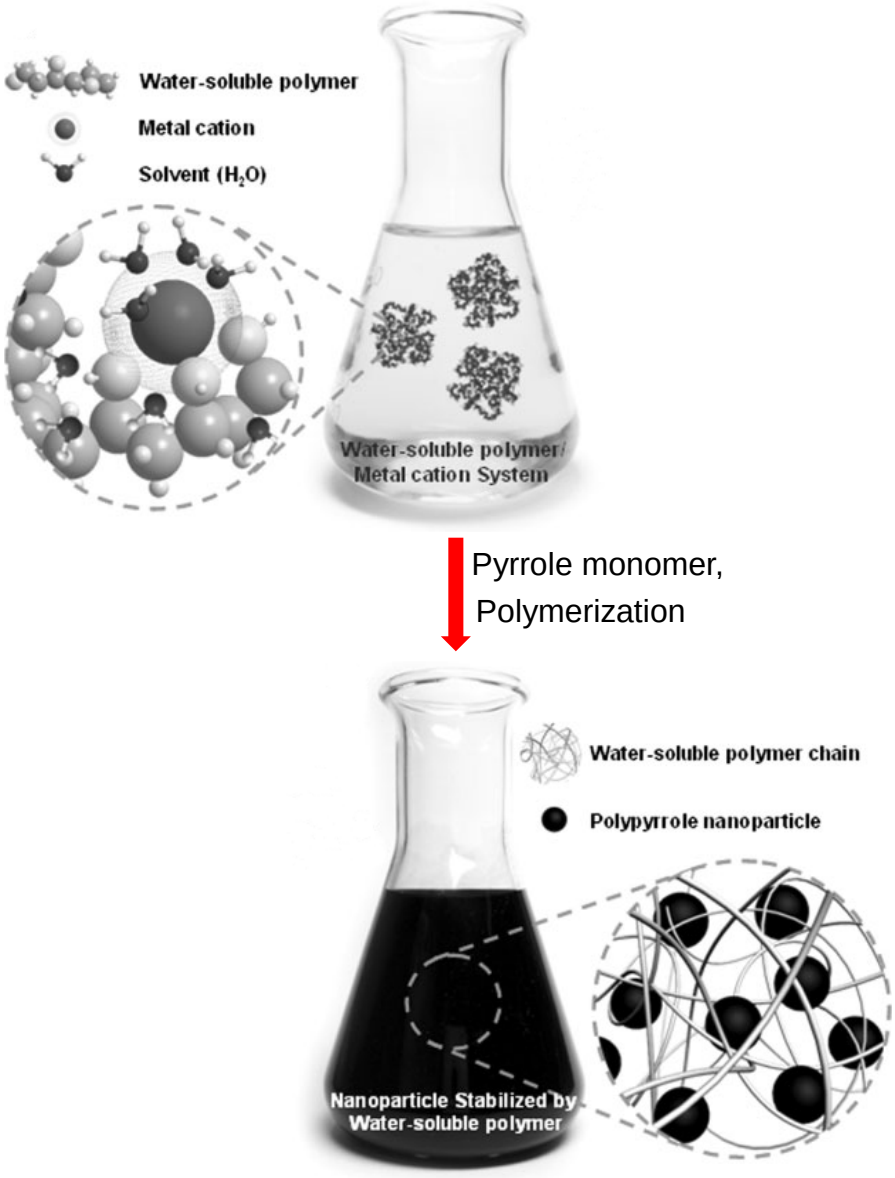

Figure 11. Schematic illustration of the formation of polypyrrole nanoparticles in an aqueous PVA solution through dispersion polymerization.[55]

solution. The concentrations of pyrrole monomer ranged from 0.1 to 1.0 M. Polymerization proceeded while stirring for 4 h. After completion of polymerization, the resulting nanoparticles were separated from the dispersion solution by centrifugation (10000 rpm, 40 min) and washed several times with hot water to remove impurities. The remaining PPy nanoparticle precipitate was dried in a vacuum oven at room temperature.

As the prepared PPy nanoparticles were mixed with a 10 wt% $FeCl_3$ aqueous solution and then stirred for 4 h at room temperature. The mixed solution was loaded into a syringe pump (KD Scientific, U.S.A.) and then pumped through the outer part of the dual metal nozzle (20 G needle; inner diameter: 0.5 mm) (Figure 12). Compressed air flowed through the inner part of the dual-nozzle (27 G needle; inner diameter: 0.1 mm). A voltage of 15 kV was applied between the metal nozzle and the collector Petri dish. The Petri dish collector contained a NaOH aqueous solution to maintain a stable Taylor cone. The distance between the nozzle and collector was 15 cm. The flow rate of the syringe pump was maintained at 0.1 mL h^{-1}. The materials obtained from the electrospray were dispersed in various concentrations of the $FeCl_3$ aqueous solution and stirred for 4 h at 70℃. The reacted solution was cleaned with ethanol several times and then dried at 60℃ for 12 h.

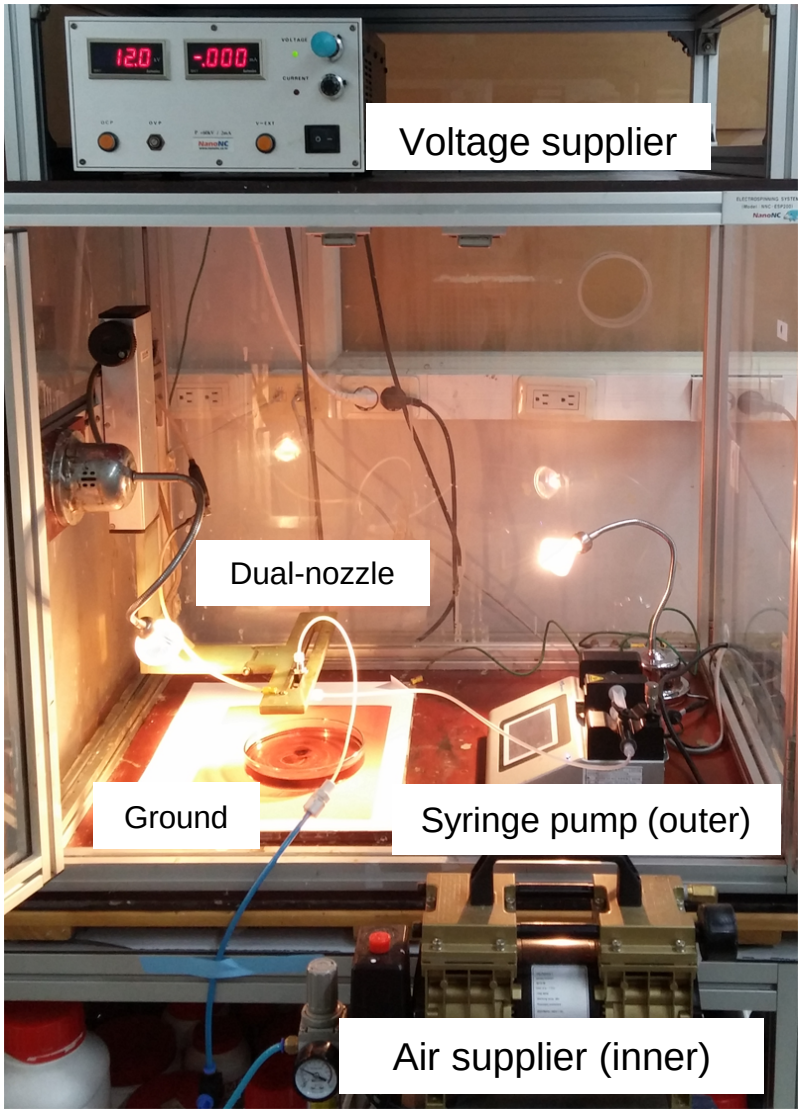

Figure 12. Photograph image of dual-nozzle electrospray apparatus.

2.1.1.2. Application for nerve agent simulant chemical sensor

The multidimensional polypyrrole/iron oxyhydroxide hybrid nanoparticles (PFFs) were prepared by ultrasonication for deposition on the as-prepared interdigitated array (IDA) with 0.5 wt% in ethanol solution. The samples were introduced by a drop-casting method on top of the IDA, to reduce the contact resistance between the particles. The physical adsorption of PFFs on the substrate was followed by drying at room temperature in an inert atmosphere for 1 h to obtain good electrical ohmic contact between the PFFs and electrodes. In the droplet process, a spin-coating method (1000 rpm, 45 s) was used for introducing the uniformly controlled array. A randomly disordered sensor substrate, produced using the drop-casting method, was used as a control.

Resistance changes in the hybrid PFF were monitored with a source meter connected to a computer. The hybrid PFF sensors were placed in a vacuum chamber, having a vapor inlet/outlet pressure of 10^0 Torr. Various DMMP vapor concentrations (0.1 - 1000 ppb) were injected into the chamber by a mass flow controller (MFC, KNH Instruments). The real-time resistance was monitored at a constant applied current of 10^{-6} A (defined as $\Delta R/R_0 = (R - R_0)/R_0$, where R and R_0 are the real-time and initial resistances, respectively). After the PFF nanoparticles interacted with various concentrations of DMMP vapor for several minutes, each vapor was replaced by compressed air to remove the molecules attached to the backbone of the PFFs. This process was

performed repeatedly several times. Vapor/air was supplied at various flow rates of 2-8 slm and 1-5 sccm using the MFC.

2.1.2. Multidimensional polypyrrole hybrid nanoparticles

2.1.2.1. Fabrication of multidimensional polypyrrole hybrid nanoparticles

Poly(vinyl alcohol) (PVA, Mw 9000), $FeCl_3$ (97%), and $CuCl_2$ (97%) were purchased from the Aldrich Chemical Company and used without further purification. Pyrrole (98%) monomer and NaOH were also obtained from the Aldrich Chemical Company and used as received.

Uniform PPy nanoparticles of various sizes were prepared with PVA, $FeCl_3$, and the pyrrole monomer in distilled water. First, various amounts of PVA (0.5–7.5 wt%) were stirred in distilled water, and then $FeCl_3$ was added to the PVA solutions. After few minutes of equilibration, the pyrrole monomer was introduced into the mixed polymer solution. The molar ratio of $FeCl_3$ to pyrrole monomer was 2.3, and the volume ratio of pyrrole-to-water was 6.25×10^{-3}. Various sizes of PPy particles (30, 60, and 100 nm diameters) were mixed with a 10 wt% $FeCl_3$ aqueous solution and then stirred for 4 h at room temperature. The mixed solution was loaded into a syringe pump (KD Scientic, USA) and pumped through the outer part of a dual metal nozzle (20 G needle; inner

diameter: 0.5 mm). Compressed air flowed through the inner part of the dual-nozzle (27 G needle; inner diameter: 0.1 mm). A voltage of 15 kV was applied between the metal nozzle and a Petri dish collector, which contained an aqueous NaOH solution to maintain a stable Taylor cone. The distance between the nozzle and the Petri dish collector was 15 cm. The flow rate of the syringe pump remained fixed at 0.1 ml h^{-1}. The materials obtained from the electrospray were dispersed in a 10 wt% $FeCl_3$ aqueous solution, which was stirred for 4 h at 70℃. The solution was cleaned with ethanol several times and then dried at 60℃ for 12 h. The obtained hybrid particles were soaked in a 5 wt% $CuCl_2$ ethanol solution. The particles were then exposed to the vaporized pyrrole monomer for 5 min at room temperature in a vacuum chamber to initiate polymerization on the particle surface.

2.1.2.2. Application for hazardous gas chemical sensor

U_PPy particles (0.5 wt% in ethanol solution) were prepared by ultrasonication for deposition onto an as-prepared interdigital array (IDA) electrode. The U_PPy sample was introduced by spin-coating (1000 rpm, 45 s) to create a uniform array of particles.

The as-prepared IDA electrode measured resistance changes in the particles with a source-meter connected to a computer. The U_PPy particle sensors were

placed in a vacuum chamber with a vapor inlet/outlet pressure of 10^0 Torr. Various concentrations of NH_3 (0.01–10 ppm), MeOH (0.5–50 ppm), and other organic gases were injected into the chamber using a mass-flow controller (MFC, KNH Instruments). The real-time responses from the U_PPy nanoparticles were systematically evaluated by normalized resistance changes ($\Delta R/R_0$). The normalized resistance change ($\Delta R/R_0$) of the U_PPy based sensor was monitored in real-time during exposure to various gases at a constant applied current (10^{-6} A) until saturation was reached. $\Delta R/R_0$ of the U_PPy nanomaterials is given by the following equation:

$$\Delta R/R_0 = (R - R_0)/R_0$$

where R_0 is the initial resistance and R is the measured real-time resistance, respectively. After the U_PPy particles were exposed to various concentrations of NH_3 or MeOH gas for several minutes, the gas vapor was then replaced by compressed air to remove any molecules attached to the nanomaterials. This process was repeated several times. Vapor/air was supplied at various flow rates ranging from 2 to 8 slm and 1 to 5 sccm, as controlled by the MFC.

2.1.3. Aptamer-functionalized multidimensional carboxylated polypyrrole hybrid nanoparticles

2.1.3.1. Fabrication of aptamer-functionalized multidimensional carboxylated polypyrrole hybrid nanoparticles

Poly(vinyl alcohol) (PVA; MW: 9000), $FeCl_3$ (97%), and $CuCl_2$ (97%) were purchased from Aldrich Chemical Company and used without further purification. Pyrrole (98%) and pyrrole-3-carboxylic acid were purchased from Aldrich and Acros Organics. BPA (4,4′-(isopropylidene)diphenol), BPB (4,4′-(1-methylpropylidene)diphenol), VA (4,4-bis(4-hydroxyphenyl)valeric acid), BP (4,4′-bisphenol), and 6F (4,4′-(hexafluoroisopropylidene)diphenol) were purchased from TCI. The BPA-binding aptamer was synthesized by Bioneer Co. (Daejeon, Korea); the sequence of the designed aptamer was 5′-NH_2 -CCG GTG GGT GGT CAG GTG GGA TAG CGT TCC GCG TAT GGC CCA GCG CAT CAC GGG TTC GCA CCA-3′, where C, G, T, and A represent cytosine, guanine, thymine, and adenine, respectively. The aptamer stock solution was diluted with diethyl pyrocarbonate (DEPC)-treated water and stored in the freezer before use (−20°C).

Uniform CPPyNPs with diameters of 30, 60, and 100 nm were prepared with PVA, $FeCl_3$, and a mixture of pyrrole and pyrrole-3-carboxylic acid monomers (molar ratio of (pyrrole) : (pyrrole-3-carboxylic acid) = 30 : 1).

The CPPyNPs were electrosprayed along with compressed air through a dual-nozzle at an applied voltage of 15 kV into an aqueous NaOH solution contained within a Petri dish; the outer and inner parts of the spray were the CPPyNPs and air, respectively. The resulting aqueous solution of the electrosprayed CPPyNPs was dispersed in a 10-wt% $FeCl_3$ aqueous solution and then stirred for 4 h at 70℃. The subsequent solution was then precipitated with ethanol several times and then dried at 70℃ for 12 h. The hybrid particles obtained were soaked in a 5-wt% $CuCl_2$ ethanol solution, and then exposed to a vaporized mixture of pyrrole and pyrrole-3-carboxylic acid monomers (molar ratio for (pyrrole) : (pyrrole-3-carboxylic acid) = 30 : 1) for 5 min at room temperature in a vacuum chamber, to initiate VDP on the particle surface.

2.1.3.2. Application for endocrine disruptor biosensor

To construct the FET aptasensor, an IDA electrode was treated with 5-wt% aqueous aminosilane (APS) for 6 h to introduce amino groups to the electrode surface. The treated electrode was then exposed to a mixture of 0.1-wt% M_CPPyNP aqueous solution (40 μL) and 1-wt% DMT-MM aqueous solution (40 μL) for 12 h. Subsequently, the coupling reaction to attach the BPA-binding aptamer to the M_CPPyNP surface was carried out using a mixture of the binding aptamer and 1-wt% DMT-MM aqueous solution (40 μL) for 12 h.

Afterward, the A_M_CPPyNP immobilized electrode was rinsed with distilled water and dried at room temperature.

All electrical measurements were conducted using a Keithley 2612A source meter and probe station (MS TECH, Model 4000). To utilize the solution-based measurement, a solution chamber (volume: 200 μL) was designed and used. The change in the current was normalized as follows:

$$[\Delta I/I_0]_{SD} = (I - I_0)/I_0 \times 100$$

where I_0 indicates the initial current, and I is the measured real-time current.

2.2. Multidimensional noble metal/conducting polymer hybrid nanoaprticles

2.2.1. Multidimensional platinum/carboxylated polypyrrole hybrid nanoparticles

2.2.1.1. Fabrication of multidimensional platinum/carboxylated polypyrrole hybrid nanoparticles

Poly(vinyl alcohol) (PVA, Mw 9000), $FeCl_3$ (97%), and $PtCl_4$ (99%) were purchased from Aldrich Co. and used without further purification. Pyrrole (98%) and pyrrole-3-carboxylic acid were obtained from Aldrich and Acros Organics. Dopamine (DA), ascorbic acid (AA), uric acid (UA), epinephrine

(EP), and norepinephrine (NE) were acquired from Sigma Co.

As the starting material, 60 nm of uniform carboxylated polypyrrole nanoparticles (CPPyNPs) were prepared with PVA, $FeCl_3$, and mixture of pyrrole and pyrrole-3-carboxylic acid monomers (molar ratio of pyrrole : pyrrole-3-carboxylic acid = 30 : 1).

The prepared CPPyNPs were mixed with various concentration (0.5×10^{-3} –20×10^{-3} M) of $PtCl_4$ aqueous solutions. Then, 0.01 g of $NaBH_4$ was added to the mixed CPPyNP solution with ultrasonication for 2 h to decorate Pt nanoparticles on the CPPyNP surface. The subsequent solution was precipitated with ethanol several times and then dried at 70℃ for 12 h.

2.2.1.2. Application for dopamine biosensor

To construct the nonenzyme FET sensor, IDA electrode was treated with 5wt% aqueous amino-silane (3-aminopropyltrimethoxysilane, APS) for 6 h to introduce amino groups to the electrode surface. Then, the treated electrode was exposed to a mixture of 0.1 wt% Pt_CPPy aqueous solution (40 μL) and 1 wt% 4-(4,6-dimethoxy-1,3,5–2-yl)-4-methylmorpholinium chloride (DMT-MM) aqueous solution (40 μL) for 12 h. Afterward, the Pt_CPPys immobilized electrode was rinsed with distilled water and dried at room temperature.

All electrical measurements were conducted using Keithley 2612A source meter and probe station (MS TECH, Model 4000) in pH 7.4 of PBS solution.

To utilize the solution-based measurement, a solution chamber (volume: 200 μL) was designed and used. The change in the current was as follows:

$$[\Delta I/I_0]_{SD} = (I - I_0)/I_0 \times 100$$

where I_0 suggests the initial current, and I is the measured real-time current.

2.2.2. Multidimensional porous palladium/carboxylated polypyrrole hybrid nanoparticles

2.2.2.1. Fabrication of multidimensional porous palladium/ carboxylated polypyrrole hybrid nanoparticles

Poly(vinyl alcohol) (PVA, Mw 9000), $FeCl_3$ (97%), hexylamine (C_6H_{13}-NH_2), decylamine ($C_{10}H_{21}$-NH_2), and hexadecylamine ($C_{16}H_{33}$-NH_2) were purchased from Aldrich Chemical Co. and used without further purification. Pyrrole (98 %) and pyrrole-3-carboxylic acid were obtained from Aldrich and Acros organics. $PdCl_2$ (99 %) as precursor of Pd architecture was acquired from Kojima Co.

As starting material, 60 nm of carboxylated polypyrrole nanoparticles (CPPyNPs) were uniformly prepared with PVA, $FeCl_3$, and mixture of pyrrole and pyrrole-3-carboxylic acid monomers (molar ratio of pyrrole : pyrrole-3-carboxylic acid = 30 : 1). The prepared CPPyNPs were mixed with different alkylamine (hexylamine, decylamine, and hexadecylamine) contained ethanolic solution. Then small amount of 4-(4,6-dimethoxy-1,3,5-triazin-2-yl)-4-

methylmorpholinium chloride (DMT-MM) was added to induce covalent bonding of alkylamine. 2 mM of $PdCl_2$ was added to alkyl chain functionalized CPPyNP contained solution. Subsequently, 0.01 g of $NaBH_4$ was added to the mixed solution with ultrasonication for 2 h to decorate porous palladium layer on the CPPy surface. The subsequent solution was precipitated with ethanol and water for several times and then dried at 70℃ for 12 h.

2.2.2.2. Application for hydrogen gas chemical sensor

M_PdCPPys (0.5 wt% in ethanol solution) were prepared by ultrasonication for deposition onto an as-prepared inter-digitated array (IDA) electrode. The M_PdCPPy sample was introduced by spin-coating (1000 rpm, 45 s) to create a uniform array of particles. The as prepared IDA electrode measured resistance changes in the particles with a source-meter connected to a computer. The M_PdCPPy sensors were placed in a vacuum chamber with a vapor inlet/outlet pressure of 10^0 Torr. Various concentration of hydrogen gas (0.1 - 100 ppm) was injected into the chamber using a mass flow controller (MFC, KNH Instruments). The real-time responses from the M_PdCPPys were systematically evaluated by normalized resistance changes ($\Delta R/R_0$). The normalized resistance change ($\Delta R/R_0$) of the M_CPPy based sensor was monitored in real-time during exposure to various gases at a constant applied current (10^{-6} A) until saturation was reached. $\Delta R/R_0$ of the M_PdCPPys is

given by the following equation:

$$\Delta R/R_0 = (R - R_0)/ R_0$$

where R_0 is the initial resistance and R is the measured real-time resistance, respectively. After the M_PdCPPys were exposed to various concentration of hydrogen gas for several minutes, the gas vapor was then replaced by compressed air to remove any molecules attached to the nanomaterials. This process was repeated several times. Vapor/air was supplied at various flow rates ranging from 2 to 8 slm and 1 to 5 sccm, as controlled by the MFC.

2.3. Instrumental analysis

Transmission electron microscopy (TEM) and high-resolution transmission electron microscopy (HR-TEM) images were obtained with a JEOL JEM-200CX and JEOL JEM-3010 system, respectively. During the sample preparation, the nanomaterials, diluted in ethanol, were cast onto a copper grid. A JEOL 6700 was used to obtain field-emission scanning electron microscopy (FE-SEM) images. X-ray diffraction (XRD) patterns and X-ray photoelectron spectroscopy (XPS) spectra were recorded using the M18XHF SRA (MAC Science Co.) and AXIS-His (KRATOS) systems, respectively. Brunauer-Emmett-Teller (BET) surface areas were measured using a surface area/porosimetry analyzer (ASAP2010, Micromeritics). Thermogravimetric

analysis (TGA) was recorded on a Pyris6 (Perkin-Elmer). The measurement of the electrical conductivity was carried out at ambient temperature with a source meter, using the four-probe method. Electron energy loss spectroscopy (EELS) mapping of the hybrid nanoparticles was performed with a JEOL JEM 2100F. The scanning TEM/energy dispersive X-ray (STEM-EDX) line analysis data was obtained with a Technai F20 (FEI) spectrometer. Measurement of the electrical conductivity was accomplished *via* the four-point probe method using a source-meter at ambient temperature.

3. RESULT AND DISCUSSION

3.1. Multidimensional metal oxide/conducting polymer hybrid nanoparticles

3.1.1. Multidimensional polypyrrole/iron oxyhydroxide hybrid nanoparticles

3.1.1.1. Fabrication of multidimensional polypyrrole/iron oxyhydroxide hybrid nanoparticles

Figure 13 illustrates the overall procedure for the fabrication of multidimensional hybrid PPy nanoparticles, based on the dual-nozzle electrospray method. First, 60 nm diameter PPy particles were prepared using a monodisperse method as shown in Figure 14.[55] PPy nanoparticles were stirred in an $FeCl_3$ aqueous solution at room temperature to induce covalent bonding between the Fe^{3+} ions and the partial negative charge of the N atom in the pyrrole structure. The mixed PPy solutions were electrosprayed by the outer part of the dual-nozzle, while compressed air flowed through the inner nozzle. The electrosprayed PPy (E_PPy) particles were collected by a Petri dish collector, under a continuous high voltage. During the electrospray process, FeOOH particle formation on the PPy surfaces was facilitated by

several factors (Figure 15). The high positive voltage applied allowed uniform dispersion of Fe^{3+} ions on the PPy surfaces, resulting in positively charged electrosprayed PPy nanoparticles. Additionally, the mechanical force, provided by the compressed air flow through the inner part of the dual-nozzle, broke up the mixed PPy solution drops into small nanosized droplets; this reduced the likelihood of particle aggregation (Figure 16a,b). Finally, the Fe^{3+} ions reacted with the hydroxide ions in the collector; thus, when the electrosprayed particles were collected in a solution containing NaOH, the Fe^{3+} ions reacted with the hydroxide ions to form FeOOH particles, as described by the following reaction:[213,214]

$$Fe^{3+} + 3OH^- \rightarrow FeOOH + H_2O$$

Figure 16c exhibits the E_PPy nanoparticles decorated with about 3 nm diameter metal particles on their surface. High-resolution transmission electron microscopy (HR-TEM) images indicated an interplanar spacing between the metal particles of 0.29 and 0.26 nm for the (100) and (021) planes, respectively, corresponding to the α-FeOOH lattice structure (Figure 16d).

The E_PPy nanoparticles were stirred in an $FeCl_3$ aqueous solution at 70°C for 4 h to induce growth of FeOOH needles on the surface. The Fe^{3+} ions in the solution were converted into FeOOH needles at the decorated FeOOH particle sites (*i.e.*, the FeOOH particles acted as nucleate sites during this process). The

morphology and needle density were controlled by the concentration of the $FeCl_3$ aqueous solution, which varied from 0.5 to 10 wt%. This resulted in multidimensional FeOOH nanoneedle-decorated polypyrrole hybrid nanoparticles (denoted as PFFs), with various needle morphologies on the surface.

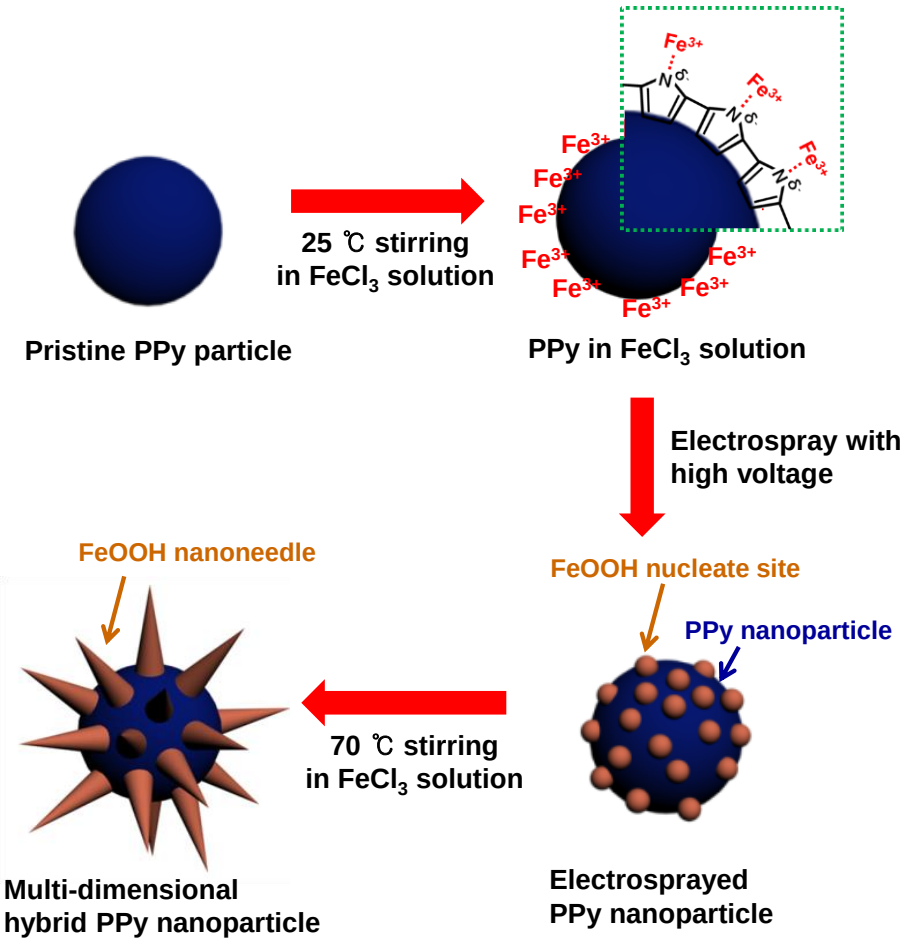

Figure 13. Illustrative diagram of the sequential fabrication steps for multidimensional hybrid polypyrrole nanoparticles.

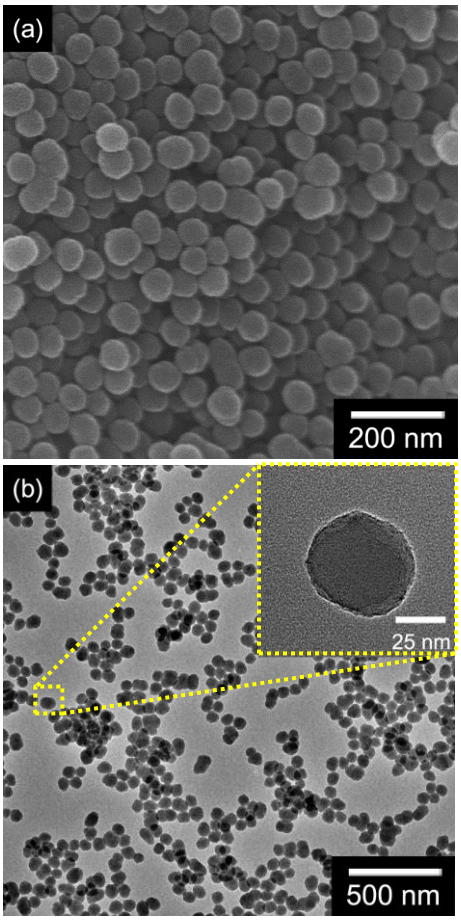

Figure 14. (a) FE-SEM and (b) TEM (inset: high resolution TEM) images of pristine PPy with 60 nm-diameter.

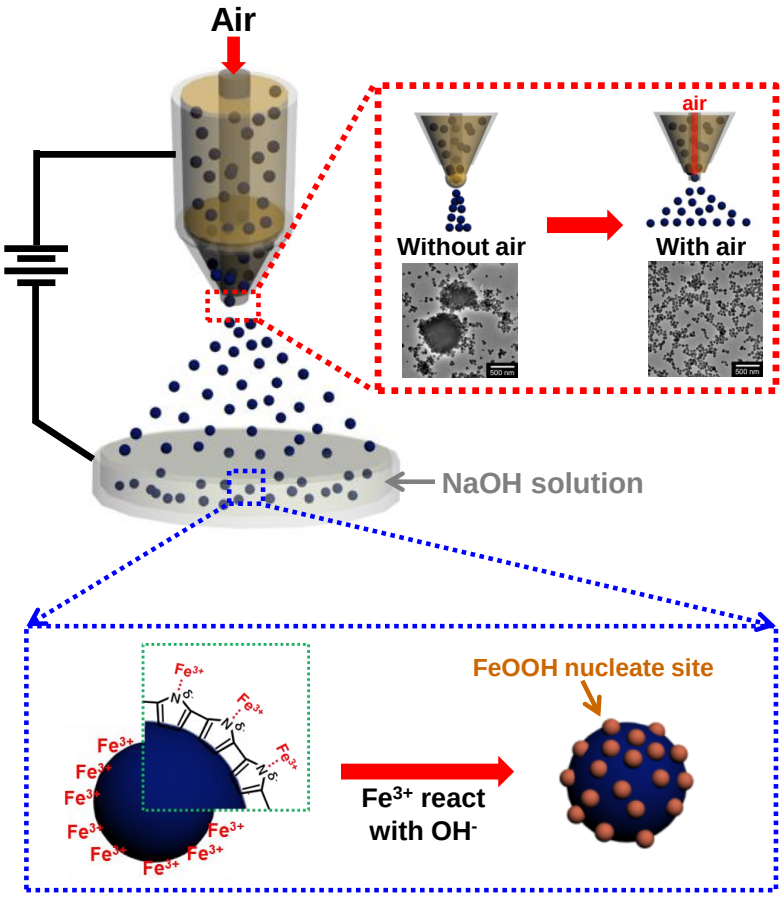

Figure 15. Schematic illustration of the formation of FeOOH nucleate site by using dual-nozzle electrospray method with compressed air blowing (red inset: comparison of electrosprayed particles by control compressed air blowing).

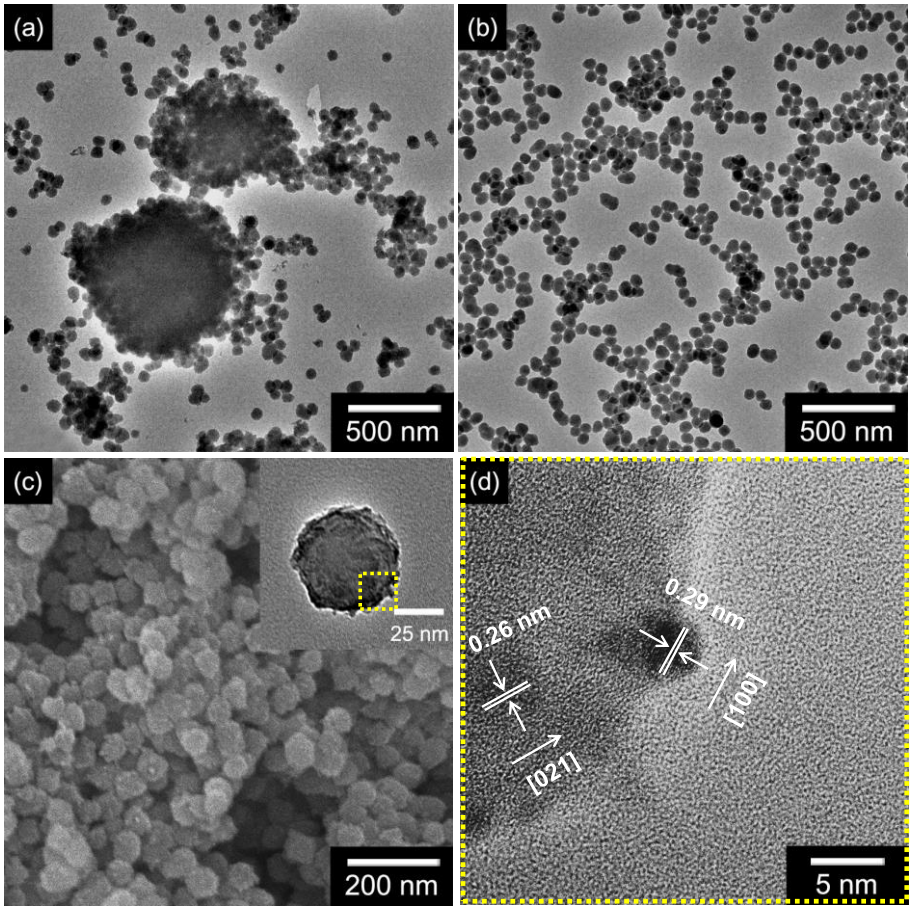

Figure 16. TEM images of E_PPy nanoparticles (a) without compressed air and (b) with compressed air during electrospray process. (c) FE-SEM and TEM (inset) image of E_PPy nanoparticles after reacted with hydroxide (OH^-) ions. (d) HR-TEM image of FeOOH nucleate sites on the E_PPy nanoparticle.

The nanostructures of the hybrid PFFs had different FeOOH nanoneedle configurations. The PFFs with 0.5, 2.0, 5.0, and 10.0 wt% FeOOH precursors are denoted as PFF_0.5, PFF_2, PFF_5, and PFF_10, respectively (Figure 17). TEM and HR-TEM images show that the length and diameter of the FeOOH nanoneedles increased with the precursor concentration. At low concentrations (0.5 wt%), the about 5 nm diameter FeOOH particles decorated the surface, instead of nanoneedles. However, the 10 wt% FeOOH precursor concentration resulted in the formation of nanoneedles, about 40 nm in length and about 10 nm in diameter. The FeOOH density also increased with precursor concentration. The HR-TEM image of FeOOH points out an interplanar spacing of 0.29 and 0.26 nm for the (100) and (021) of α-FeOOH, respectively, and confirmed growth of pure, crystalline nanoneedles following treatment (Figure 17f).

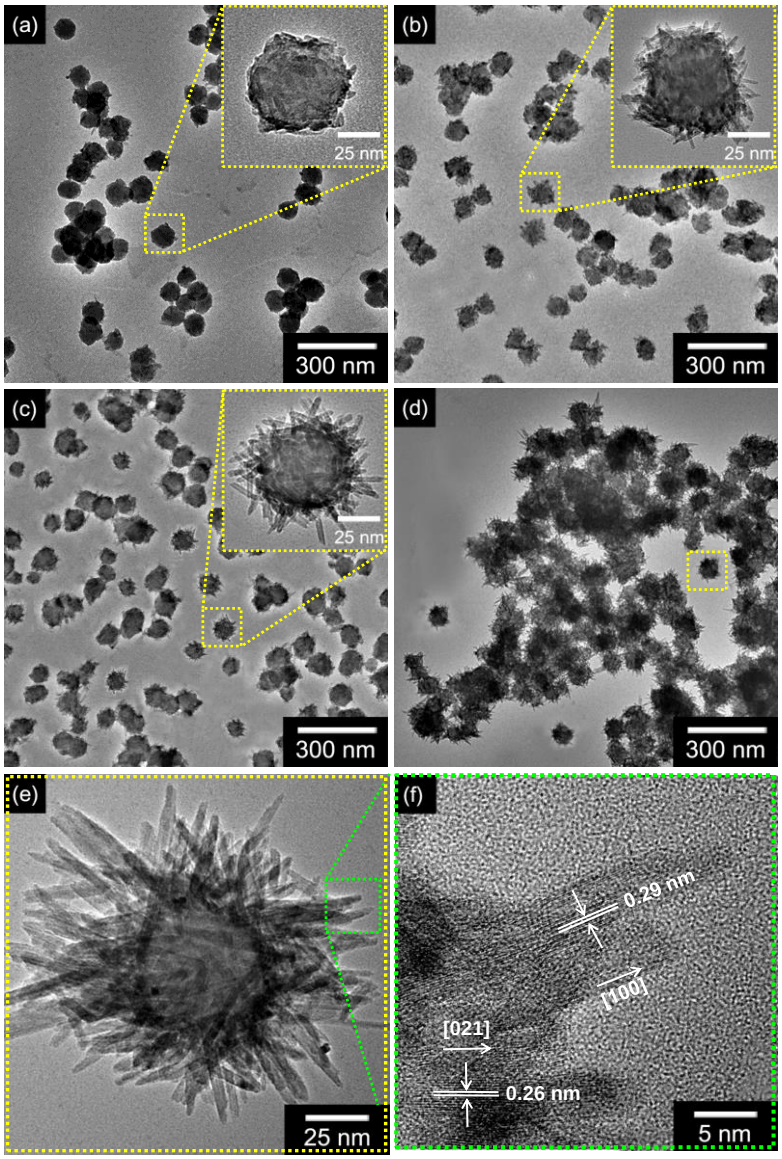

Figure 17. Low- and high (inset)-resolution TEM images of hybrid PFF nanoparticles with various concentration of $FeCl_3$ solutions; (a) 0.5 wt%, (b) 2.0 wt%, and (c) 5.0 wt%, and 10 wt% hybrid PFF nanoparticles with (d) low resolution TEM, (e) high resolution TEM, and (f) HR-TEM images of FeOOH nanoneedles on the PPy surface.

The X-ray diffraction (XRD) patterns of the particles are shown in Figure 18. The peak of the inorganic material in the E_ PPy and hybrid PFF particles can be well indexed to the α-FeOOH (JCPDS 29-713), indicating the formation of α-FeOOH nanostructures on the PPy surface. As expected, the peak intensities for the α-FeOOH nanoneedles increased due to the enhancement in the nanoneedle density, following the stirring reaction procedure. The broad diffraction peaks at 25.6 cm^{-1} were observed for all samples, indicating an identical crystalline PPy structure for all of the samples.

The chemical composition of the hybrid materials was also confirmed by X-ray photoelectron spectroscopy (XPS). Figure 19a dispalys the complete spectra over the range of 0 - 1200 eV. These overview spectra revealed that C, N, O, and Fe atoms were illustrated in the PFF_10 and E_PPy samples, whereas only C, O, and N were present in the pristine PPy nanoparticles. The N 1s peak was attributed to the N component in the pyrrole structure (pyrrolylium nitrogen component and the positively charged N atoms). The high-resolution XPS spectra for the C 1s region around 285 eV are demonstrated in Figure 19b; this peak was deconvoluted into four components. The peak at 284.3 eV was attributed to C=C bonds, and the 285.3 eV peak corresponded to the C-C bond. The C-O and C-N groups exhibited peaks at 286.6 and 284.9 eV, respectively. The C 1s peaks for the hybrid PFF_10 and

E_PPy were not shifted relative to those for the pristine PPys, confirming that the structure of the PPys remained unchanged after the formation of FeOOH nanoneedles. Figure 19c shows the O 1s band of particles deconvoluted into several components. The peak at 533.0 eV represented the C-O bonds from the PPy structure component. The peaks at 531.7 eV and 529.6 eV were attributed to the OH^- and O^{2-} components in the FeOOH structure. Figure 19d describes the high-resolution XPS spectra for the Fe 2p peak. Spin-orbit components $2p_{3/2}$ and $2p_{1/2}$ were observed near 708.5 eV and 722.2 eV, indicating that the valance state of Fe was +3. Thus, it can be concluded that the FeOOH nanoneedles were composed of Fe(III) and O, as confirmed by XRD results.

Additionally, the decoration amounts of FeOOH were quantified by thermogravimetric analysis (TGA) method (Figure 20). There is small weight loss around 100℃ in the TGA curve owing to evaporation vapor in the composite structures. Then, all the above TGA analysis could be confirmed by drastic weight loss in the curve at the corresponding temperature from 200 to 450℃. After 450℃, there was no change in weight loss, indicating the formation of pure metal oxide. As a result, the amount of metal oxide decoration on PPy surface increased from 10.4 wt% to 56.7 wt% with enhancing metal precursor ($FeCl_3$) contained aqueous solution from 0.5 wt% to 10.0 wt% during heat stirring process.

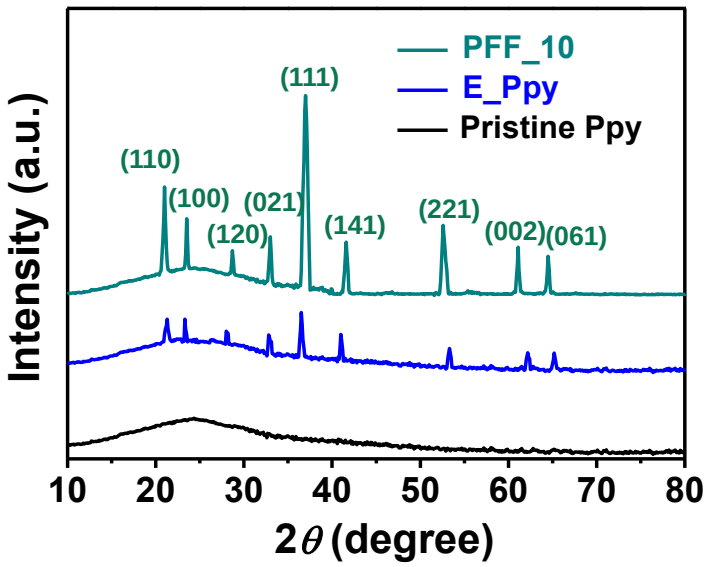

Figure 18. XRD pattern of various PPy nanoparticles (black: pristine PPy; blue: E_ PPy; green: hybrid PFFs).

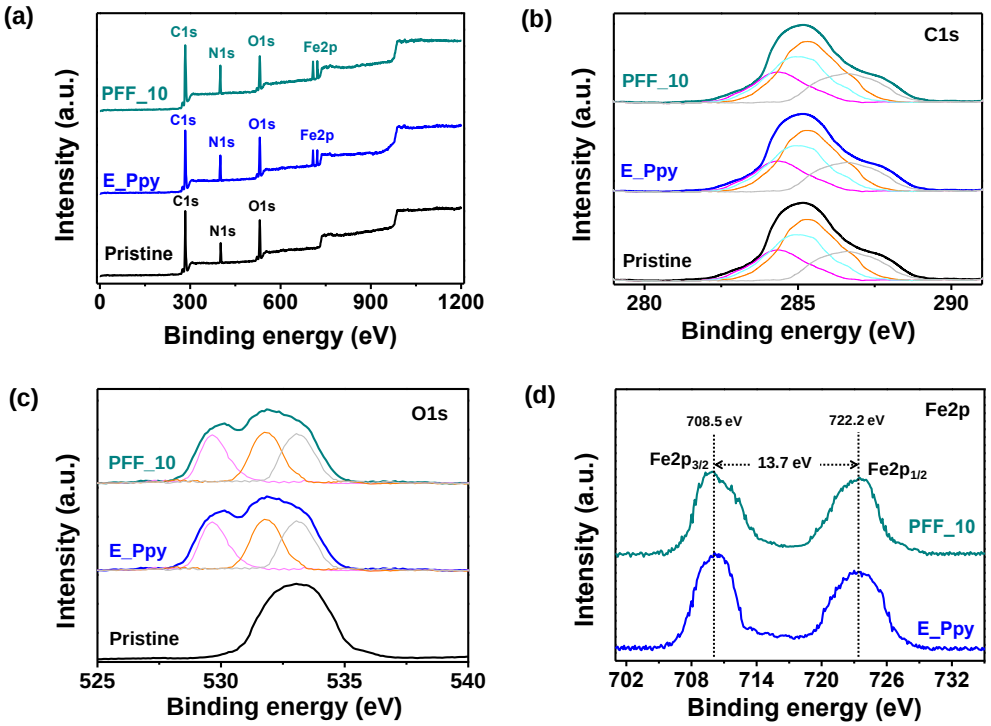

Figure 19. XPS patterns of (a) fully scanned spectra and high resolution of (b) C 1s, (c) O 1s, and (d) Fe 2p of hybrid PPy nanoparticles (black : pristine PPy; blue : E_PPy; green : PFF_10).

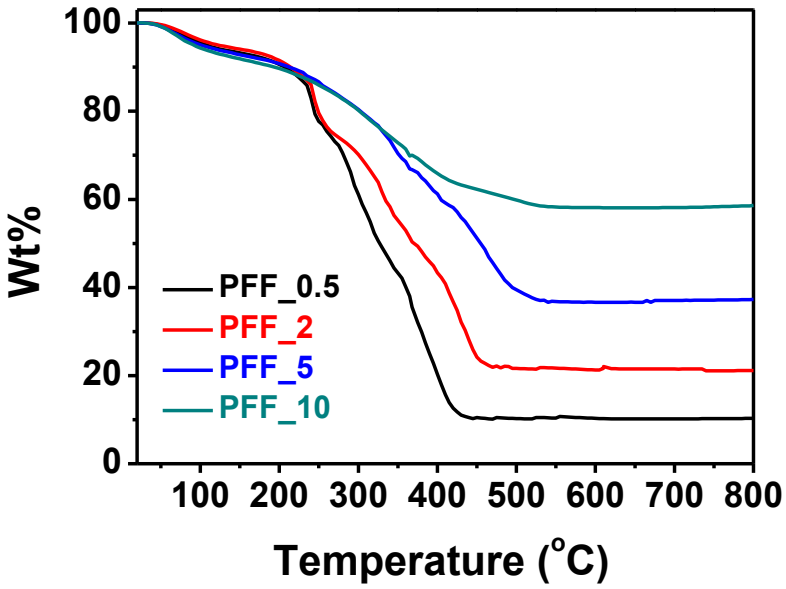

Figure 20. TGA analysis of various hybrid PFF nanoparticles (black: PFF_0.5; red: PFF_2; blue: PFF_5; green: PFF_10).

Figure 21 presents the N_2 adsorption/desorption isotherms obtained using the Brunauer-Emmett-Teller (BET) method for the hybrid PPy nanoparticles. The surface area increased from 50 m^2 g^{-1} for pristine PPy particles to 227 m^2 g^{-1} for PFF_10. This increase in the surface area was caused by the enhancement in the nanoneedle density and size on the surface; specifically, the surface area of PFF_10 was *ca*. 4 times larger than that of the pristine PPy particle. Additionally, the surface areas of E_PPy and PFF_0.5 were 60 m^2 g^{-1} and 65 m^2 g^{-1}, similar to that for pristine PPy (Figure 22). Therefore, the $FeCl_3$ solution concentration during the stirred heat reaction had a significant effect on the surface area of the hybrid PFFs, due to the enhancement of the decorated FeOOH nanoneedle size and density.

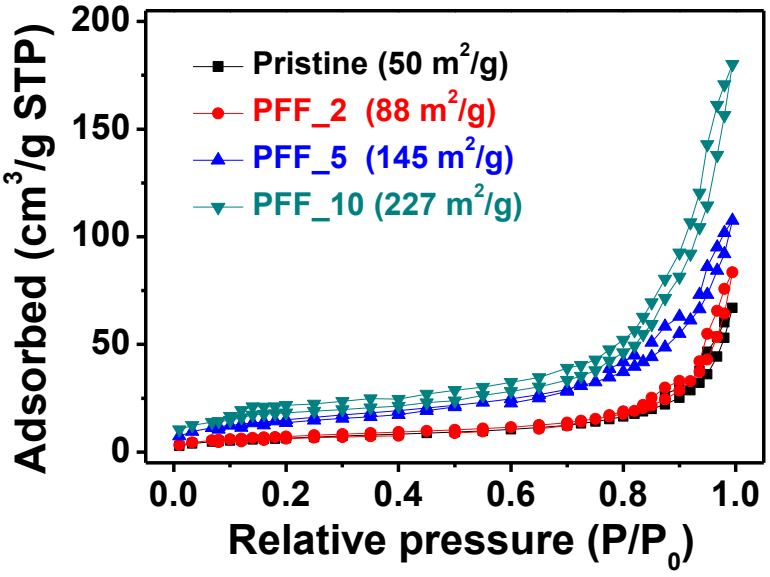

Figure 21. Nitrogen adsorption-desorption isotherm of various hybrid FeOOH/PPy nanoparticles (pristine PPy: black; PFF_2: red; PFF_5: blue; PFF_10: green).

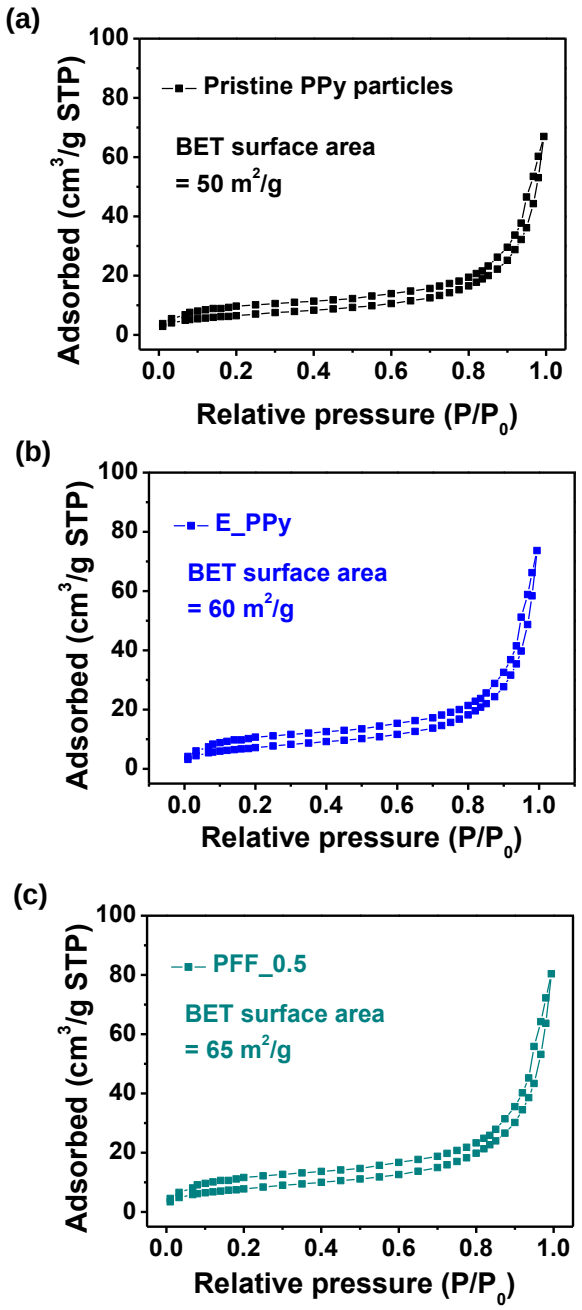

Figure 22. Nitrogen adsorption-desorption isotherm of pristine PPy particles (black), E_PPy (blue), and PFF_0.5 (green).

3.1.1.2. Application for nerve agent simulant chemical sensor

Several approaches were explored to optimize the sensor performance, *i.e.*, the conductive pathway and effective surface area. Figure 23 illustrates the current–voltage (I–V) curves of the hybrid PFFs; the results indicated that the hybrid nanoparticles were in good electrical contact with the sensor substrate. The transducer arrangement was thought to improve the conductive pathway, *i.e.*, to increase the DMMP detection sensitivity. The randomly-stacked arrangement of PFFs were prepared by the drop-casting method had a higher contact resistance than the uniform array obtained by spin-coating, due to interruption of the conductive pathway through the accumulated particle–particle assembly. Therefore, PFFs were deposited on the electrode by spin-coating to determine the sensing performance in real-time with minimized contact resistance.

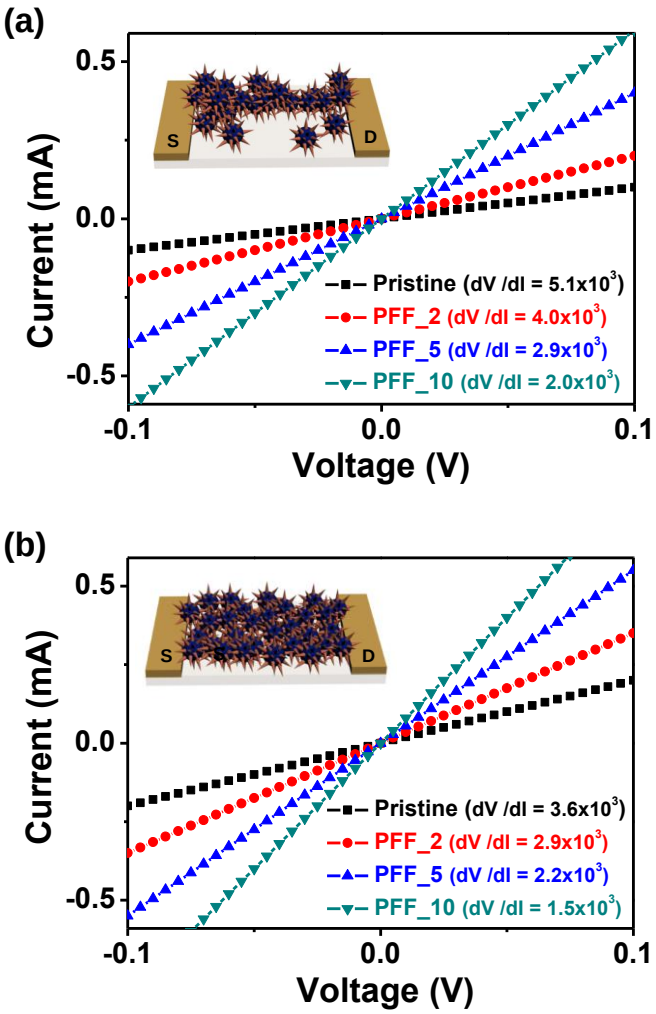

Figure 23. I-V curves of hybrid PFF nanoparticles deposited on IDA by using (a) drop-casting and (b) spin-coating method (pristine PPy: black; PFF_2: red; PFF_5: blue; PFF_10: green).

The uniformly-dispersed PFFs on the sensor substrate rapidly detected DMMP molecule at room temperature. The sensing mechanism of the hybrid PFFs is described below (Figure 24). The FeOOH surfaces adsorbed to DMMP by charge interaction and hydrogen bonding through the −OH group of FeOOH and the phosphate group of the DMMP structure. DMMP is a strong electron donor; thus, when the PFFs were exposed to DMMP vapors, electrons were transferred from DMMP to FeOOH; these transferred electrons flowed to the PPy structure, leading to a decrease in the number of holes in the PPy and increasing electrical resistance (because PPy acts as a p-type transducer).[215,216] The FeOOH nanoneedles performed critical effect to DMMP sensing in the detecting mechanism. First, it bonded to DMMP molecule through not only charge interaction but also hydrogen bonding of oxygen atom in the DMMP and −OH group of FeOOH that increased functional site to DMMP molecule. Second, enlarged surface area by vertically aligned on the PPy surface is also increasing DMMP sensing active site. As a result, enhancement adsorbed amount of vapors increased sensitivity to DMMP molecules.

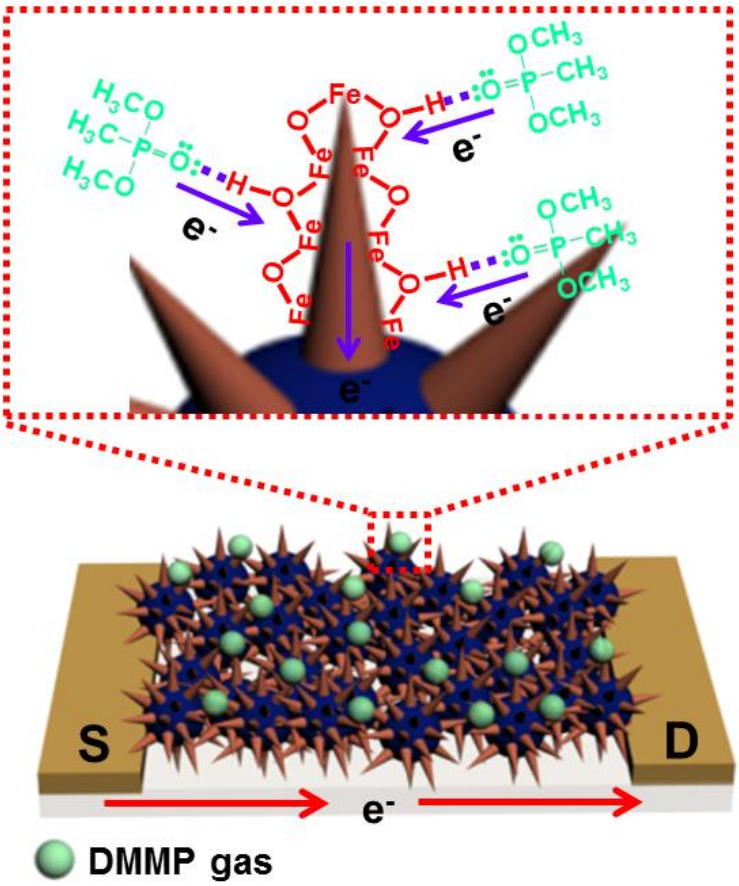

Figure 24. DMMP vapor detection mechanism of hybrid PFF nanoparticles at room temperature.

The sensing performance of the DMMP sensor was affected by the decorated FeOOH populations and morphologies of the surfaces. The real-time responses of various PPy nanoparticles were measured for different concentrations of DMMP vapor. First, pristine PPy and E_PPy nanoparticles, without FeOOH needles, were tested (Figure 25a). In the pristine PPy case, there were no functional sites to attract DMMP molecules. In contrast, the E_PPy nanoparticles had numerous FeOOH nucleate sites to attract the DMMP molecule to the PPy surface. However, the nucleate site is quite small in size; thus, there was little interaction with the DMMP molecule. As a result, the sensitivity of the DMMP sensor was absent or low for the pristine PPy and E_PPy particles. In contrast, for the hybrid PFFs, the FeOOH nanoneedle morphology and density on the PPy surfaces significantly affected the sensing performance of the DMMP vapor sensor. When the hybrid PFF sensors were exposed to DMMP vapor at room temperature, excellent sensitivity and rapid response/recovery times were observed. Figure 25b suggests the sensor response upon sequential exposure as a function of analyte concentration. The sensitivity of hybrid PFFs increased as the size and density of FeOOH needles on the surface increased; specifically, PFF_10 was capable of detecting DMMP concentrations as low as 0.1 ppb at room temperature. Furthermore, nanoneedle size and density influence to the response and recovery times to the

target gas. Figure 25c shows the real-time response to DMMP of hybrid PPy particles. The response of the E_PPy nanoparticles was 2.0 s; the hybrid PFF sensor with PFF_2, PFF_5, and PFF_10 exhibited response times of 2, 2, and 1.5 s, respectively. These response times were attributed to the incorporation of FeOOH nanoneedles on the PPy surfaces, leading to protuberances and a subsequent increase in the surface area. Therefore, the rapid response occurred because DMMP molecules rapidly diffused into the hybrid PFF nanoparticles due to the high surface area. In contrast, recovery times varied from 3.5 s for the E_PPy to 8.5 s for PFF_10 (PFF_2: 5.5 s; PFF_5: 7.5 s); this effect was attributable to the interaction of the FeOOH nanoneedles with the DMMP molecule (Figure 25d). Thus, the E_PPy sensor indicated *ca*. 3 times faster recovery time than the PFF_10 sensor, owing to its minimal interaction with the DMMP molecule. As a result, the sensing ability of different PPy particles with enhancing surface area is suggested in Table 1. In addition, increasing PPy nanoparticle diameters (60 to 150 nm) decrease sensitivity to DMMP vapor because of reducing surface area (Figure 26).

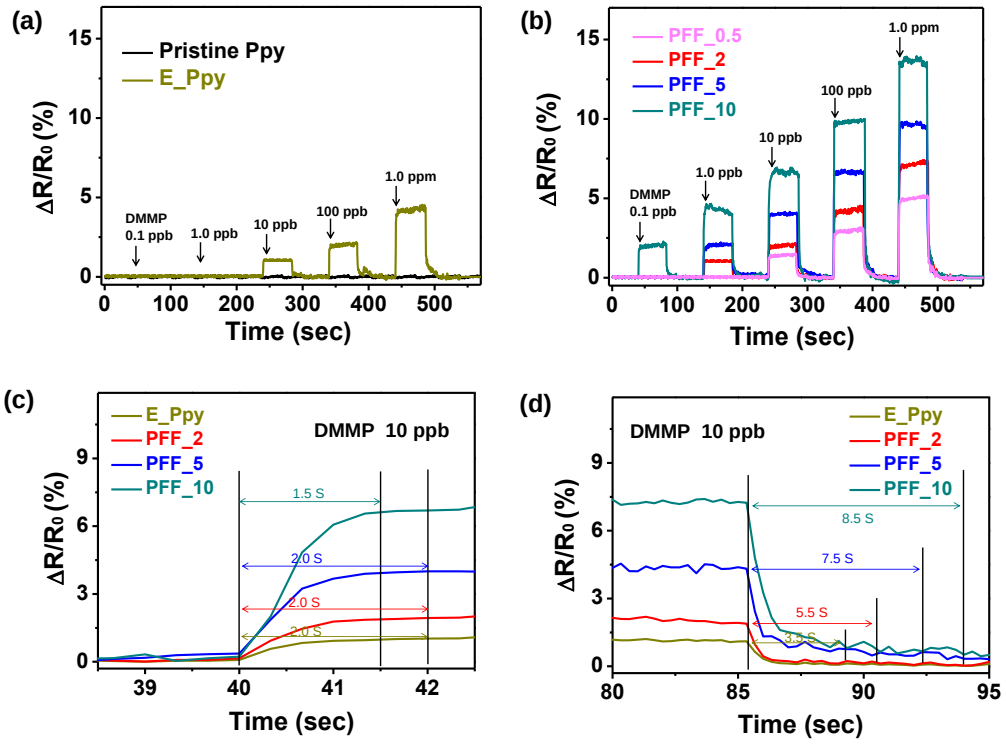

Figure 25. Reversible and reproducible responses are measured at a constant current value (10^{-6}A) with various amount and type of FeOOH on the PPy surfaces. Normalized resistance changes upon sequential exposure to various DMMP concentrations of (a) pristine (black), E_PPy (yellow) and (b) hybrid PFF nanoparticles (pink: PFF_0.5; red: PFF_2; blue: PFF_5; green: PFF_10). The (c) response and (d) recovery times of hybrid PPy nanoparticles (yellow: E_PPy; red: PFF_2; blue: PFF_5; green: PFF_10) at 10 ppb of DMMP vapor at room temperature.

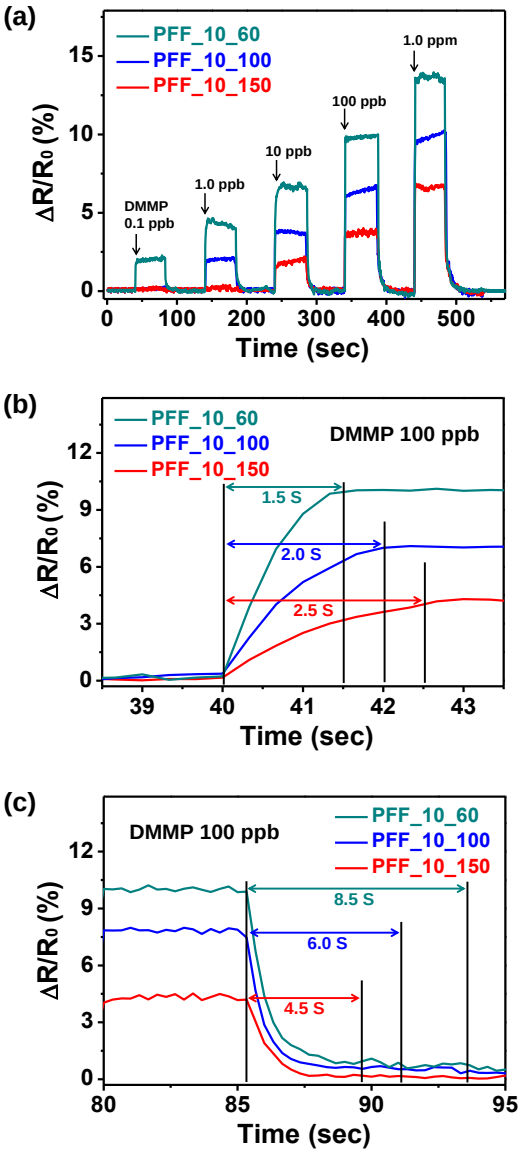

Figure 26. (a) Normalized resistance changes upon sequential exposure to various DMMP concentrations with different diameters of PFF_10. The (b) response and (c) recovery times of different diameters of PFF_10 at DMMP vapor 100 ppb at room temperature (green: PFF_10 with 60-nm diameter; blue: PFF_10 with 100-nm diameter; red: PFF_10 with 150-nm diameter).

Table 1. BET surface area and sensing ability of various FeOOH decorated polypyrrole nanoparticles to DMMP vapor.

	BET area[a] (m^2 g^{-1})	MDL[b]	Response time (s)	Recovery time (s)
PPy	50	-	-	-
E_PPy	60	10 ppb	2.0	3.5
PFF_0.5	65	10 ppb	2.0	3.5
PFF_2	88	1 ppb	2.0	5.5
PFF_5	145	1 ppb	2.0	7.5
PFF_10	227	0.1 ppb	1.5	8.5

[a] Surface area calculated from Brunauer-Emmett-Teller method

[b] Minumum detactable level

Figures 27a and b present the electrical response of various PPy nanoparticles upon periodic exposure to 10 ppb of DMMP vapor at room temperature. With the exception of pristine PPy, these particles revealed similar response sensitivity with enhanced sensing number without retardation of the response or recovery times. Moreover, hybrid PPy nanoparticle gas sensors maintained their sensing ability after 100 cycles (Figure 27c). Furthermore, the morphology of PFFs after DMMP vapor exposure was maintained without collapse of nanoneedles (Figure 28). Figure 29 represents the sensitivity (S, defined as the normalized resistance change measured after a 10 s vapor exposure) changes of the sensors as a function of gas concentration; note that the sensitivity should be zero at 0 ppb. At low concentrations (< 0.1 ppb), the hybrid PFF sensors showed nonlinear changes in sensitivity. Linear behavior was observed over a wide range of concentrations (0.1~1000 ppb). Therefore, the hybrid PFF gas sensors demonstrated reversible, reproducible responses to different analyte concentrations, and their responses were more pronounced as the gas concentration increased. Additionally, these hybrid PFFs can also detect other organophosphate nerve agent simulants such as diethyl chlorophosphonate (DCP) and diethyl cyanophosphonate (DCNP) (Figure 30).

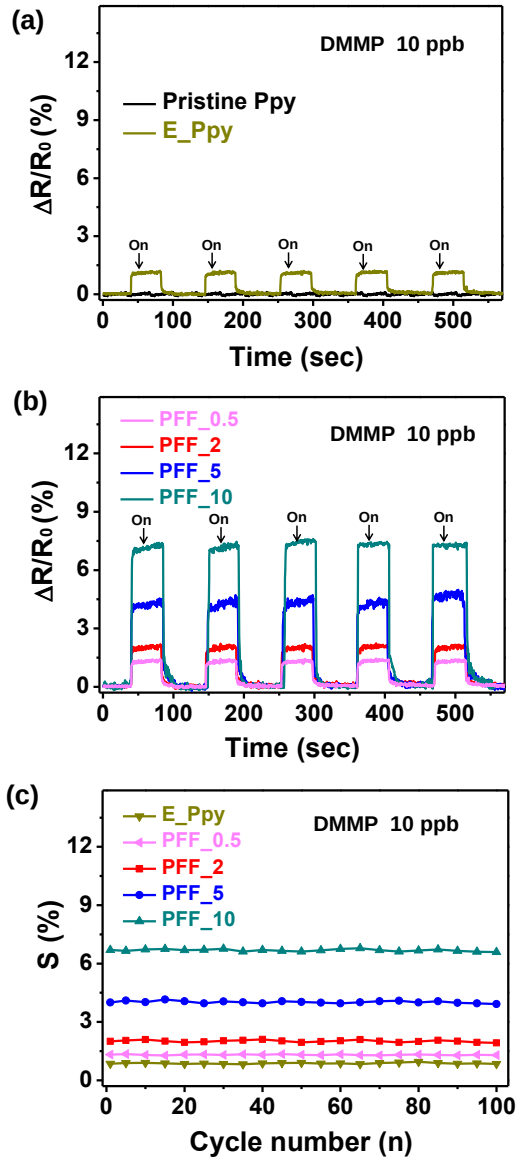

Figure 27. Periodic exposure to DMMP vapor of 10 ppb of (a) pristine (black), E_PPy (yellow) and (b) hybrid PFF nanoparticles (pink: PFF_0.5; red: PFF_2; blue: PFF_5; green: PFF_10). (c) Sensitivity changes of hybrid PFF nanoparticles with periodic exposure to DMMP vapor of 10 ppb for 100 cylcles (yellow: E_PPy; pink: PFF_0.5; red: PFF_2; blue: PFF_5; green: PFF_10).

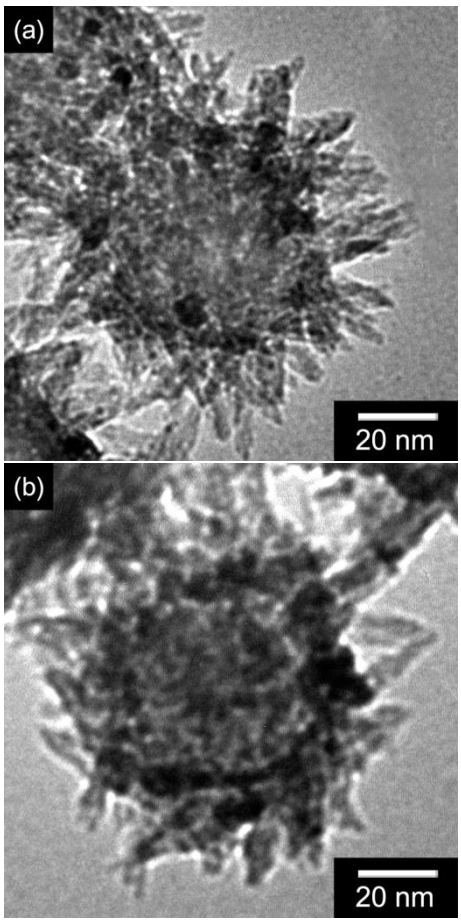

Figure 28. TEM images of PFF_10 nanoparticle (a) before DMMP vapor sensing and (b) after exposure to DMMP vapor of 10 ppb for 100 cycles.

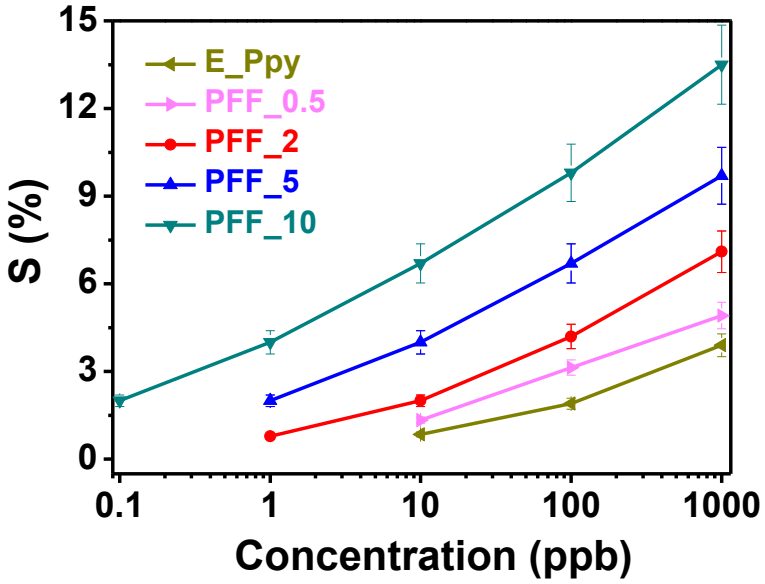

Figure 29. Calibration line of FeOOH decorated PPy particles as a function of DMMP vapor concentration (yellow: E_PPy; pink: PFF_0.5; red: PFF_2; blue: PFF_5; green: PFF_10).

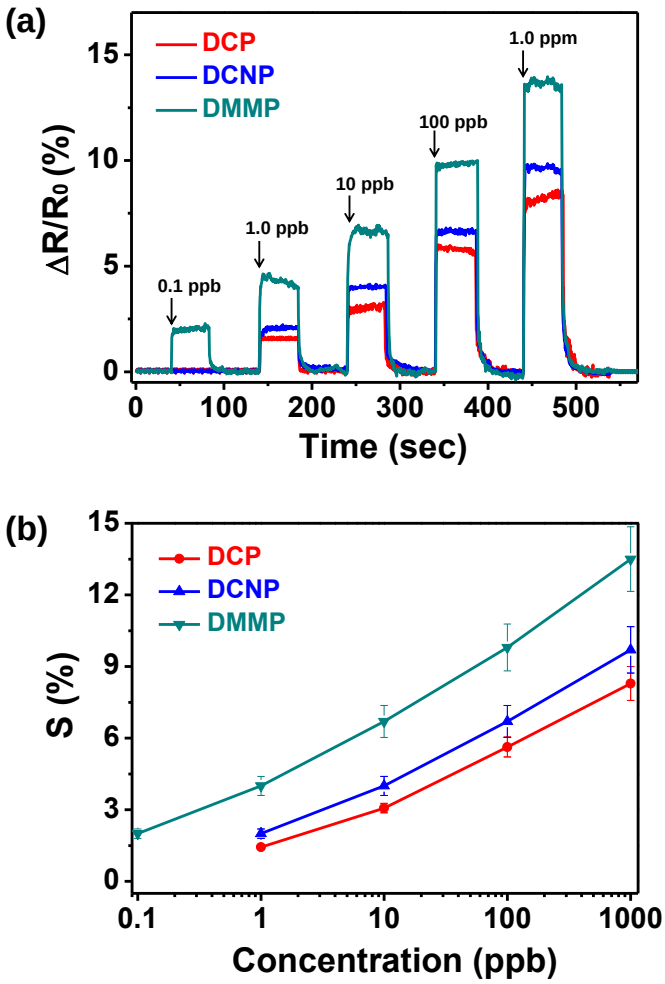

Figure 30. Reversible and reproducible responses of PFF_10 are measured at a constant current value (10^{-6}A) with different target analytes. (a) Normalized resistance changes upon sequential exposure to various analyte concentrations. (b) Calibration line of PFF_10 particles as function of analyte concentration (green: DMMP; blue: diethyl cyanophosphonate (DCNP); red: diethyl chlorophosphonate (DCP)).

3.1.2. Multidimensional polypyrrole hybrid nanoparticles

3.1.2.1. Fabrication of multidimensional polypyrrole hybrid nanoparticles

Figure 31 presents the fabrication procedure for the U_PPy particles, based on the dual-nozzle electrospray and VDP methods. The diameters of the pristine PPy nanoparticles (as starting materials) were controlled by the amount of the pyrrole monomer used during fabrication. Figure 32 shows aggregate-free, pristine PPy nanoparticles with various diameters (30, 60, and 100 nm). The PPy particles were mixed with an $FeCl_3$ aqueous solution. The mixed solution was then electrosprayed using a dual-nozzle consisting of the PPy mixed solution (outer part) and compressed air (inner part). The electrosprayed particles were collected in a Petri dish collector containing a NaOH aqueous solution; this setup enabled the creation of FeOOH nucleated sites on the surface (Figure 33a). During the electrospray process, aggregate-free PPy particles with nucleated sites on the surface (E_PPy) were fabricated. First, because of the high positive voltage supplied, the Fe^{3+} ions were dispersed uniformly over the PPy surfaces, thereby resulting in positively charged, electrosprayed PPy particles. Second, the mechanical force of the compressed air owing through the inner nozzle broke up the PPy mixture drops into scattered, nanoscale droplets. Third, Fe^{3+} ions were converted into FeOOH particles, due to the reaction between the Fe^{3+} ions and the OH^- ions in the Petri

dish collector, as described in section 3.1.1.1.

Figure 33b displays HR-TEM images of nucleated sites; the interplanar spacing was 0.29 nm and 0.26 nm for the (100) and (021) planes, respectively, corresponding to an α-FeOOH lattice structure. The E_PPy particles were then mixed with the $FeCl_3$ aqueous solution at 70℃ for 4 h to induce the growth of FeOOH needles on the surface at these sites. During the stirring process, Fe^{3+} ions in the solution were converted to FeOOH needles at the FeOOH nucleated sites, as illustrated in Figure 34. Then, the FeOOH-decorated hybrid PPy particles (PFFs) were dipped into 5 wt% $CuCl_2$ ethanol solution. As a result, Cu cations were adsorbed on the FeOOH needle surface on account of the charge–charge interaction between the Cu^{2+} ions and the partial negative charge of the oxygen atoms in the FeOOH structure (red inset of Fugure 31).

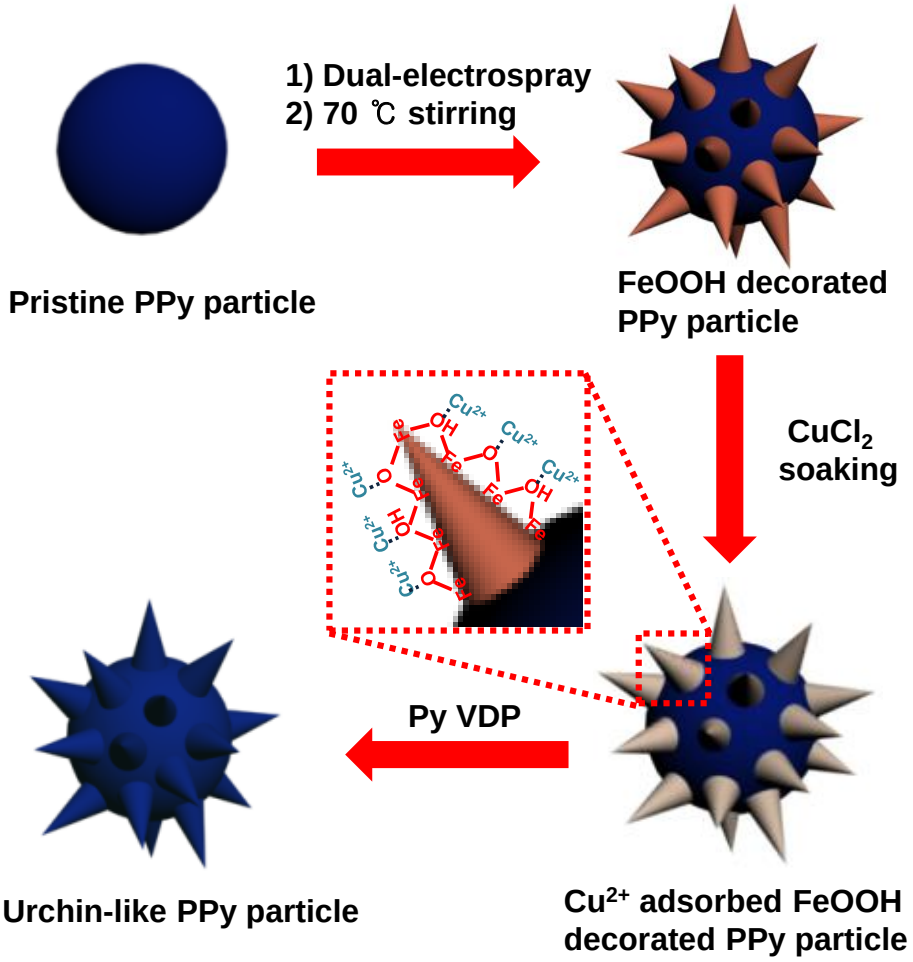

Figure 31. Illustrative diagram of the sequential fabrication steps for multidimensional urchin-like polypyrrole hybrid nanoparticle (U_PPy).

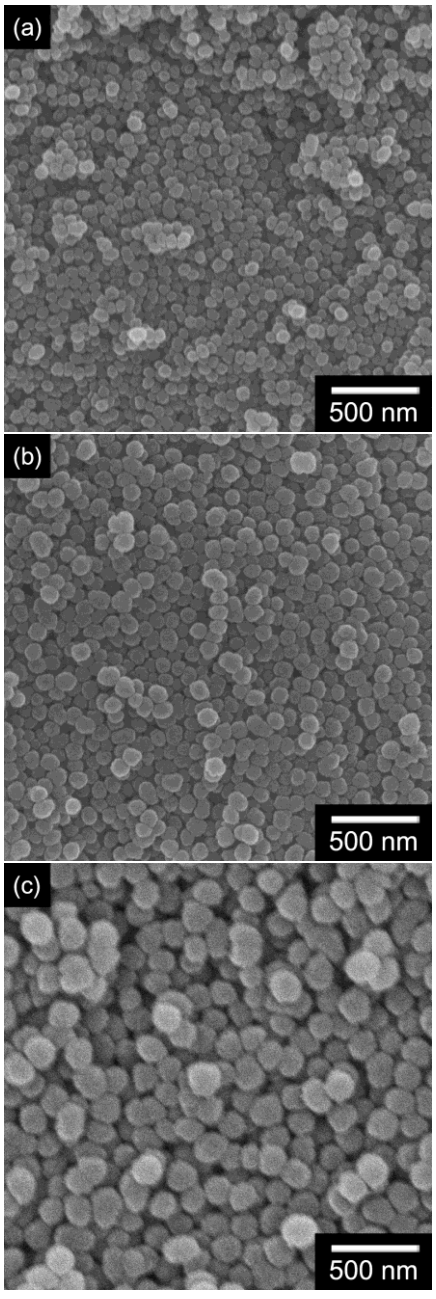

Figure 32. FE-SEM images of polypyrrole (PPy) particles diameter with (a) 30 nm, (b) 60 nm, and (c) 100 nm.

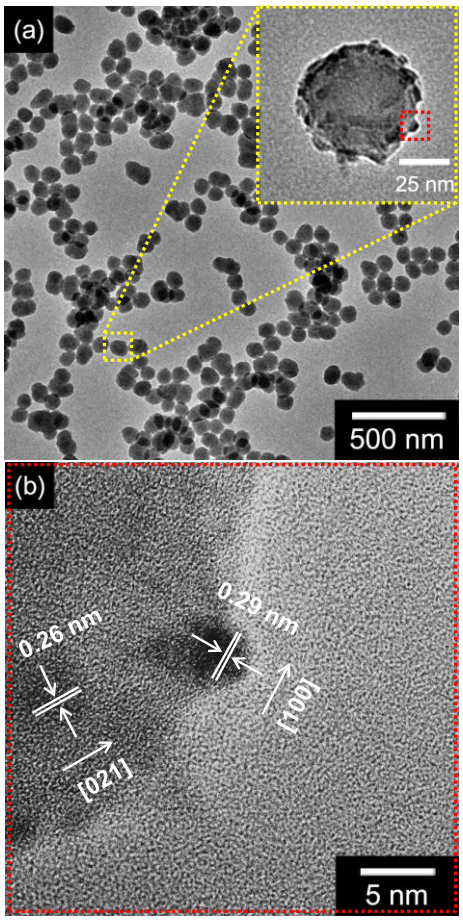

Figure 33. (a) TEM (inset: enlarged TEM) and (b) HR-TEM images of electrosprayed polypyrrole nanoparticles (E_PPys).

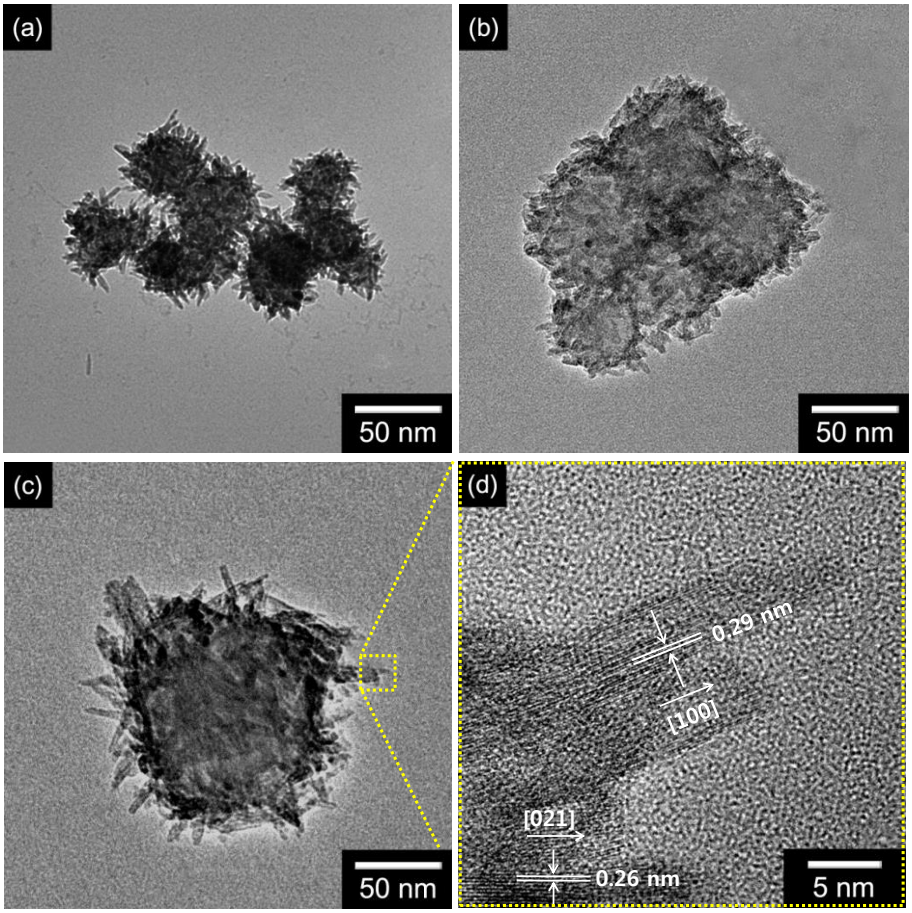

Figure 34. TEM images of FeOOH nanoneedle decorated polypyrrole nanoparticles (PFFs) with different diameters of (a) 30 nm, (b) 60 nm, and (c) 100 nm. (d) HR-TEM image of FeOOH nanoneedles on the surface.

When the Cu cations were sufficiently adsorbed to the FeOOH needles, vaporized pyrrole monomers in contact with the Cu cations were polymerized *via* chemical oxidation polymerization. As a result, various diameters of U_PPy nanoparticles were fabricated having a uniform *ca*. 3 nm thick PPy-coated layer on the needle surface (Figure 35). No aggregation of coated particles was observed following polymerization; this result was attributed to the uniform dispersion of Cu cations on the FeOOH surfaces during adsorption.

X-ray diffraction (XRD) patterns of the particles are shown in Figure 36. The peak of the inorganic material in the E_PPy, PFF, and U_PPy particles could be well indexed to α-FeOOH (JCPDS 29-713), which indicated formation of α-FeOOH nanostructures on the PPy surface. The peak intensities for α-FeOOH increased as nanoneedles formed upon stirring, as expected. Broad diffraction peaks at 25.3 cm^{-1} were observed for all samples, indicating an identical crystalline PPy structure in all samples.

The chemical composition of the hybrid materials was confirmed by X-ray photoelectron spectroscopy (XPS). Figure 37a suggests the complete spectra over the range of 0–1200 eV. These overview spectra revealed that C, N, O, and Fe atoms were iluustrated in U_PPy, whereas only C, O, and N were present in the pristine PPy particles. Figure 37b displays the O 1s band of particles, deconvoluted into several components. The peaks at 531.7 and 529.6

eV were attributed to the OH^- and O^{2-} components in the FeOOH structure. The N 1s peaks for two PPy types are revealed in Figure 37c. For pristine PPy particles, three deconvoluted peaks were attributed to the N component in the pyrrole structure: 399.7 eV for neutral N, 401.2 eV for positively charged pyrrolium nitrogen, and 397.8 eV for imine-like nitrogen. The N 1s of U_PPy also contained the same three peaks, with additional chemical bonding to Fe atoms. Figure 37d presents the high-resolution XPS spectra for the Fe 2p peak of U_PPy. Spin–orbit components $2p_{3/2}$ and $2p_{1/2}$ were observed near 708.5 and 722.2 eV, indicating that the valance state of Fe was +3. Thus, we concluded that the FeOOH nanoneedles were composed of Fe(III) and O, as confirmed by the XRD results.

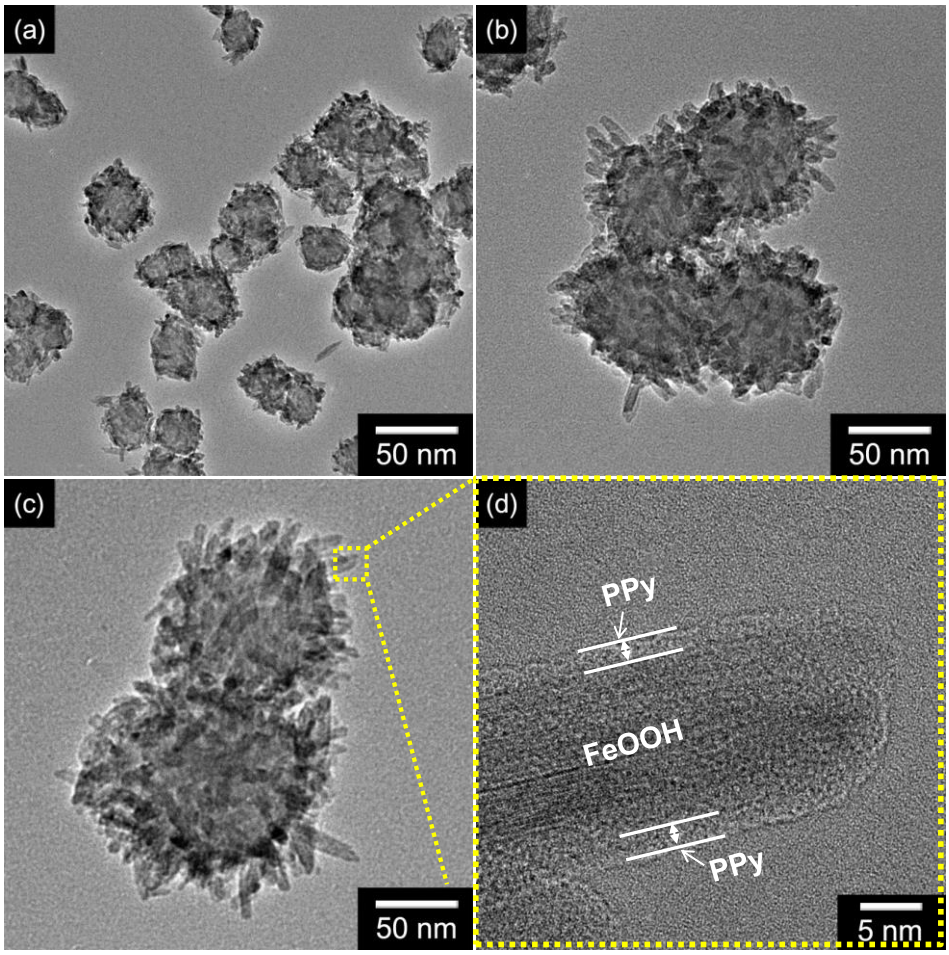

Figure 35. TEM images of U_PPy nanoparticles of (a) 30 nm, (b) 60 nm, and (c) 100 nm diameter. (d) HR-TEM images of needles on the 100 nm diameter of U_PPy nanoparticles.

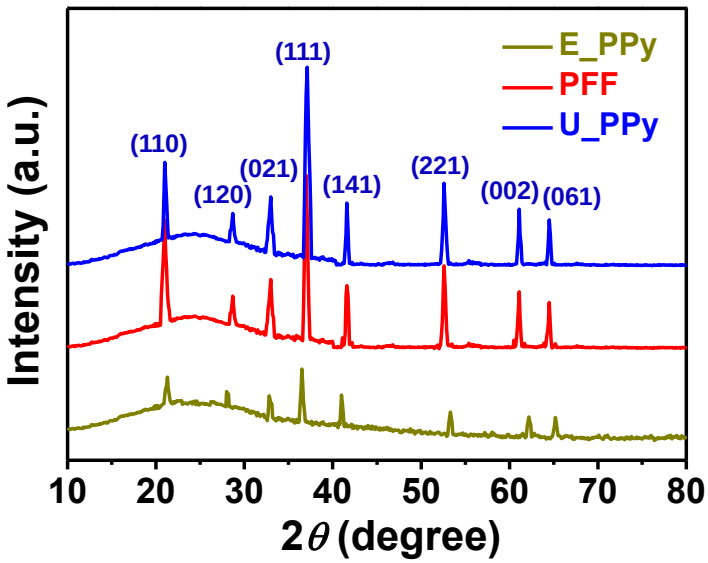

Figure 36. XRD pattern of various PPy nanoparticles (yellow: E_PPy; red: PFF blue: U_PPy).

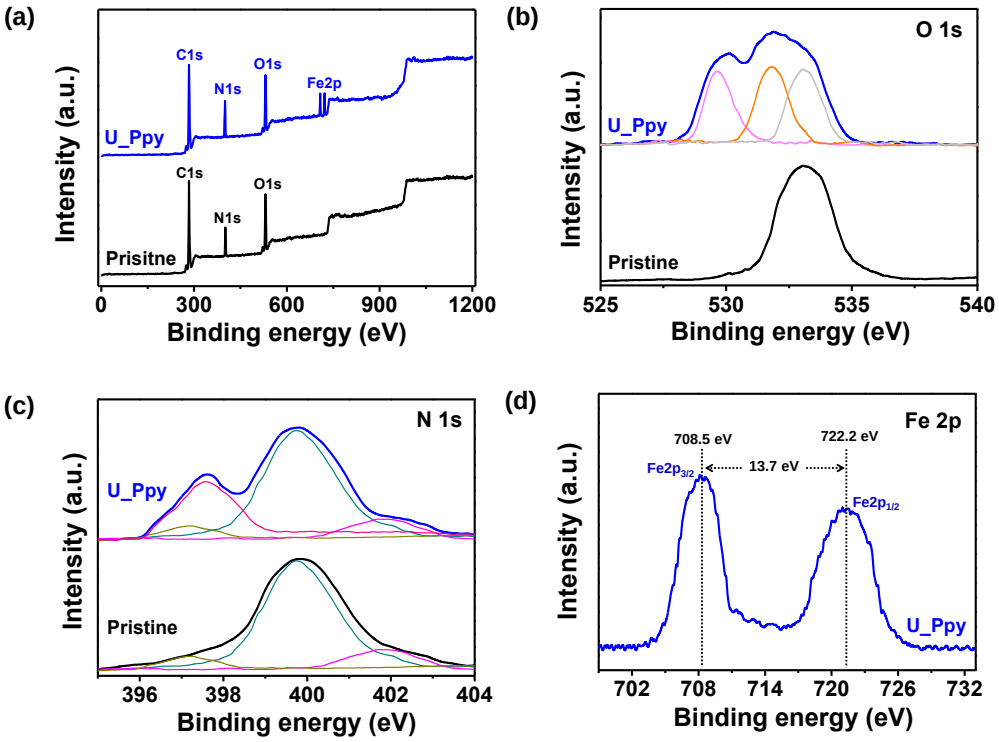

Figure 37. XPS patterns of (a) fully scanned spectra and high resolution of (b) O 1s, (c) N 1s, and (d) Fe 2p of PPy nanoparticles (black: pristine PPy; blue: U_PPy).

The specific surface area of the U_PPy particles was determined by the nitrogen adsorption/desorption isotherm, according to Brunauer-Emmett-Teller (BET) analysis (Figure 38). Starting from 100 m^2 g^{-1} of 30 nm diameter pristine PPy, the surface area increased to 396 m^2 g^{-1} for the urchin-like multidimensional particles; the specific surface areas of the 60- and 100 nm diameter PPy particles increased from 50 to 204 m^2 g^{-1} and from 35 to 140 m^2 g^{-1}, respectively, as they transformed from spheres to the urchin-like structure. Thus, a four-fold increase in surface area was observed for the U_PPy particles, compared with pristine PPy. Additionally, Figure 39 presents the current–voltage (I–V) curves of the pristine PPy and U_PPy particles; the results indicated that the PPy particles were in good electrical contact with the sensor substrate. Despite good electrical conductivity, the resistance of the U_PPy particles was lower than that of the pristine PPy particles; good electrical contact with the sensor substrate was facilitated by the greater surface area arising from the needle morphology.

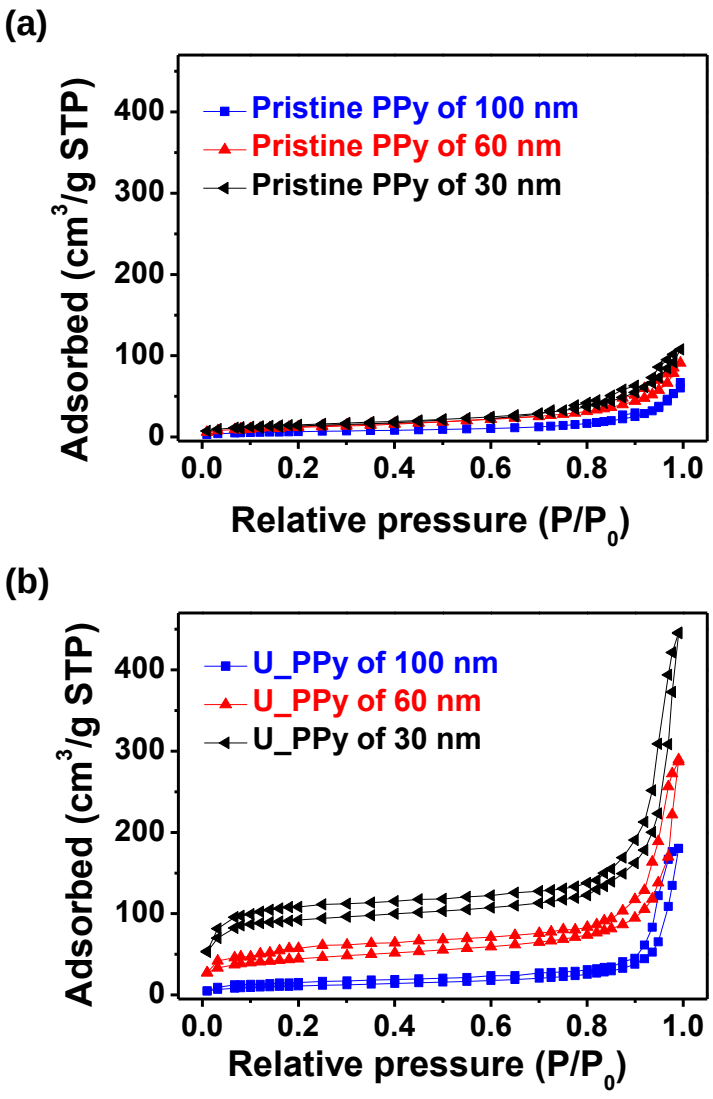

Figure 38. Nitrogen adsorption-desorption of various diameters of (a) pristine and (b) U_PPy nanoparticles (black: 30 nm; red: 60 nm; blue: 100 nm).

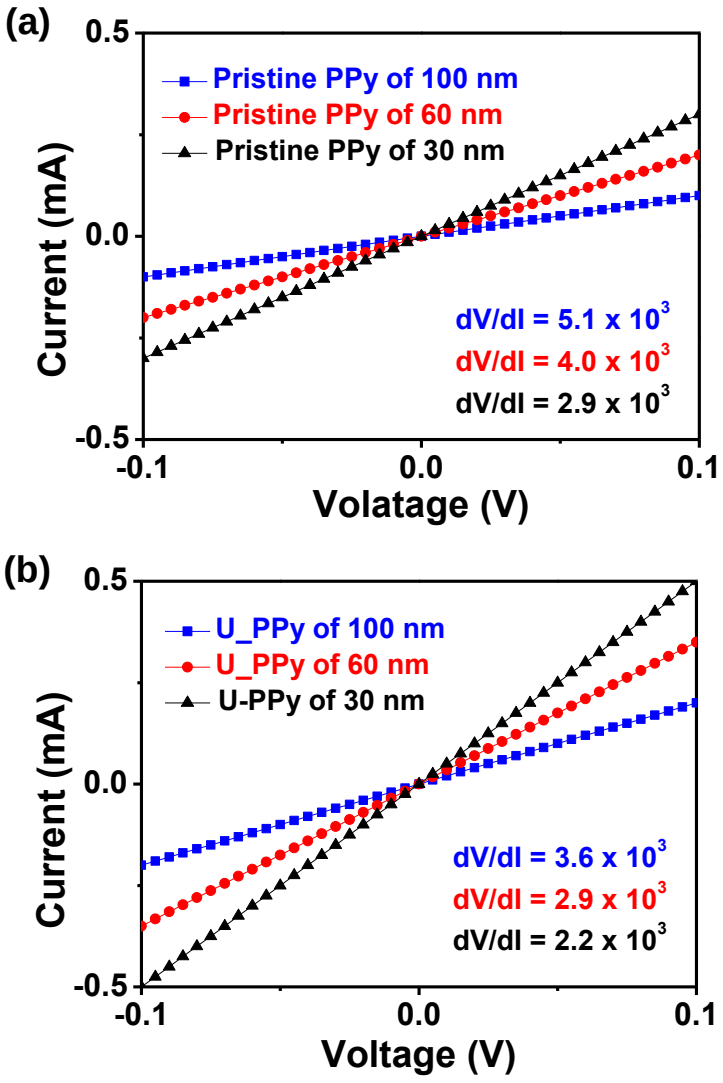

Figure 39. I-V curves of (a) pristine PPy and (b) U_PPy particles with different diameters (black: 30 nm; red: 60 nm; blue: 100 nm diameter).

3.1.2.2. Application for hazardous gas chemical sensor

To determine the sensing performance of the U_PPy nanoparticles as chemical sensor transducers, these particles were deposited onto an electrode, as suggested in Figure 40. Their electrical response, based on resistance changes, was measured in real-time upon exposure to various gases. When the U_PPy particle gas sensors were exposed to various gases at room temperature, excellent sensitivity and rapid response/recovery times were observed. Figure 41a shows the response upon sequential exposure to NH_3 (0.01, 0.05, 0.1, 1, and 10 ppm) and MeOH vapor (0.5, 1, 5, 10, and 50 ppm) as a function of analyte concentration. Interestingly, the electrical resistances of the U_PPy sensor were opposite for the two gases tested; the resistance increased after exposure to NH_3 and decreased after exposure to MeOH.[217] This result displays that the introduction of electron-donating molecules (NH_3) into the PPy backbone (p-type transducer) decreased the charge carrier (electron–hole) concentration *via* a redox reaction, resulting in the enhanced resistance of the transducer. In contrast, the electron-acceptor MeOH induced new electron–hole formation, thereby decreasing the resistance. The minimum detectable level (MDL) of the 30 nm U_PPy gas sensor was 0.01 and 0.5 ppm for NH_3 and MeOH, respectively; the MDL of both gases was within specifications provided by the Occupational Safety and Health Administration (NH_3: 25 ppm;

MeOH: 200 ppm).[218]

The enlarged surface area reduced the response times to less than 1 s for the two gases tested, with recovery times of *ca*. 30 s (for 0.1 ppm of NH_3) and *ca*. 15 s (for 5 ppm of MeOH) for the 30 nm diameter U_PPy particles (Figure 42). The enhanced surface area of the U_PPy particles allowed rapid diffusion of the analyte gas molecules for fast detection and rapid response times, as well as enhanced sensitivity with decreasing diameter (100 nm < 60 nm < 30 nm), because smaller diameters provided higher surface-to-volume ratios and, thus, increased the interaction with the target analyte (Table 2).

Figure 41b demonstrates the electrical response of various U_PPy particles upon periodic exposure to 0.1 ppm of NH_3 and 5 ppm of MeOH at room temperature. The U_PPy particles exhibited similar responses for both NH_3 and MeOH. Moreover, this gas sensor maintained its sensing ability after 100 cycles (Figure 41c). Figure 41d shows the sensitivity (defined as the normalized resistance change measured after a 10 s vapor exposure) of the sensor as a function of NH_3 gas and MeOH vapor concentrations. At low concentrations (<0.01 ppm), the normalized resistance change was nearly zero at 0 ppm; the U_PPy particles described a nonlinear change in sensitivity. In contrast, linear behavior was observed for sensor sensitivity over the concentration ranges of 0.01–10 ppm for NH_3 and 0.5–50 ppm for MeOH.

Therefore, U_PPy particles can be effectively utilized as signal transducers for detecting NH_3 gas and MeOH vapor of various concentrations. In addition, Figure 43 demonstrates the sensitivity of 30 nm diameter pristine PPy and U_PPy particles to various organic vapors at 10 ppm. In pristine PPy, a significant signal change was only observed for NH_3 gas at 10 ppm. On the other hand, U_PPy nanoparticles exhibited significant signal changes in the presence of all of the organic vapors evaluated except for hexane. Among all gases tested, the sensitivity and selectivity were greatest for NH_3; furthermore, the MDL of NH_3 was 10–10^3 times higher than that of other gases. The MDL of 30 nm diameter pristine PPy and U_PPy nanoparticles for each vapor is illustrated in Table 3.

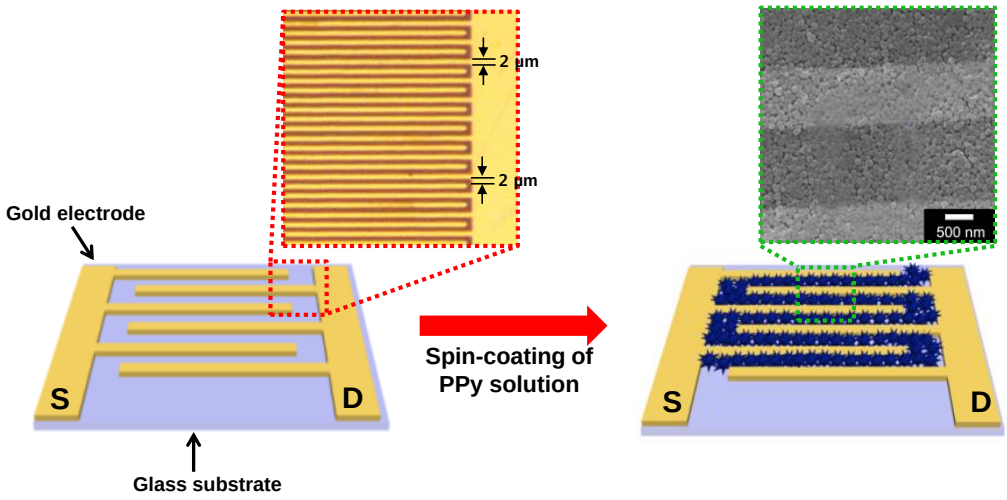

Figure 40. Schematic illustration of inter-digitated array electrode and U_PPy nanoparticle deposited electrode by spin-coating method (red inset: optical micrograph image of electrode; green inset: FE-SEM image of U_PPy deposited electrode).

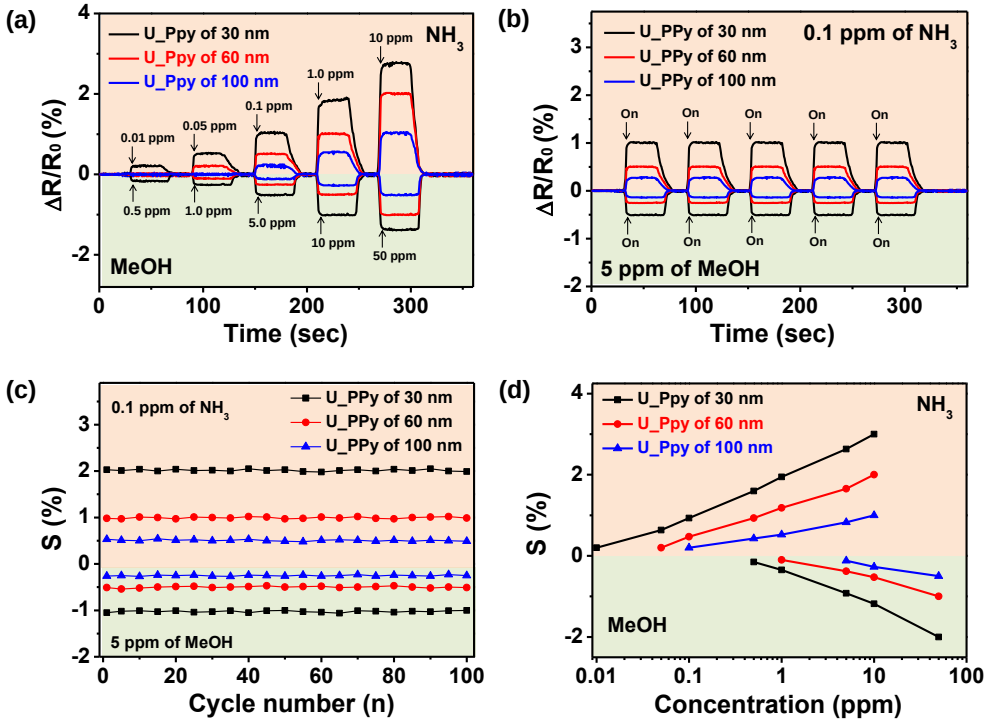

Figure 41. Reversible and reproducible responses are measured at a constant current value (10^{-6} A) with diameter of U_PPy nanoparticles. Normalized resistance changes upon sequential exposure to (a) various concentrations of NH_3 and MeOH and (b) periodic exposure to 0.1 ppm of NH_3 and 5 ppm of MeOH. (c) Sensitivity changes of U_PPy particles with periodic exposure to 0.1 ppm of NH_3 gas and 5 ppm of MeOH vapor for 100 times (black: 30 nm; red: 60 nm; blue: 100 nm diameter). (d) Calibration line of U_PPy nanoparticles as a function of NH_3 and MeOH concentration (black: 30 nm; red: 60 nm; blue: 100 nm).

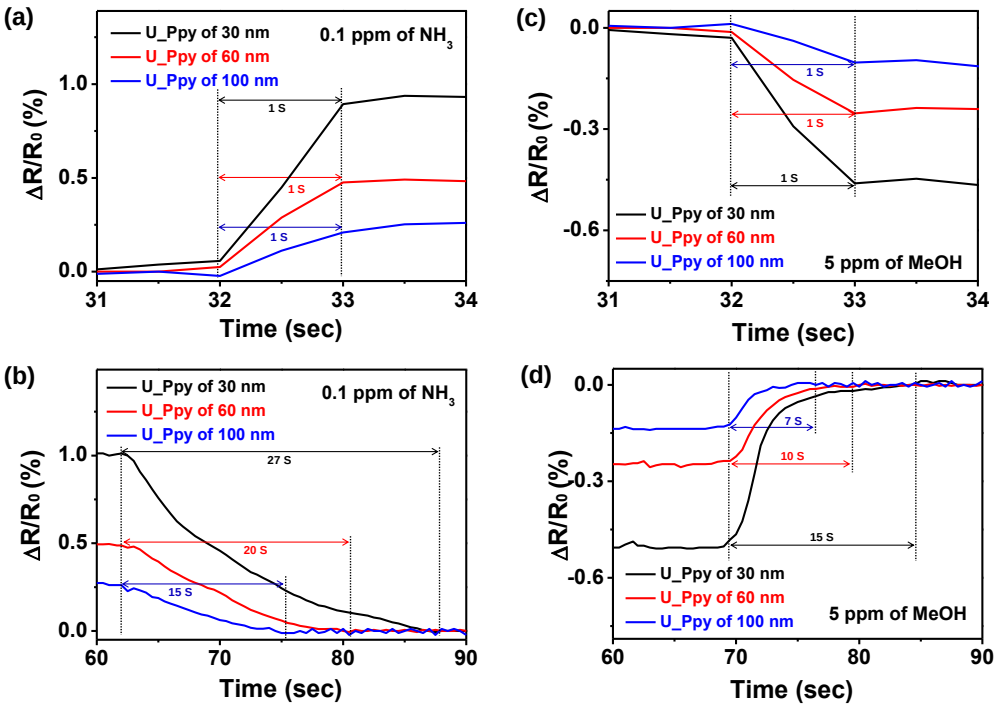

Figure 42. The response and recovery times of U_PPy particles with different diameters toward (a), (b) 0.1 ppm of NH_3 gas and (c), (d) 5 ppm of MeOH vapor (black: 30 nm; red: 60 nm; blue: 100 nm diameter).

Table 2. BET surface area and sensing ability of various hybrid polypyrrole nanoparticles to two types of hazardous molecule.

	BET area[a] (m^2 g^{-1})	MDL[b] (NH_3/MeOH)	reference
PPy of 30 nm	100	5 ppm / 50 ppm	[217]
PPy of 60 nm	50	5 ppm / 50 ppm	[217]
PPy of 100 nm	35	5 ppm / 50 ppm	[217]
U_PPy of 30 nm	396	0.01 ppm / 0.5 ppm	this work
U_PPy of 60 nm	204	0.05 ppm / 1.0 ppm	this work
U_PPy of 100 nm	140	0.1 ppm / 5 ppm	this work

[a] Surface area calculated from Brunauer-Emmett-Teller method

[b] Minumum detactable level

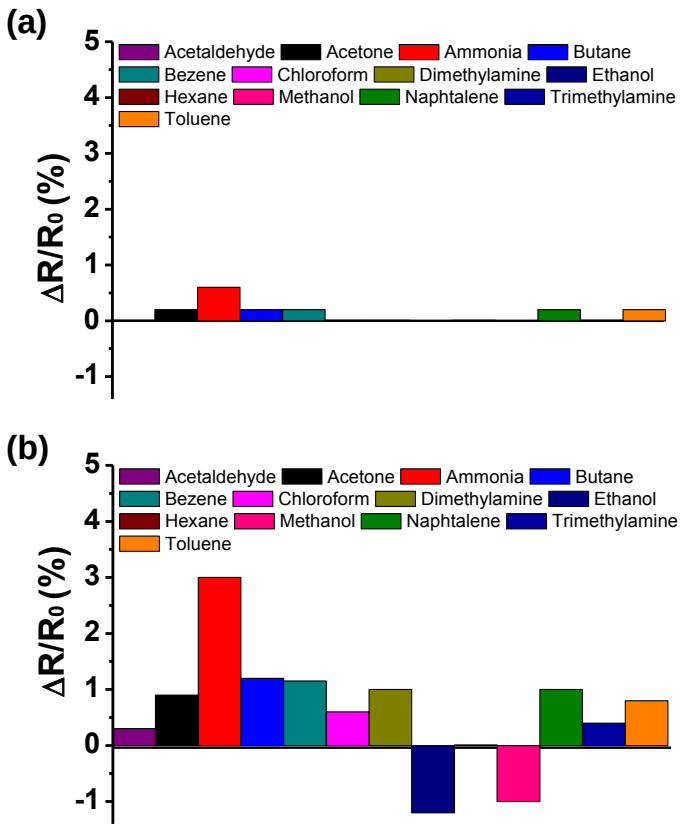

Figure 43. Sensing performance histogram of 30 nm-diameter (a) pristine PPy particles and (b) U_PPy particles to 13 analytes: each analyte concentration was fixed at around 10 ppm.

Table 3. Minimum detectable level (MDL) of 30-nm-diameter pristine PPy and U_PPy nanoparticles to various hazardous vapors.

	pristine PPy	U_PPy
Acetaldehyde	100 ppm	10 ppm
Acetone	10 ppm	2 ppm
Ammonia	5 ppm	0.01 ppm
Butane	10 ppm	1 ppm
Benzene	10 ppm	1 ppm
Chloroform	30 ppm	2 ppm
Dimethylamine	30 ppm	1 ppm
Ethanol	40 ppm	0.2 ppm
Hexane	150 ppm	30 ppm
Methanol	50 ppm	0.5 ppm
Naphtalene	10 ppm	1 ppm
Trimethylamine	100 ppm	5 ppm
Toluene	10 ppm	1 ppm

3.1.3. Aptamer-functionalized multidimensional carboxylated polypyrrole hybrid nanoparticles

3.1.3.1. Fabrication of aptamer-functionalized multidimensional carboxylated polypyrrole hybrid nanoparticles

Multidimensional carboxylated polypyrrole nanoparticles (M_CPPyNPs) were fabricated using dual-nozzle electrospray and vapor deposition polymerization (VDP). As a starting material, carboxylated polypyrrole nanoparticles (CPPyNPs) (diameter: 30, 60, and 100 nm) were synthesized through chemical copolymerization of pyrrole and pyrrole-3-carboxylic acid (molar ratio = 30 (pyrrole) : 1 (pyrrole-3-carboxylic acid)) using the dispersion method. The pyrrole-3-carboxylic acid functional units were incorporated into the pyrrole repeating units through α-α' covalent linkages without any degradation in their major physical properties.

The carboxylated polypyrrole nanoparticles (CPPyNPs) were then mixed with an $FeCl_3$ aqueous solution; the mixture was electrosprayed using a dual-nozzle consisting of the CPPyNP mixed solution (outer part) and compressed air (inner part) into an NaOH aqueous solution contained within a Petri dish. The electrosprayed CPPyNPs were then mixed with the $FeCl_3$ aqueous solution at 70℃ for 4 h to induce growth of FeOOH needles on the surface.

The FeOOH-decorated hybrid CPPyNPs were then dipped into 5 wt%

$CuCl_2$ ethanol solution. As a result, Cu cations adsorbed to the FeOOH needle surface, due to the charge–charge interaction between the Cu^{2+} ions and the partial negative charge of the oxygen atoms in the FeOOH structure (Figure 44). When the Cu cations were sufficiently adsorbed to the FeOOH needles, vaporized pyrrole/pyrrole-3-carboxylic acid monomers (molar ratio: 30/1), in contact with the Cu cations, were copolymerized *via* chemical oxidation polymerization. As a result, a uniform CPPy layer (thickness: *ca*. 3 nm) formed on the surface, as confirmed by transmission electron microscopy (TEM) and high-resolution TEM (Figure 45a and b, respectively). Electron energy loss spectroscopy (EELS) mapping of Fe, O, and N atoms confirmed the composition of the CPPy-coated FeOOH needle surface through the VDP step (Figure 45c–e). The 30- and 100-nm-type CPPyNPs also formed a similar multidimensional morphology using the same process, as described in the Figure 46. No aggregation of the coating particles was observed following polymerization, owing to the uniform dispersion of Cu cations on the FeOOH surfaces during adsorption. The surface area of the prepared M_CPPyNPs increased *ca*. four-fold, compared with pristine CPPyNPs; specifically the surface area increased from 100 to 396 $m^2 g^{-1}$ for the 30-nm-type, 50 to 204 $m^2 g^{-1}$ for the 60-nm-type, and 35 to 140 $m^2 g^{-1}$ for the 100-nm-type M_CPPyNPs (Figure 47).

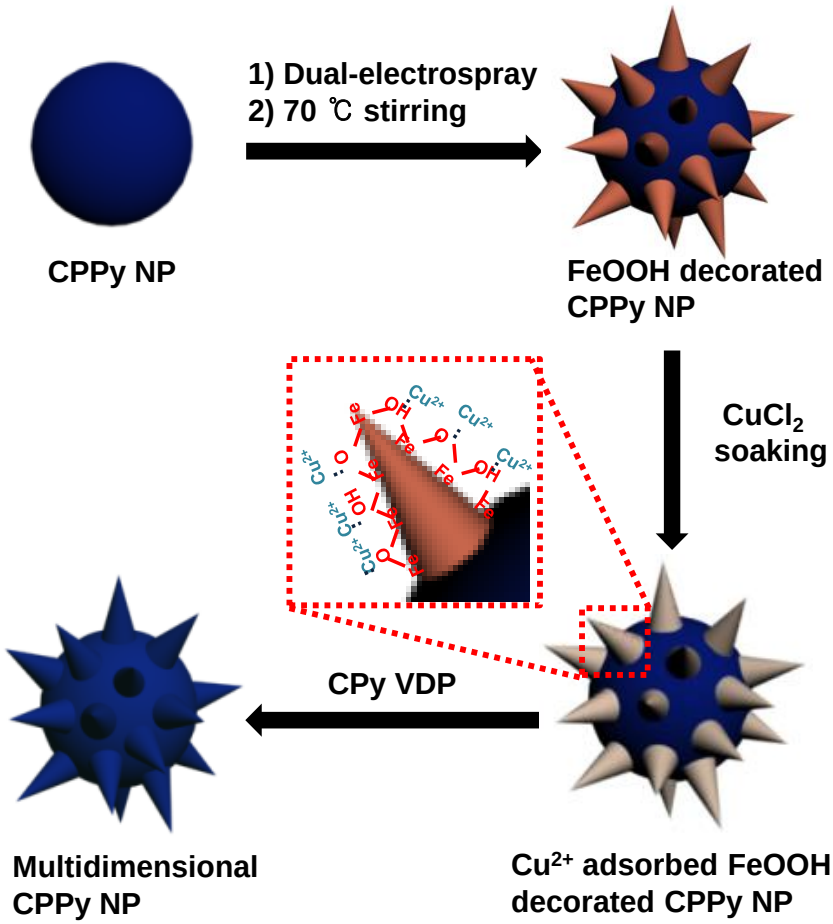

Figure 44. Illustrative diagram of the sequential fabrication steps for multidimensional carboxylated polypyrrole (CPPy) nanoparticles (M_CPPyNPs) (red inset: mechanism of Cu^{2+} adsorption on the FeOOH surface).

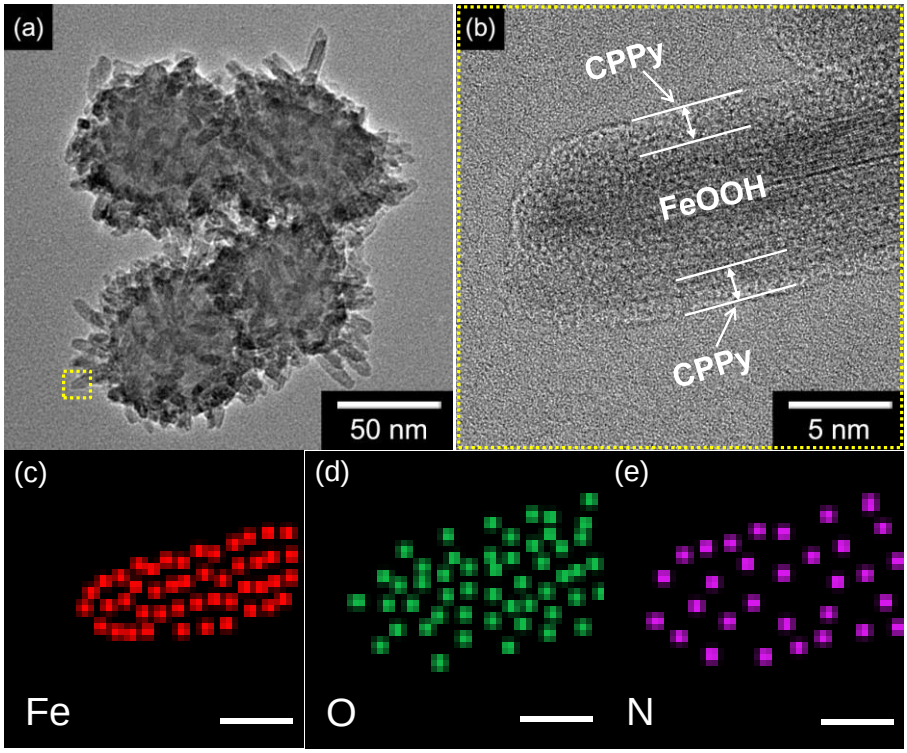

Figure 45. (a) Transmission electron microscopy (TEM) image of multidimensional carboxylated polypyrrole nanoparticles (M_CPPyNPs) 60 nm in diameter. (b) High-resolution TEM (HR-TEM) image of a nanoneedle on M_CPPyNP. Electron energy loss spectroscopy (EELS) dot mapping of the needle on the M_CPPy surfaces, composed of (c) Fe (red), (d) O (green), and (e) N (purple) atoms.

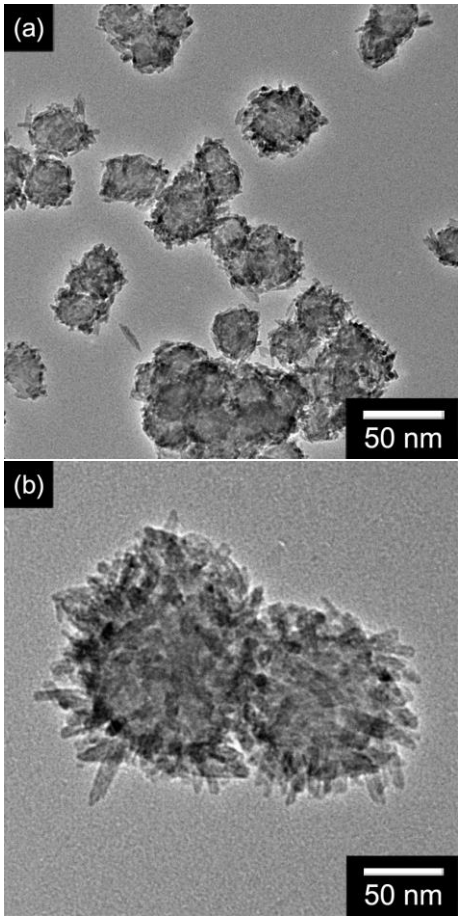

Figure 46. Transmission electron microscopy (TEM) images of M_CPPyNPs: (a) 30-nm-diameter and (b) 100-nm-diameter nanoparticles.

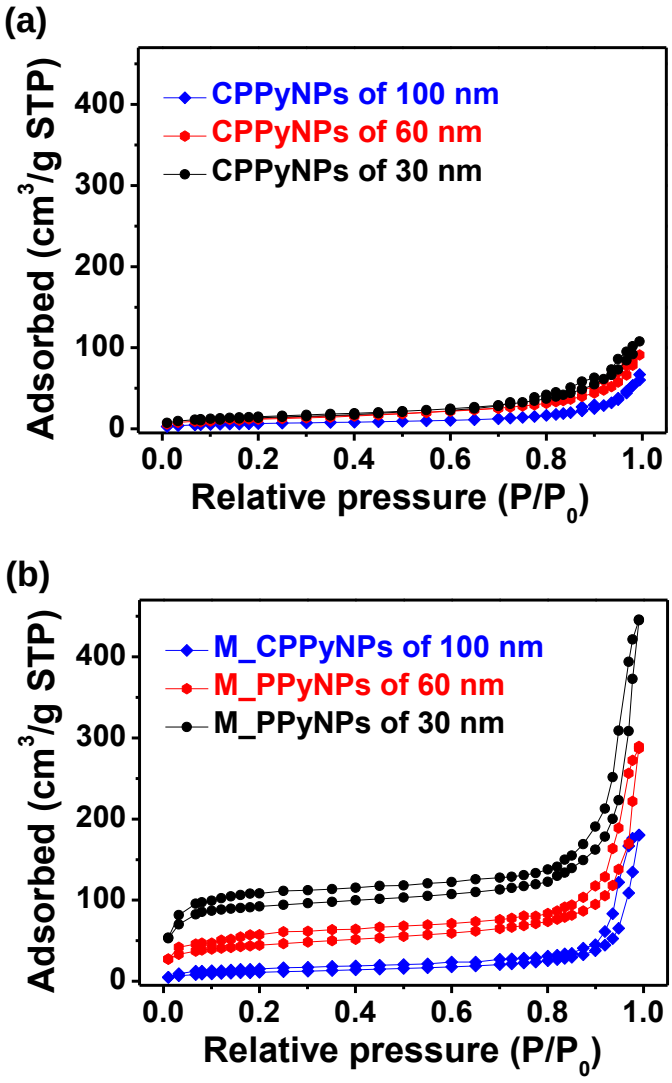

Figure 47. Nitrogen adsorption–desorption for (a) pristine and (b) M_CPPyNPs for various diameter nanoparticles (black: 30 nm; red: 60 nm; blue: 100 nm).

The stability of the sensing environment (*i.e.*, the liquid–ion solution) and strong bonding between the transducer and binding receptors are critical factors in the fabrication of highly sensitive FET-type biosensor electrodes. To improve stability, immobilization of the transducer on the sensor electrode and binding receptor on the transducer were conducted *via* covalent bonding of functional groups. Figure 48 provides a schematic diagram of the procedure for the immobilization of aptamer-functionalized M_CPPyNPs on the electrode substrate. An interdigitated microelectrode array (IDA) was patterned on a glass substrate using a lithographic process; the array was composed of pairs of gold electrode bands with 25 lines of fingers (Figure 49). The IDA glass substrate was treated using 3-aminopropyltrimethoxysilane (APS) to amine (-NH_2) functionalized on the surface. Subsequently, the M_CPPyNPs were anchored to the substrate through a condensation reaction between the carboxylic group (-COOH) of the nanoparticles and the amine group (-NH_2) of the substrate through condensing agent (4-(4,6-dimethoxy-1,3,5-triazin-2-yl)-4-methylmorpholinium chloride (DMT-MM)). The carboxyl group of M_CPPyNPs facilitated compact nanoparticle-array formation on the substrate, as well as enabled the attachment of binding aptamers to the particle surface. The 3'-end of the BPA-binding aptamer (5'-NH_2-CCG GTG GGT GGT CAG GTG GGA TAG CGT TCC GCG TAT GGC CCA GCG CAT CAC GGG

TTC GCA CCA-3') was modified with a primary aliphatic amino linker for the covalent bonding between the BPA-binding aptamer and the carboxyl group of the M_CPPyNPs. A similar condensation reaction occurred between the amine group of the binding aptamer and the carboxylic group of the M_CPPyNPs. As a result, BPA-binding aptamer-functionalized M_CPPyNPs (A_M_CPPyNPs) became immobilized on the electrode substrate, and demonstrated outstanding stability against environmental perturbation.

Figure 50a shows field-effect scanning electron microscopy (FE-SEM) images of the as-prepared 60-nm-diameter immobilized A_M_CPPyNPs, with highly ordered packing on the IDA substrate. The arrays of ordered, packed hybrid nanoparticles were clearly observed between the IDA. TEM images of the A_M_CPPyNPs indicated a rugged surface morphology and enlarged-sized NPs, compared with M_CPPyNPs (*i.e.*, evidence of aptamer conjugation) (Figure 50b). Additionally, the 30- and 100-nm-diameter hybrid NPs were also packed on the IDA electrode in ordered array form, and described a rugged surface morphology, similar to the 60-nm-type A_M_CPPyNPs (Figure 51).

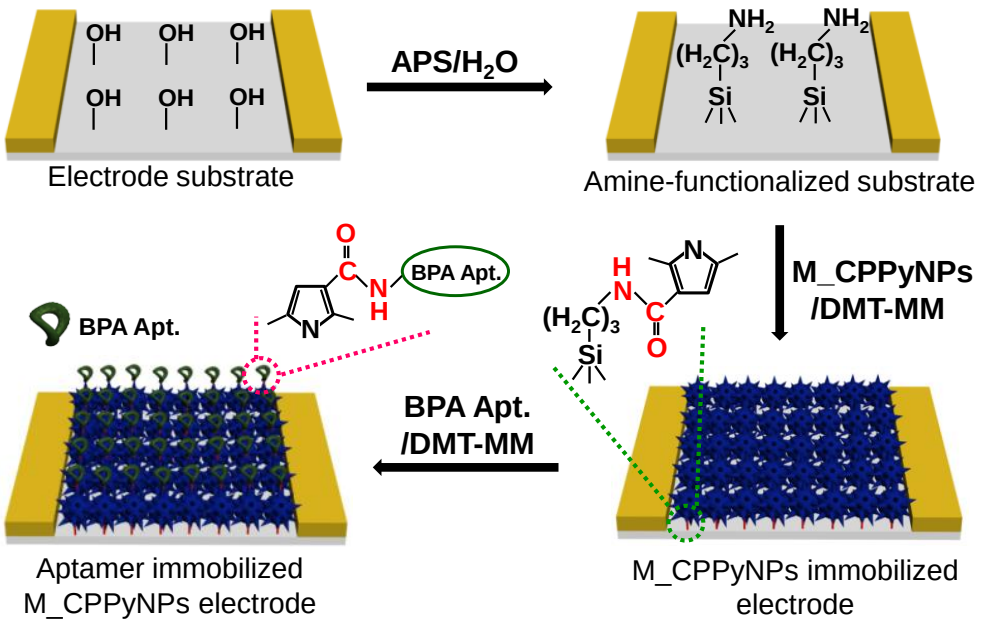

Figure 48. Schematic diagram of the immobilization process used to produce the aptamer-functionalized M_CPPyNP (A_M_CPPyNP) sensor electrode on the interdigitated array (IDA) electrode substrate.

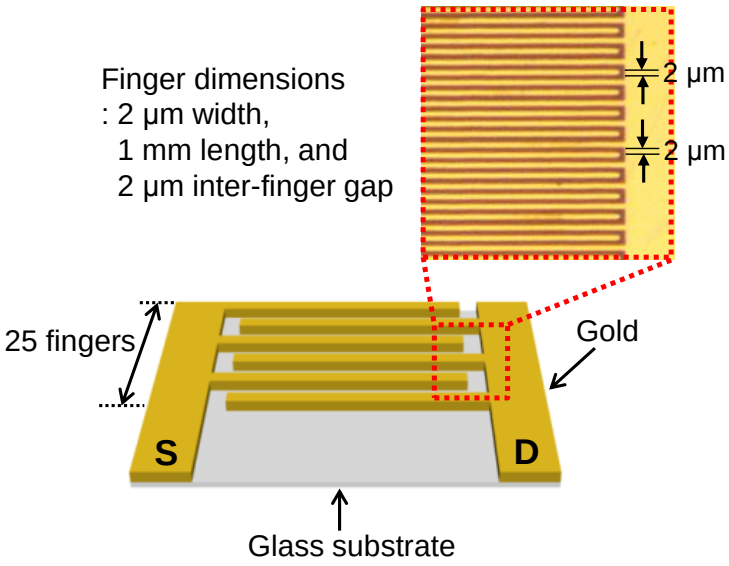

Figure 49. Schematic diagram of the interdigitated array (IDA) electrode (red inset: optical microscope image of the gold finger).

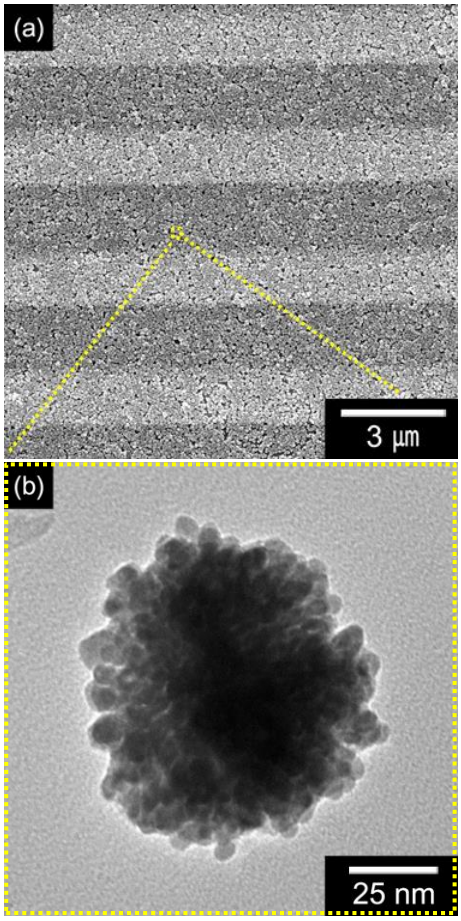

Figure 50. (a) Field-effect scanning electron microscopy (FE-SEM) image of immobilized arrays of the bisphenol A (BPA)-binding apatamer conjugated-M_CPPyNPs (A_M_CPPyNPs) on the IDA substrate. (b) TEM image of the A_ M_CPPyNP with 60-nm-type.

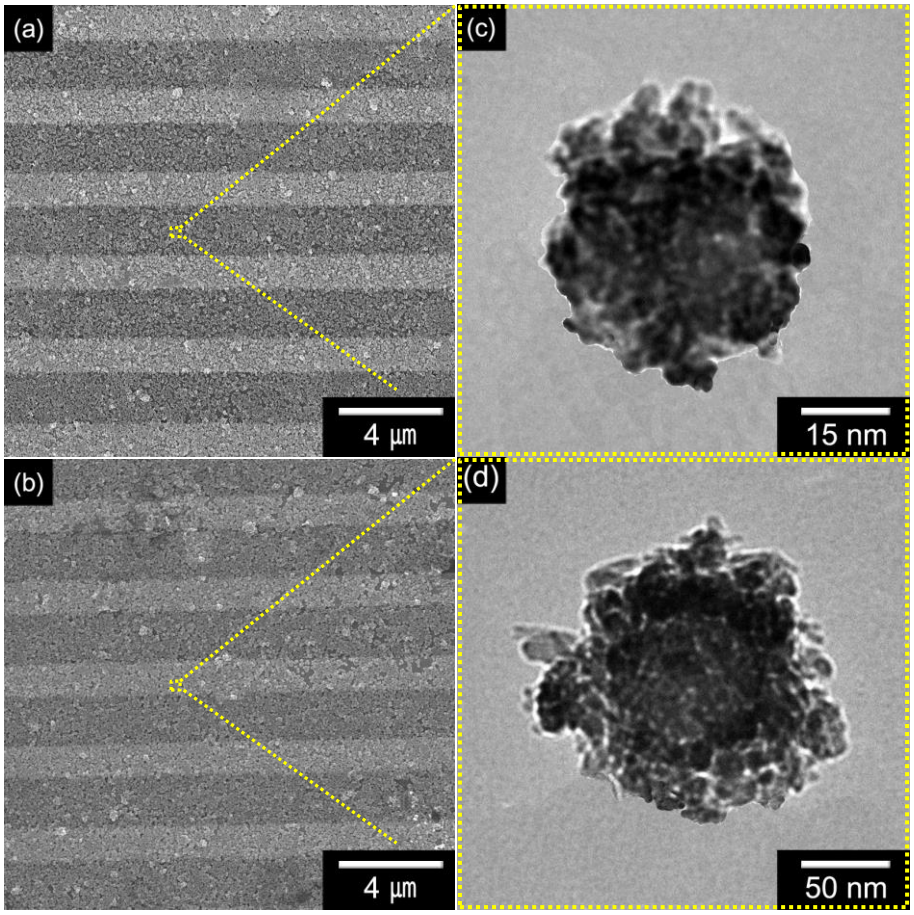

Figure 51. FE-SEM images of a (a) 30-nm-type and (b) 100-nm-type A_M_CPPyNPs immobilized on the IDA substrate. TEM images of a (c) 30-nm-type and (d) 100-nm-type BPA-binding aptamer-immobilized A_M_CPPyNP.

Current-voltage (I–V) curves were used to evaluate the electrical contact of A_M_CPPyNPs on the IDA substrate. Figure 52a suggests the I–V characteristics of 30-, 60-, and 100-nm-diameter M_CPPyNPs, before and after immobilization of the BPA-binding aptamer. M_CPPyNPs with no aptamer conjugation exhibited linearity (*i.e.*, ohmic contact) for voltages ranging from −0.1 to 0.1 V, as opposed to the nonlinearity illustrated by Schottky barriers with poor electrical contact at the electrode. The dI/dV values of the electrode increased, as the diameter of the M_CPPyNPs decreased, and decreased after the binding aptamer became immobilized on the particle surface. During aptamer introduction, oxidation level of M_CPPyNP was changed owing to detachment of doped element through condensation reaction. Nevertheless, linearity was maintained, and the dI/dV value was preserved with the same order of magnitude, after binding-aptamer immobilization. Thus, these results display that the binding aptamers were effectively incorporated into the M_CPPyNPs, without any deterioration in electrical contact. Additionally, compared with pristine CPPyNPs, the electrical properties of the M_CPPyNPs demonstrated higher conductivity, due to the enhanced contact area with the electrode substrate, by the presence of CPPy nanoneedles on the particle surface (Figure 52b).

To characterize the electrical properties of A_M_CPPyNPs in the liquid

phase, an FET configuration was constructed using an electrolyte as a liquid-ion gate. Figure 53a presents a schematic diagram of the FET-sensor platform, based on A_M_CPPyNPs. Two gold IDA bands were used as the source (S) and drain (D) electrodes. The gate electrode was immersed in the electrolyte. The gate potential (V_G) was applied to the source electrode through a buffer solution. The distance between the electrodes was fixed at 2 mm, based on the resistivity of the buffer solution. To characterize the charge transport properties of A_M_CPPyNPs in the FET configuration, the dependence of the source–drain current (I_{SD}) with V_G variation (−20 to 100 mV) was investigated at a constant scan rate (10 mV s^{-1}) of source–drain voltage (V_{SD}). Figure 53b shows a plot of the I_{SD} versus V_{SD} for varying V_G, for a 30-nm-diameter A_M_CPPyNP electrode. The I_{SD} increased negatively with negative enhancing V_G, indicating p-type (hole-transport) behavior, caused by an increase in the oxidation level of the polymer chains. Additionally, other sizes of A_M_CPPyNPs (60- and 100-nm-diameter) electrodes also exhibited p-type behavior (Figure 54). Consequently, the dependence of I_{SD} on V_G confirmed that A_M_CPPyNP FETs could be effectively used as an electrochemical sensor for detecting analytes in solution. The liquid-ion gate is capable of achieving increased transconductance, because of the intimate contact between the nanoparticles and the gate, compared with conventional backgating.

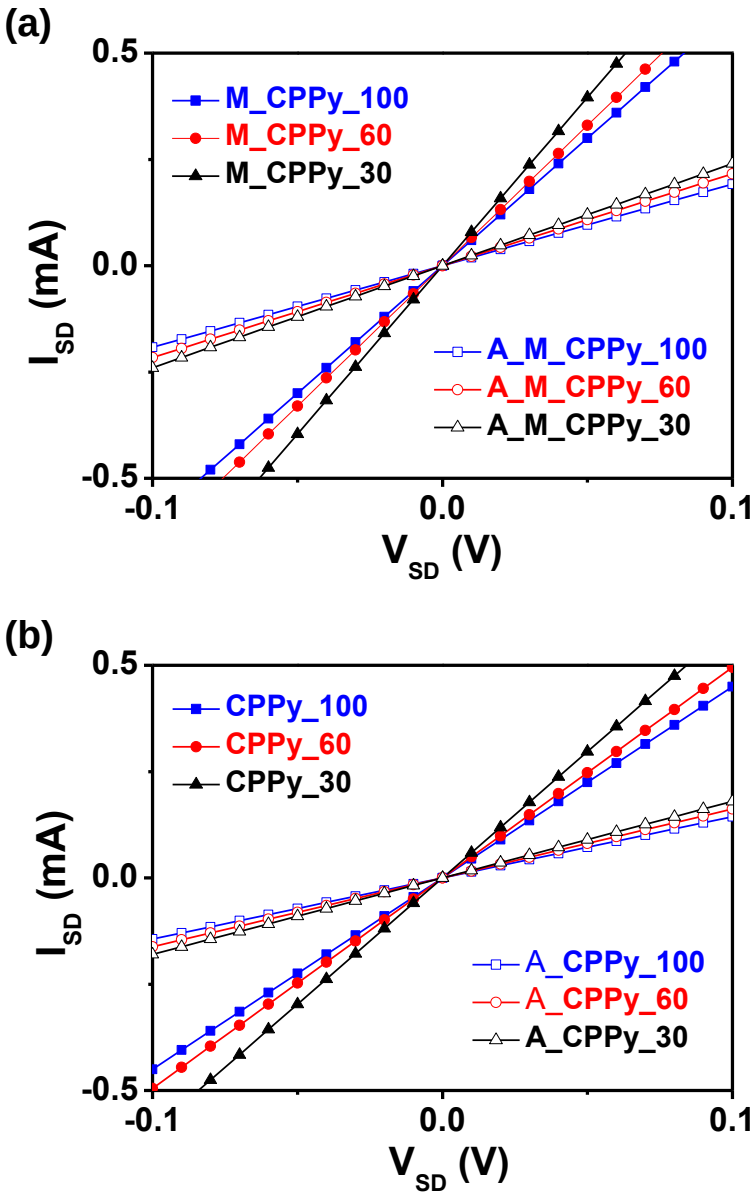

Figure 52. Current–voltage (I_{SD}–V_{SD}) curve comparison of 30-, 60-, and 100-nm-diameter nanoparticles: (a) M_CPPyNP- and (b) CPPyNP-based IDA electrodes, before and after BPA-binding aptamer introduction (for a V_{SD} scan rate of 10 mV s^{-1}).

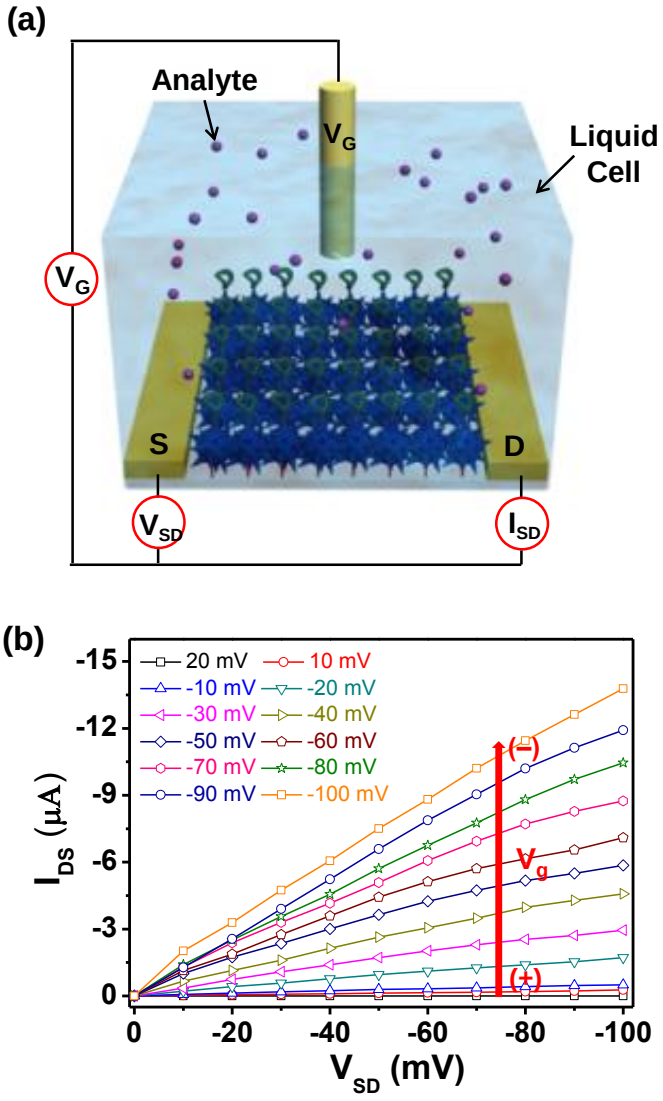

Figure 53. (a) Schematic diagram of liquid-ion-gated field-effect transistor (FET)-type A_M_CPPyNP arrays. (b) Source–drain current (I_{SD}) versus source–drain voltage (V_{SD}) (I_{SD}–V_{SD}) characteristics of an A_M_CPPyNP FET-type electrode (NP diameter: 30 nm) for a varying gate voltage (V_G) ranging from 20 to −100 mV in −10 mV steps (V_{SD} scan rate: 10 mV s^{-1}).

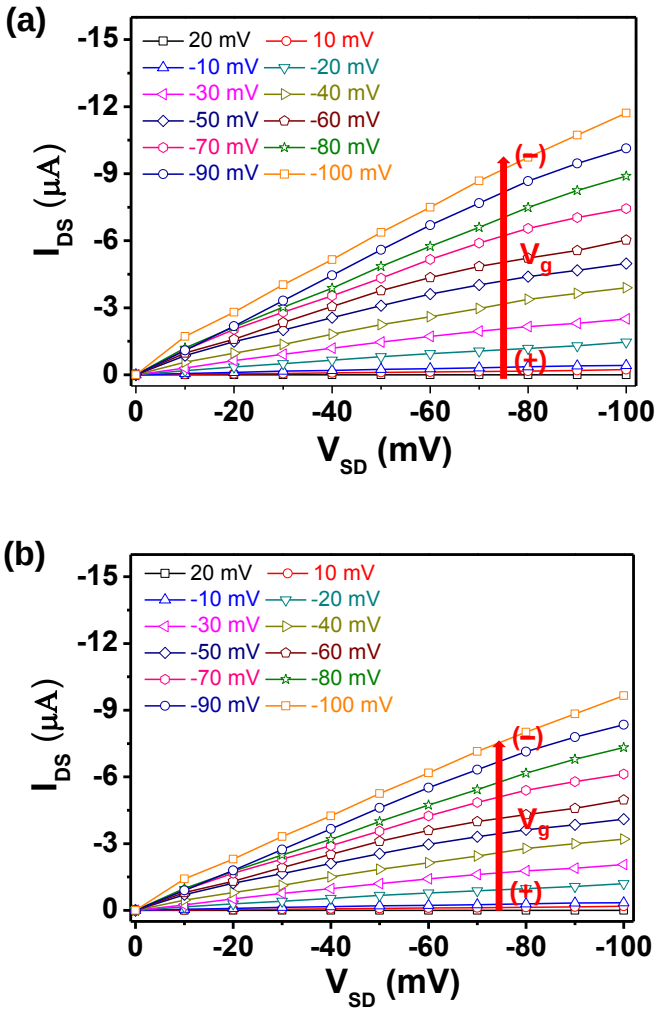

Figure 54. Current–voltage of source–drain (I_{SD}–V_{SD}) characteristics of a (a) 60-nm-type and (b) 100-nm-type A_M_CPPyNP FET-type electrode for a gate voltage (V_G) range of 20 to −100 mV in −10 mV steps (V_{SD} scan rate: 10 mV s^{-1}).

3.1.3.2. Application for endocrine disruptor biosensor

To investigate the sensing characteristics of the liquid-ion-gated A_M_CPPyNP FET, I_{SD} was monitored in real time at a V_G = 10 mV (V_{SD} = 10 mV), a low operating voltage, upon the addition of various concentrations of bisphenol A (BPA). Figure 55a shows the real-time response of the A_M_CPPyNP FET sensor for 30-, 60-, and 100-nm-diameter particles as a function of BPA concentration. Upon each addition of BPA, the I_{SD} decreased rapidly over a 1-s period before reaching its saturated value. The decrease in I_{SD} may account for the intermolecular interaction that is induced in the formation of the binding aptamer–BPA complex. The carboxyl functional group in the polymer chains has a large dipole moment (μ = 2.6 D), and the BPA binding aptamer has an overall negative charge.[158,219] Therefore, the BPA bonded to A_M_CPPyNPs can induce dipole–dipole or dipole–charge interactions between BPA and aptamer-conjugated polymer chains. Particularly, the negative charge of the binding aptamers can be reduced by BPA molecules, when the BPA molecule–aptamer complex forms. This intermolecular interaction reduces the hopping rate of charge carriers because 1) the Coulomb interaction between the positively charged polymer chains and counter ions becomes enhanced, and 2) a conformational change in the polymer chains is induced, from a linear form to a coil formation. The sensitivity of

A_M_CPPyNP FETs increased as the diameter of the nanoparticles used decreased; specifically, the 30-nm-type A_M_CPPyNP was capable of detecting BPA concentrations as low as 1 fM at room temperature. The smaller diameter nanoparticle has a higher density of chemical functionality (degree of carboxylic acid group and aptamer introduced), compared with nanoparticles of a larger diameter. Therefore, a better sensitivity was achieved with 30-nm as a result of the enhanced aptamer–BPA molecule interaction.

Figure 55b displays the changes in sensitivity as a function of nanoparticle diameter for the A_M_CPPyNPs, with respect to BPA concentration. The sensitivity (S) was determined from the normalized current change ($(\Delta I/I_0)_{SD} \times 100$) saturation point, measured after a 10 s of the BPA addition. At low concentrations ($< 10^0$ fM), the A_M_CPPy FET sensors showed nonlinear changes in sensitivity. In contrast, linear behavior was observed over a wide concentration range (10^0–10^4 fM). Compared with BPA sensors based on CPPyNPs, the M_CPPyNPs presented 10^2-fold higher sensitivity (Figure 56). Importantly, the sensitivity of the 30-nm-diameter A_M_CPPyNP electrode was higher than that of the others, due to the enhanced active functional site on its surface (Table 4).

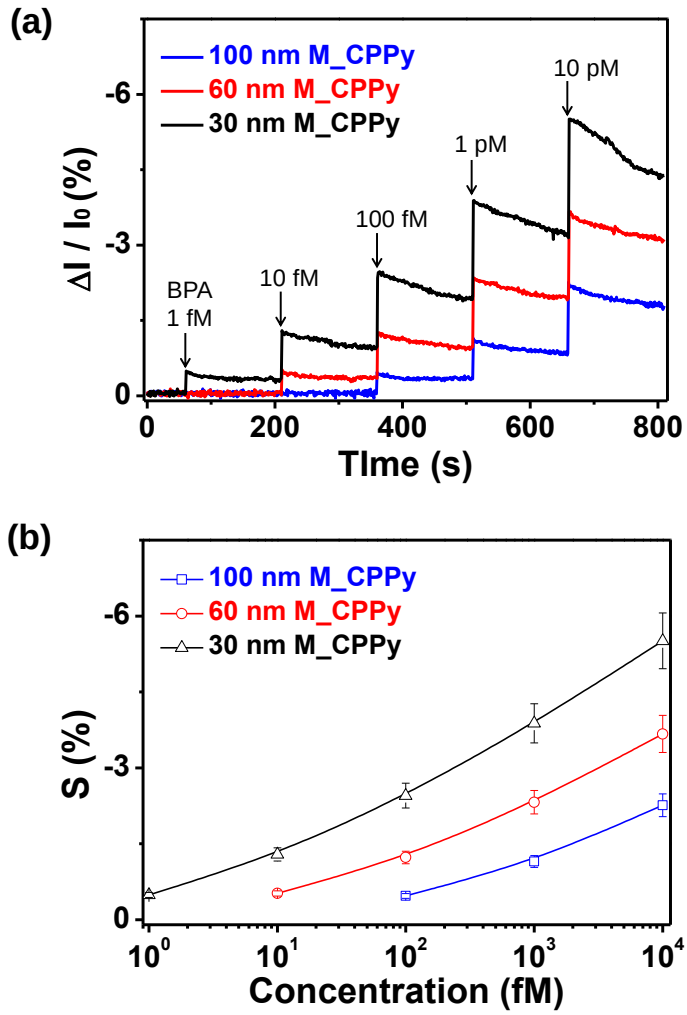

Figure 55. (a) Real-time response for various diameter of A_M_CPPyNP FETs, with normalized current changes ($\Delta I/I_0 = (I - I_0)/I_0$, where I_0 is the initial current and I is the instantaneous current), and (b) calibration curves of various diameter of A_M_CPPyNP FETs as a function of BPA concentration (S indicates the normalized current change after a 10 s BPA exposure) (black: 30-nm-type M_CPPyNP; red: 60-nm-type M_CPPyNP; blue: 100-nm-type M_CPPyNP) (V_G = 10 mV, V_{SD} = 10 mV).

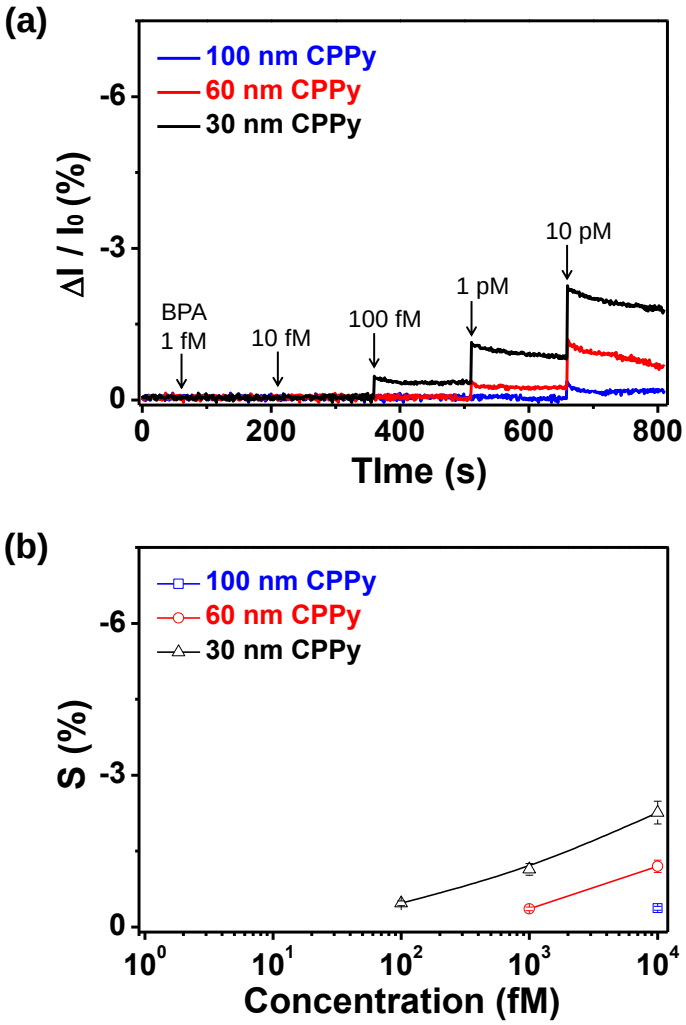

Figure 56. (a) Real-time response of different diameter of aptamer-functionalized CPPyNP FETs with normalized current changes ($\Delta I/I_0 = (I-I_0)/I_0$, where I_0 is the initial current and I is the instantaneous current), and (b) calibration curves of various diameter aptamer-functionalized CPPyNP FETs as a function of BPA concentration (S indicates the normalized current change) (black: 30-nm CPPyNP; red: 60-nm CPPyNP; blue: 100-nm CPPyNP) (V_G = 10 mV, V_{SD} = 10 mV).

Table 4. BET surface area and sensing ability of various diameter of binding aptamer-functionalized carboxylated polypyrrole nanoparticles to bisphenol A.

	BET area[a] (m^2 g^{-1})	MDL[b]
CPPyNP of 30 nm	100	100 fM[c]
CPPyNP of 60 nm	50	1 pM[d]
CPPyNP of 100 nm	35	10 pM
M_CPPyNP of 30 nm	396	1 fM
M_CPPyNP of 60 nm	204	10 fM
M_CPPyNP of 100 nm	140	100 fM

[a] Surface area calculated from Brunauer-Emmett-Teller method

[b] Minumum detactable level

[c] 10^{-15} M

[d] 10^{-12} M

The selectivity of the A_M_CPPyNP FET towards the BPA molecule was investigated for several bisphenol molecules: bisphenol B (BPB), 4,4'-bisphenol (BP), 4,4-bis(4-hydroxyphenyl) valeric acid (VA), and 4,4-(hexafluoroisopropylidene) diphenol (6F) (Figure 57). The A_M_CPPyNP sensor illustrated no significant I_{SD} changes with the addition of each 10 μM of non-target molecules; however, considerable I_{SD} changes were evident upon the addition of 1-fM BPA (Figure 58a). Additionally, to further confirm the selectivity of the FET sensors, real-time responses were conducted with the addition 10 μM non-target molecule mixtures; some of the mixtures contained 1 fM BPA, while other mixtures contained no BPA. Figure 58b indicates significant signal changes after the addition of mixtures containing BPA, compared with the signal obtained for mixtures without BPA.

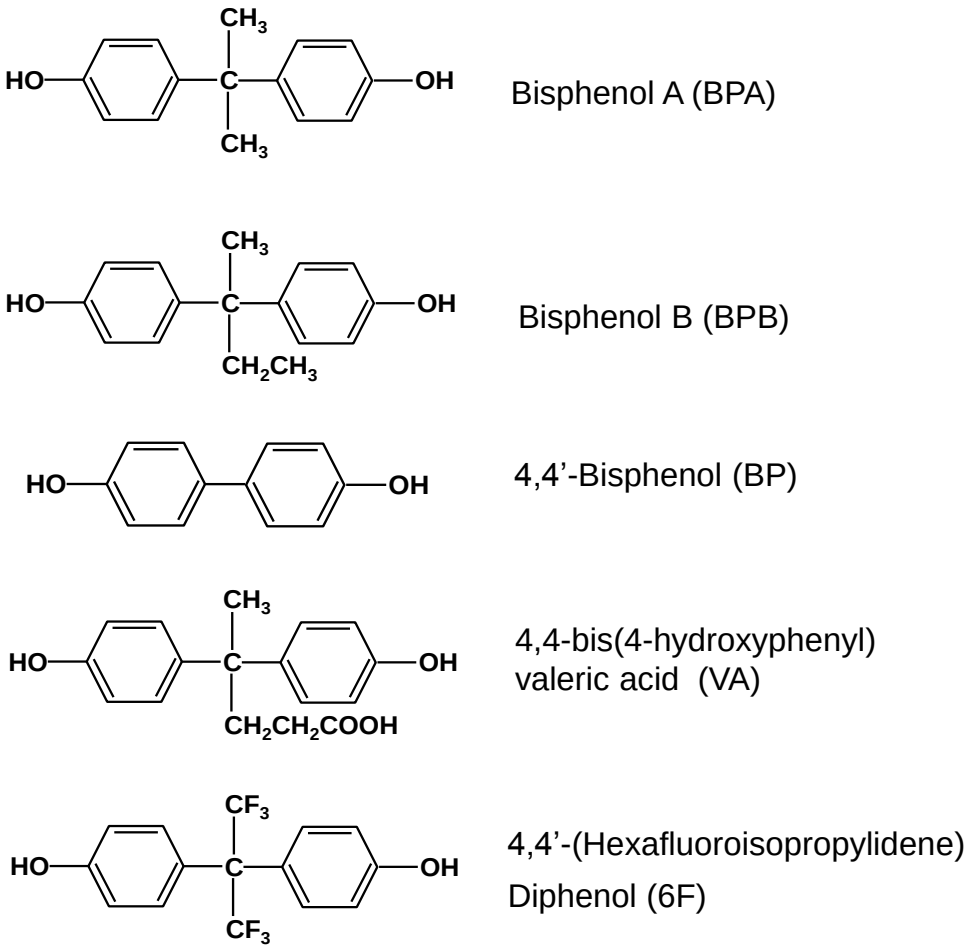

Figure 57. Molecular diagram of the bisphenol molecule family.

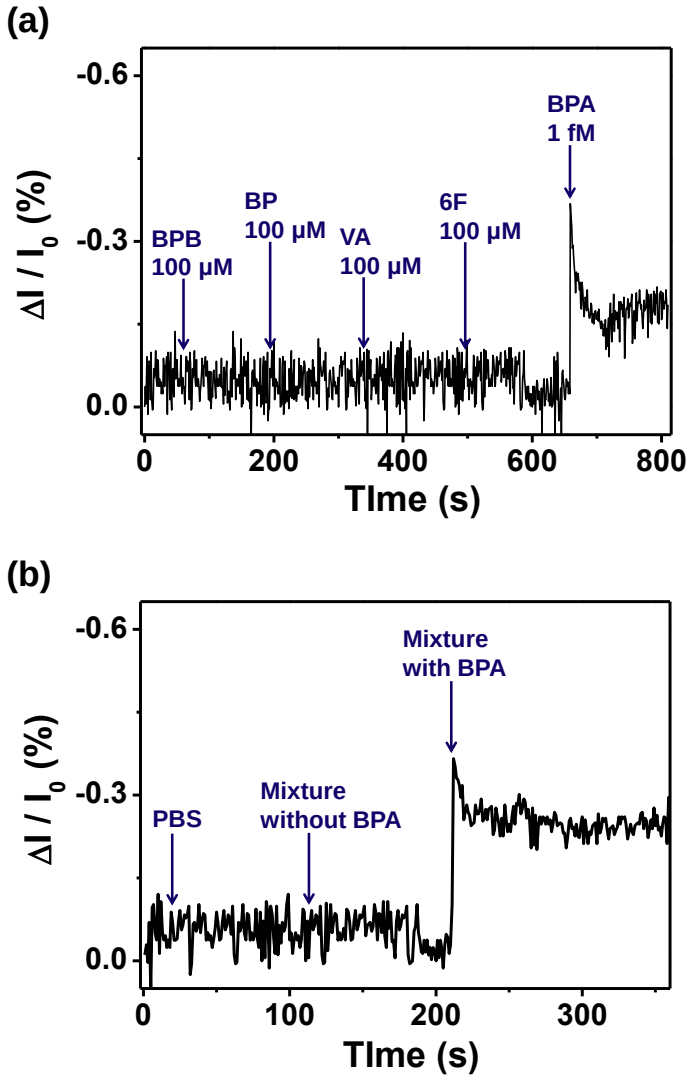

Figure 58. (a) Selectivity responses of the aptamer sensor using BPA-aptamer-30-nm-M_CPPyNPs toward non-target (bisphenol B (BPB), 4,4'-bisphenol (BP), 4,4-bis(4-hydroxyphenyl) valeric acid (VA), and 4,4-(hexafluoroisopropylidene) diphenol (6F)) and target (BPA) analytes. (b) Real-time response of the aptamer sensor for various analytes, before and after being mixed with BPA (V_G = 10 mV, V_{SD} = 10 mV).

The main advantage of the chemical-bonding-based FET system is repeated use (*i.e.*, a longer lifetime) than adsorption-based systems that require washing/rinsing processes for re-use. Figure 59 shows an estimation of the stability of diverse diameter A_M_CPPyNP FETs over several weeks. To confirm stability, the A_M_CPPyNP FET was stored in a sealed vessel at 25℃ for 4 weeks under air-dried conditions. The response of the A_M_CPPyNP FETs was displayed with 1 pM BPA concentration. Under these conditions, the sensitivity (S) decreased to *ca*. 20% after 4 weeks (21, 19, and 18% for 30, 60, and 100-nm NPs, respectively). This decrease in sensitivity was attributed to inactivation of the binding aptamer or the destruction of the nanoparticle array. However, the A_M_CPPyNP FETs maintained their other sensing abilities, such as selectivity and a minimum detectable level of BPA, despite the decrease in the response (Figure 60).

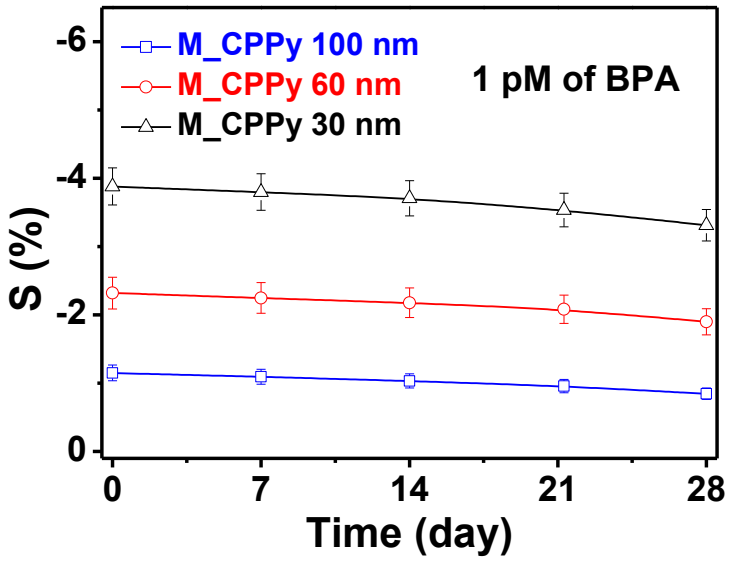

Figure 59. Comparison of the sensing performances of various BPA-aptamer M_CPPyNP-FET sensors undergoing 4 weeks of storage. Measurements were obtained at 1-week intervals (black: 30-nm-type; red: 60-nm-type; blue: 100-nm-type).

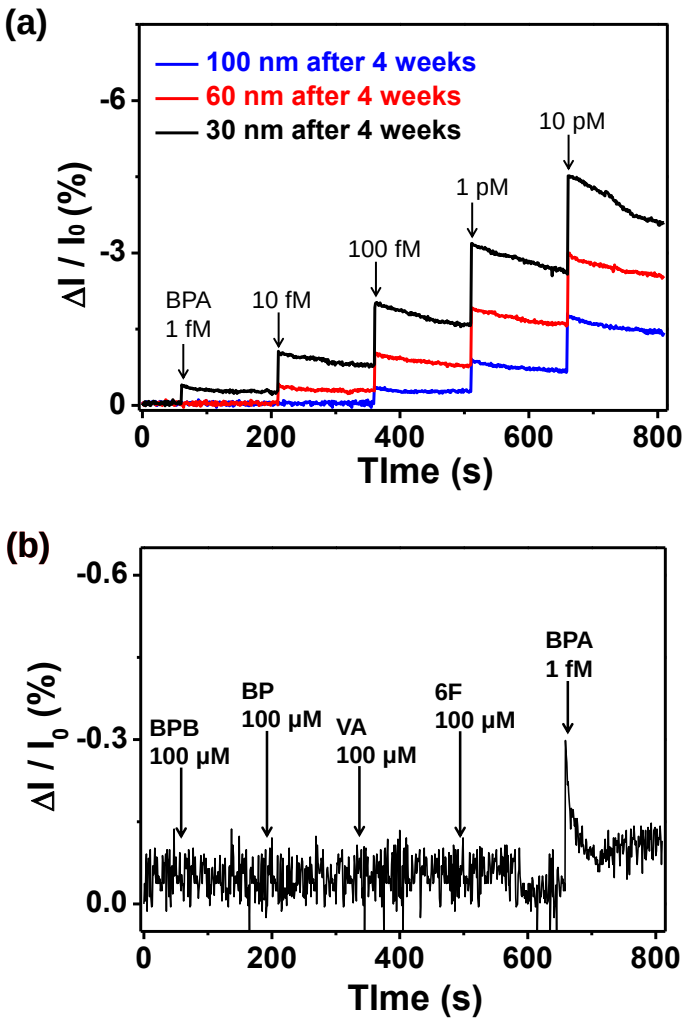

Figure 60. (a) Real-time response of various diameter A_M_CPPyNP FETs after 4 weeks, with normalized current changes. (b) Selectivity response of the aptamer sensor after 4 weeks using BPA aptamer-M_CPPyNP (30-nm) towards non-target (bisphenol B (BPB), 4,4-bisphenol (BP), 4,4-bis(4-hydroxyphenyl)valeric acid (VA), and 4,4-(hexafluoroisopropylidene)diphenol (6F)) and target analyte (BPA) (V_G = 10 mV, V_{SD} = 10 mV).

3.2. Multidimensional noble metal/conducting polymer hybrid nanoaprticles

3.2.1. Multidimensional platinum/carboxylated polypyrrole hybrid nanoparticles

3.2.1.1. Fabrication of multidimensional platinum/carboxylated polypyrrole hybrid nanoparticles

Figure 61 suggests the schematic diagram of the platinum nanoparticle decoration on the carboxylated polypyrrole nanoparticle (CPPyNP) surface through chemical reduction and following ultrasonication process. As shown in Figure 62a, aggregate-free 60-nm-diameter of CPPyNPs were prepared using a monodisperse method. The CPPyNPs were stirred in different concentration of $PtCl_4$ aqueous solutions at room temperature to induce covalent bonding between the Pt^{4+} ions and the negative charge of the O atom of the carboxylate group in the CPPy structure.[220] A small amount of $NaBH_4$ was added to the mixed CPPyNP solutions with ultrasonication for 2 h in order to reduce Pt^{4+} ions to Pt nanoparticles. Figure 62b and c represent the multidimensional platinum decorated carboxylated polypyrrole nanoparticles (Pt_CPPys) decorated with *ca*. 10 nm diameters of uniformly dispersed Pt particles on the surface.

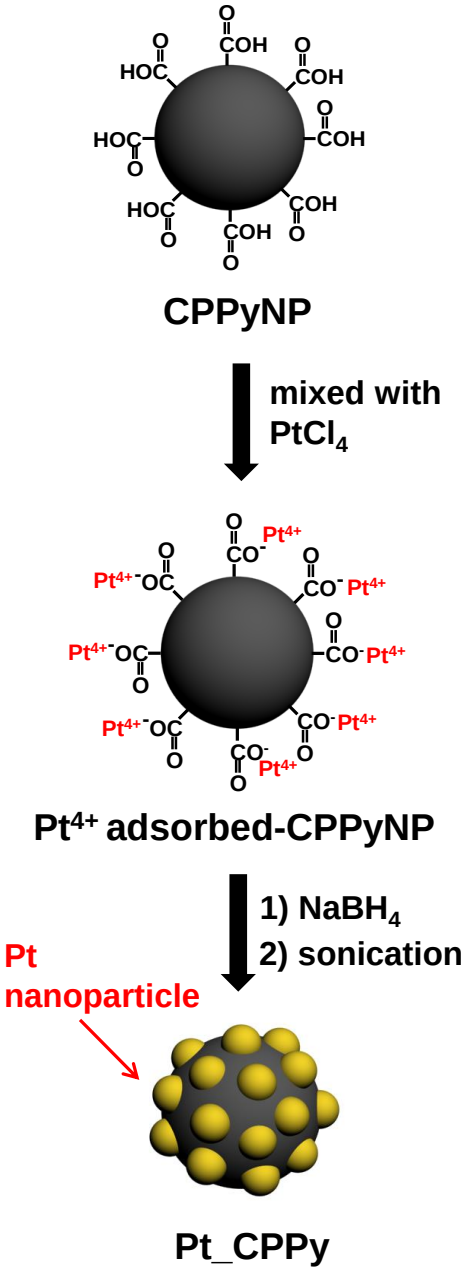

Figure 61. Illustrative diagram of the sequential fabrication steps for Pt particle decorated carboxylated polypyrrole nanoparticles (Pt_CPPys).

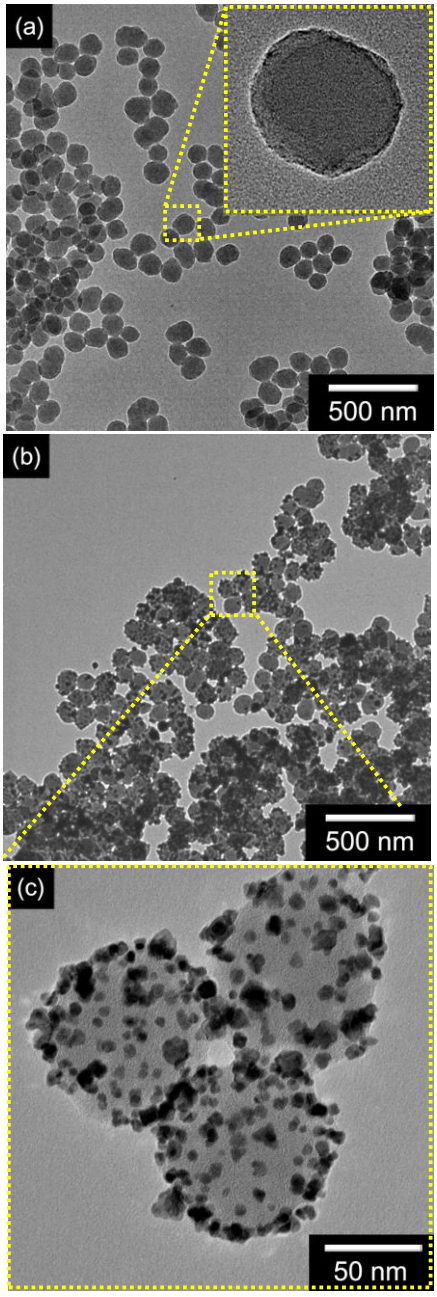

Figure 62. (a) TEM images of pristine CPPyNPs (inset: enlarged CPPyNP). (b) Low- and (c) high-resolution TEM images of Pt_CPPys.

Furthermore, the size and density of the decorated Pt nanoparticles were controlled by the concentration of the $PtCl_4$ aqueous solution, which varied from 0.5 to 20 mM. The nanostructures of the hybrid CPPys with 0.5, 2, 10, 15, and 20 mM $PtCl_4$ solutions are denoted as Pt_CPPy_0.5, Pt_CPPy_2, Pt_CPPy_10, Pt_CPPy_15, and Pt_CPPy_20 respectively. Figure 63 shows TEM and HR-TEM images of the hybrid CPPys with increasing precursor concentration. At low concentration (0.5 mM), *ca*. 5 nm diameter Pt particles sparsely decorate on the surface. The size and density of decorated Pt particles increase (*ca*. 10 nm) until 10 mM of Pt Cl_4 solution. However, over the 10 mM $PtCl_4$ concentration, Pt particles formed large scale structure rather than decorated on the CPPy surface, as suggested in the Figure 64. The HR-TEM image of Pt indicates an interplanar spacing 0.23 nm and 0.20 nm for the (111) and (200) of face-centered-cubic (fcc)-Pt and confirms growth of pure crystalline nanoparticles following treatment (Figure 63d). Additionally, to determine the crystallinity and composition of the particles, X-ray diffraction (XRD) using a JCPDS 00-004-0802 system and X-ray photoelectron spectroscopy (XPS) were used, respectively. The X-ray diffraction (XRD) patterns of the particles are demonstrated in Figure 65. The peaks of the inorganic material in hybrid CPPys can be well indexed to the fcc phase Pt (JCPDS 00-004-0802), indicating the formation of fcc phase Pt nanostructures

on the CPPy surface. As expected, the peak intensities for the Pt nanoparticles increase due to the enhancement in the nanoparticle density, following the concentration of Pt precursor. The chemical composition of the hybrid materials is also confirmed by X-ray photoelectron spectroscopy (XPS). Figure 66 exhibits the complete spectra over the range of 0-1000 eV. These overview spectra reveal that C, N, O and Pt atoms are suggested in Pt_CPPy_10, whereas only C, O and N are present in the pristine CPPy nanoparticles. The N 1s peak is attributed to the N component in the pyrrole structure (pyrrolylium nitrogen component and the positively charged N atoms). The high resolution XPS spectra for Pt show the Pt 4f peak (Figure 66b). Spin-orbit component $4f_{7/2}$ and $4f_{5/2}$ are observed near 71.0 eV and 74.3 eV, indicating that the valance state of Pt was +4.

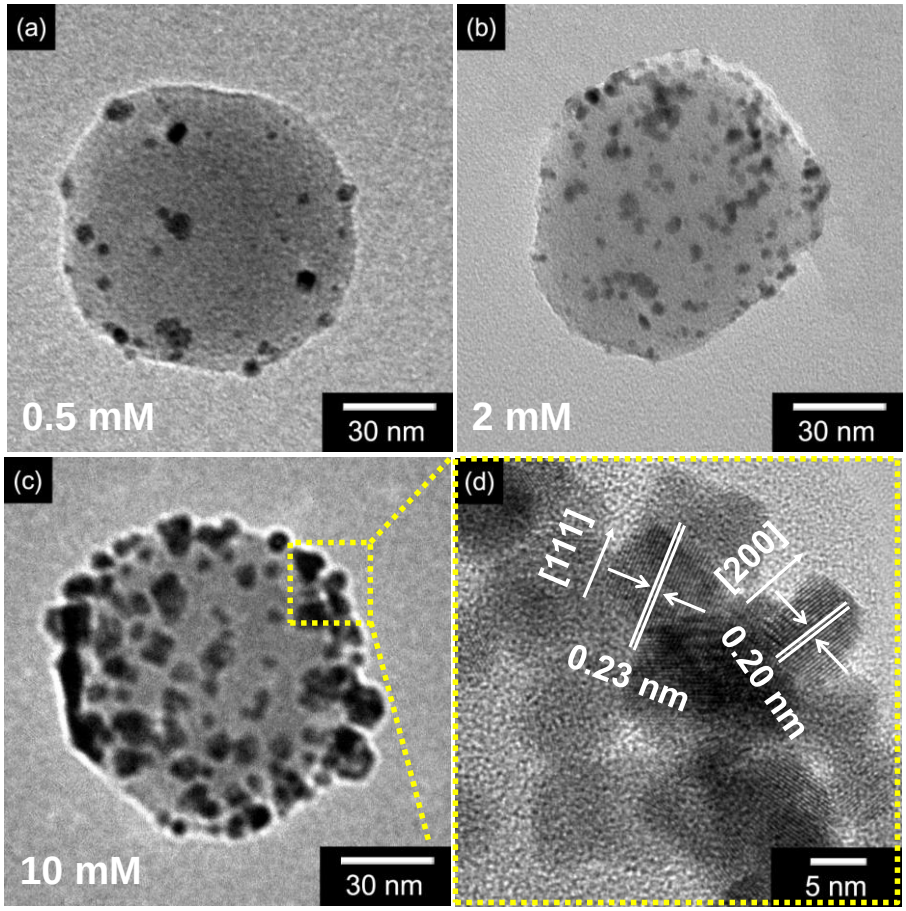

Figure 63. TEM images of Pt_CPPys with different concentration of $PtCl_4$ solutions: (a) 0.5 mM (Pt_CPPy_0.5), (b) 2 mM (Pt_CPPy_2), and (c) 10 mM (Pt_CPPy_10). (d) HR-TEM image of Pt particles on the Pt_CPPy_10 surface.

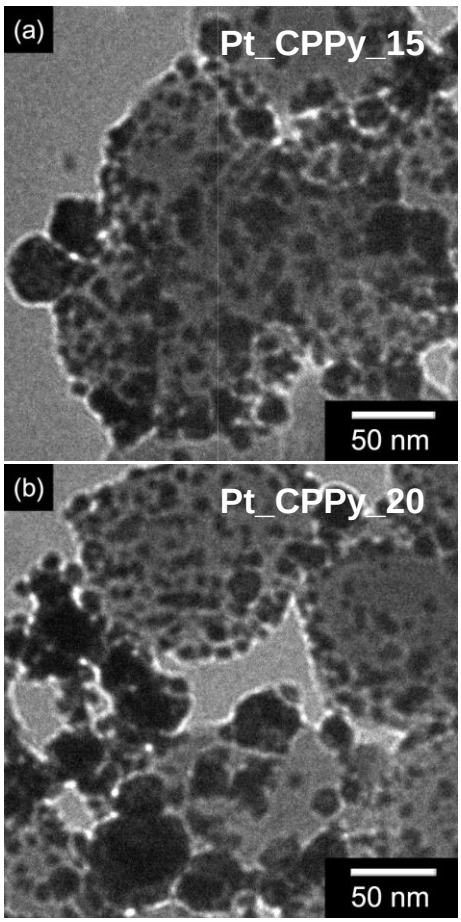

Figure 64. TEM images of Pt_CPPys with different concentrations of $PtCl_4$ solutions: (a) 15 mM (Pt_CPPy_15) and (b) 20 mM (Pt_CPPy_20).

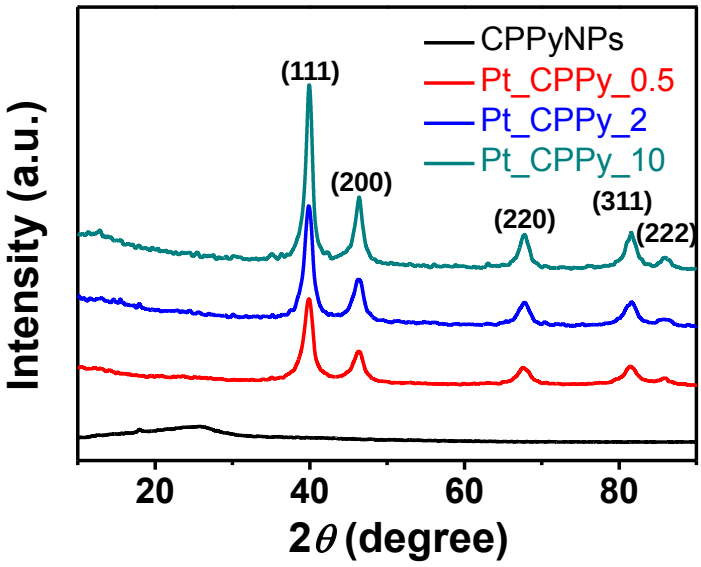

Figure 65. XRD pattern of various CPPy nanoparticles (black: CPPyNPs; blue: Pt_CPPy_0.5; green: Pt_CPPy_10).

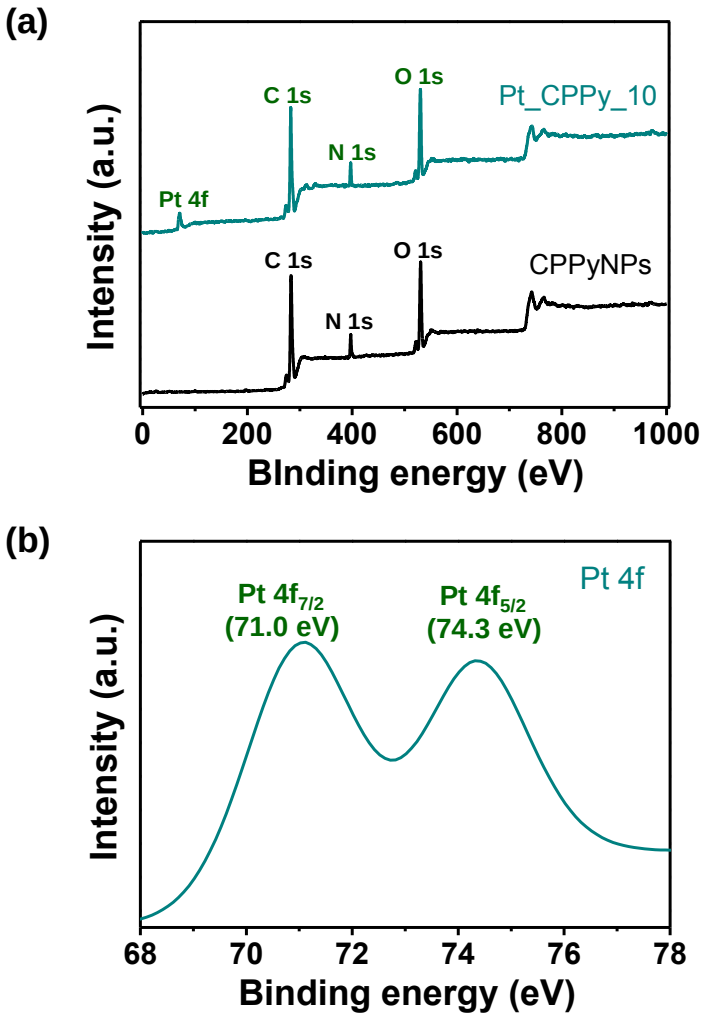

Figure 66. XPS patterns of (a) fully scanned spectra and high resolution of (b) Pt of hybrid CPPy nanoparticles (black: CPPyNPs; green: Pt_CPPy_10).

The stability in the liquid-ion solution is critical factor in the fabrication of highly sensitive non-enzyme FET sensor electrodes. To improve stability, the immobilization of the transducer on the sensor electrode is achieved *via* the covalent bonding of functional groups. Figure 67 provides a schematic diagram of the procedure for the Pt_CPPy based non-enzyme FET sensor configuration. An interdigitated microelectrode array (IDA), composed of pairs of 25 lines of gold fingers on the glass plate, was used as immobilization substrate of Pt_CPPys. The IDA glass substrate was treated with 3-aminopropyltrimethoxysilane (APS) to functionalize the surface with amine groups ($–NH_2$). Subsequently, the Pt_CPPys were anchored to the substrate through a condensation reaction between the carboxyl group (–COOH) of the particles and the $–NH_2$ of the substrate involving the condensing agent (4-(4,6-dimethoxy-1,3,5-triazin-2-yl)-4-methylmorpholinium chloride (DMT-MM)).[159] The carboxyl group of the Pt_CPPys facilitated the formation of a compact nanoparticle-array on the substrate. As a result, Pt_CPPys were immobilized on the electrode substrate, and they demonstrated outstanding stability against environmental perturbation. Figure 68 displays field-effect scanning electron microscopy (FE-SEM) images of the ordered packing on the IDA substrate. The arrays of ordered, packed hybrid NPs were clearly observed within the IDA. Then, the Pt_CPPy-immobilized IDA was formed FET-sensor

platform with PBS buffer solution (pH 7.4) as electrolyte. In the FET configuration, two gold IDA bands were the source (S) and drain (D) electrodes and gate electrode was immersed in the electrolyte. The gate potential (V_G) was applied to the source electrode through a buffer solution. The distance between electrodes was fixed at 2 mm based in the resistivity of the buffer solution.

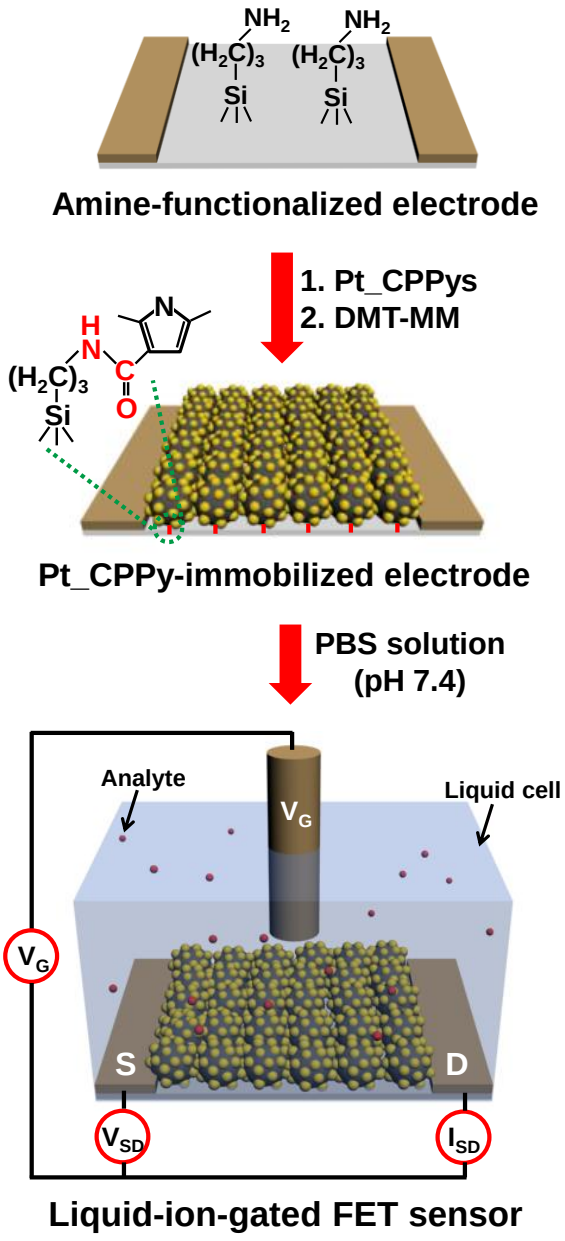

Figure 67. Schematic diagram of the liquid-ion-gated FET with the immobilized Pt_CPPy arrays on the IDA electrode.

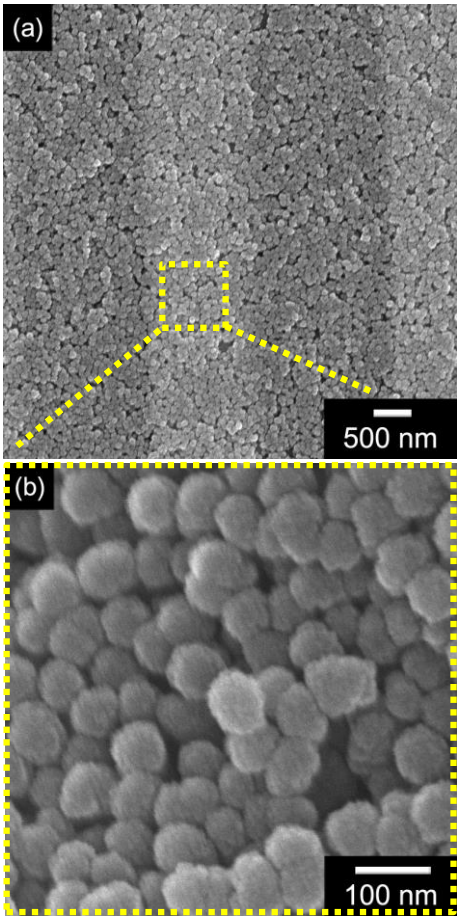

Figure 68. (a) Low- and (b) high-resolution FE-SEM images of immobilized arrays of the Pt_CPPys on the IDA substrate.

To characterize the electrical properties of the Pt_CPPys in the liquid phase, a FET configuration was constructed using an electrolyte as a liquid-ion gate. Current-voltage (I-V) curves were used to evaluate the electrical contact of the Pt_CPPys on the IDA substrate. Figure 69a shows the I_{SD}-V_{SD} characteristics (V_G = 0) of the various Pt_CPPys with different amount of Pt particle decoration. Pt_CPPys reveal linearity (*i.e.*, ohmic contact) for voltage range from -0.1 to 0.1 V, as opposed to the nonlinearity exhibition by Schottky barriers with poor electrical contact at the electrode. The dI/dV values of the electrodes increase as enhancing amount of Pt nanoparticles on the CPPy surface due to Pt particles enhance conductivity of CPPy particles. Furthermore, the dependence of the source-drain current (I_{SD}) with V_G variation (-20 to 100 mV) was investigated at a constant scan rate (10 mV s^{-1}) of source-drain voltage (V_{SD}) to verify the charge transport properties of Pt_CPPys in the FET configuration. Figure 69b demonstrates a plot of the I_{SD} versus V_{SD} for varying V_G for Pt_CPPy_10 electrode. The I_{SD} increases negatively with negative enhancing V_G, indicating p-type (hole-transport) behavior, caused by an increase in the oxidation level of the polymer chains. Additionally, other hybrid CPPyNPs (Pt_CPPy_0.5 and Pt_CPPy_2) suggest similar tendency except I_{SD} amounts with varying V_G (Figure 70). However, Pt_CPPy_15 and Pt_CPPy_20 display destruction of p-type charge transport properties in the

FET configuration owing to excess amount of Pt particles in the hybrid structure limits semi-conductive function of CPPy particles (Figure 71). Consequently, the dependence of I_{SD} on V_G is confirmed that proper amount of Pt contained Pt_CPPy FETs could be effectively used as an electrochemical sensor for detecting analytes in solution. The liquid-ion gate is capable of achieving increased transconductance, on account of the intimate contact between the particles and the gate, compared with conventional back-gating.

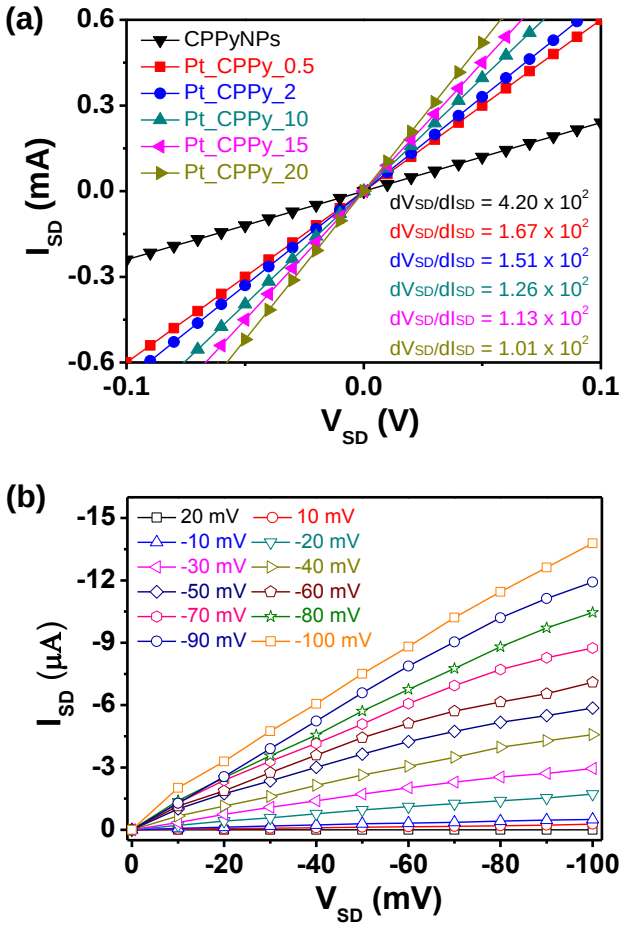

Figure 69. (a) Source-drain current-voltage (I_{SD}-V_{SD}) curves without gate potential (V_G) comparison of the IDA electrodes based on different Pt_CPPys (black: pristine CPPyNPs; red: Pt_CPPy_0.5; blue: Pt_CPPy_2; green: Pt_CPPy_10; pink: Pt_CPPy_15; yellow: Pt_CPPy_20). (b) Source-drain current versus source-drain voltage (I_{SD}-V_{SD}) characteristics of an Pt_CPPy_10 FET electrode for varying V_G ranging from 20 to -100 mV in 10 mV steps (V_{SD} scan rate: 10 mV s^{-1}).

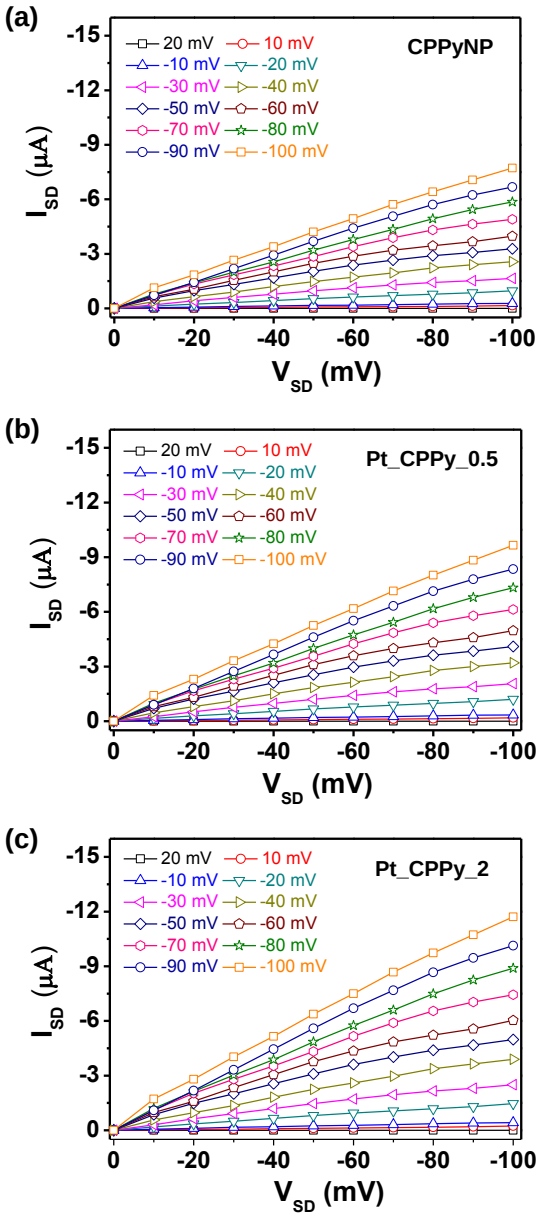

Figure 70. Source-drain current versus source-drain voltage (I_{SD}-V_{SD}) characteristics of (a) pristine CPPyNP, (b) Pt_CPPy_0.5, and (c) Pt_CPPy_2 FET electrodes for varying gate voltage (V_G) ranging from 20 to -100 mV in 10 mV steps (V_{SD} scan rate: 10 mV s^{-1}).

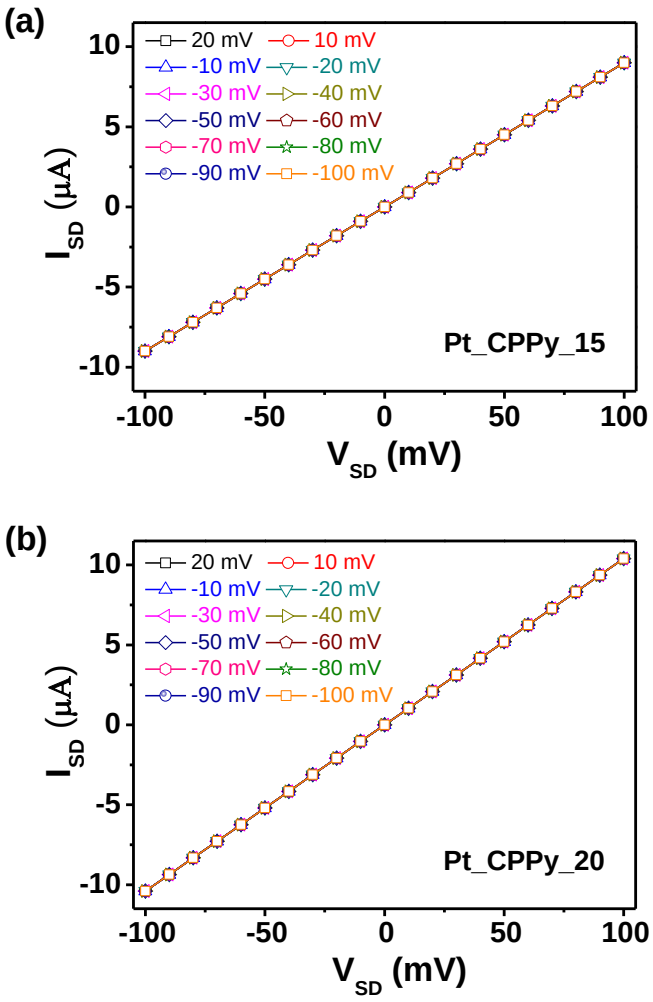

Figure 71. Source-drain current versus source-drain voltage (I_{SD}-V_{SD}) characteristics of (a) Pt_CPPy_15 and (b) Pt_CPPy_20 FET electrodes for varying gate voltage (V_G) ranging from 20 to -100 mV in 10 mV steps (V_{SD} scan rate: 10 mV s^{-1}).

3.2.1.2. Application for dopamine biosensor

The uniformly immobilized Pt_CPPys on the FET sensor electrode rapidly detect dopamine molecules at room temperature. The sensing mechanism of the hybrid CPPyNPs is described in the Figure 72. The CPPy surface is adsorbed to dopamine molecules by pi-pi interactions through conjugated five membered ring of CPPy and six membered benzene ring of dopamine structure. The adsorbed dopamine is electro-oxidized to O-dopaminequinone at the surface of the Pt particles through catalytic effect and electrons, originated from dopamine, are transferred to CPPy, leading to a decrease in the number of holes in the CPPy structure and diminishing I_{SD} (because CPPy acts as a p-type transducer).

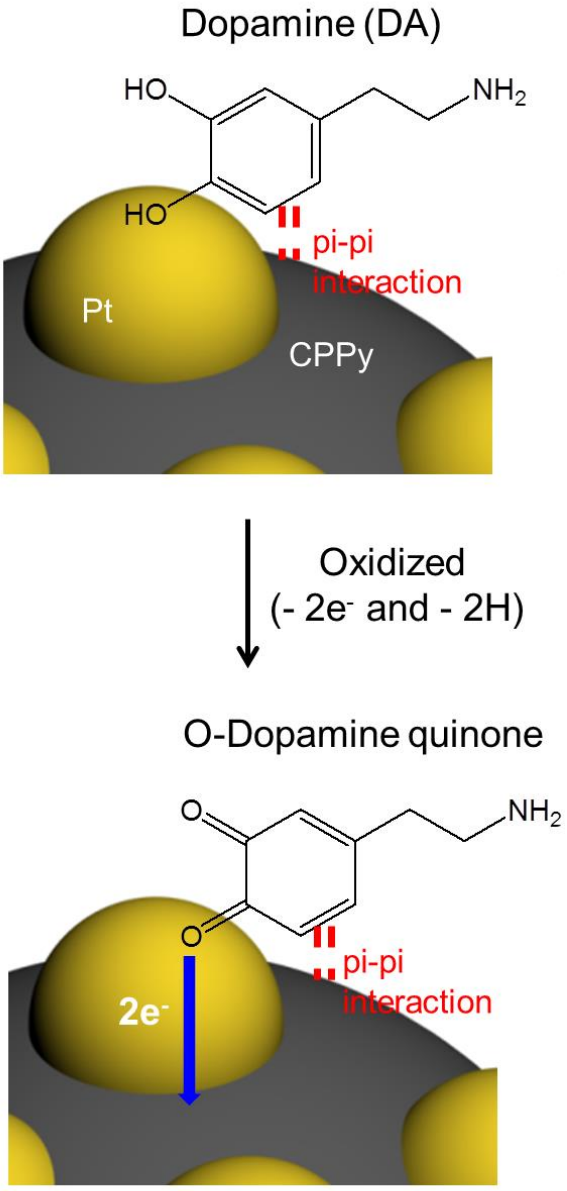

Figure 72. Dopamine molecule detection mechanism of Pt_CPPy FET sensors at room temperature.

To investigate the sensing characteristics of the liquid-ion-gated Pt_CPPy FET, the I_{SD} was monitored in real time at a V_G of 10 mV (V_{SD} = 10 mV), a low operating voltage, upon the addition of various concentration of dopamine. Figure 73a shows the real-time response of the Pt_CPPy FET sensors with different decorated Pt particle amounts as a function of dopamine (DA) sensors. Upon each addition of DA, the I_{SD} decreases rapidly over a 1 s period before its saturated value. The sensitivity of the Pt_CPPy FETs increases as the enhancing Pt decoration amounts; that is, the Pt_CPPy FET made from the Pt_CPPy_10 is capable of detecting dopamine concentrations as low as 100 fM at room temperature. The larger-amount of Pt particles have a higher density of chemical functionality (degree of Pt catalytic activity), compared with less Pt decorated CPPyNPs. Therefore, a better sensitivity is achieved with large amount of Pt particles as a result of the enhancing catalytic activity to the oxidation of dopamine molecules. Figure 73b dispalys the changes in sensitivity as a function of Pt particle density for the Pt_CPPys, with respect to dopamine concentration. The sensitivity (S) is determined from the saturation point of the normalized current change ($(\Delta I/I_0)_{SD} \times 100$), measured 10 s after the dopamine addition. At low concentrations (<100 fM), the Pt_CPPy FET sensors describe nonlinear changes in sensitivity. In contrast, linear behavior is observed over a wide concentration range (100 fM – 1 nM).

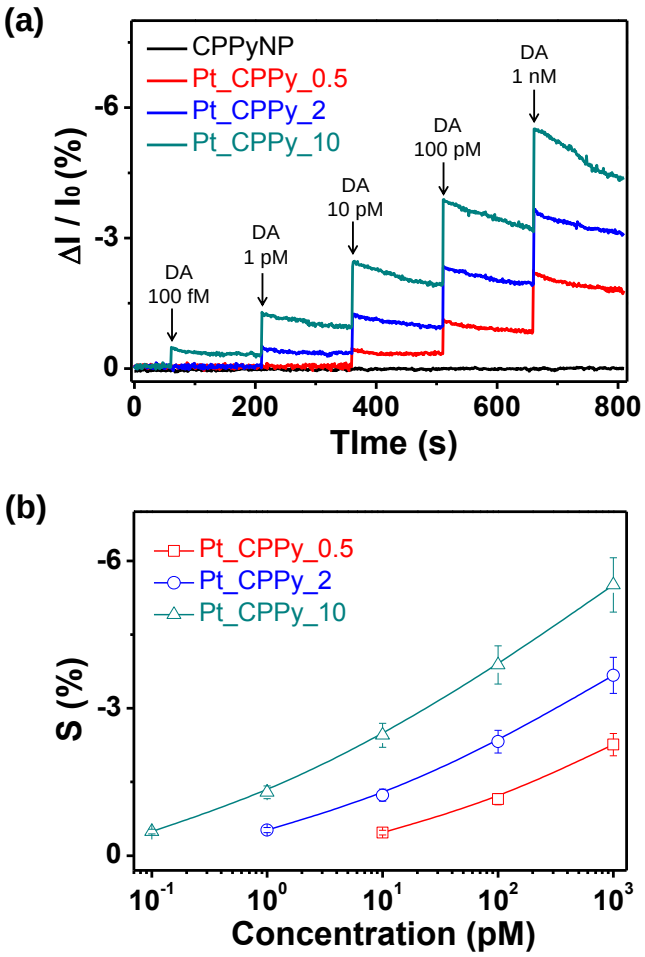

Figure 73. (a) Real-time response for the FETs comprising various Pt particle densities of Pt_CPPys, with normalized current changes ($\Delta I/I_0 = (I-I_0)/I_0$, where I_0 is the initial current and I is the instantaneous current). (b) Calibration curves of FETs comprising various Pt particle densities of Pt_CPPys as a function of dopamine concentration (S indicates the normalized current change after 10 s of dopamine exposure). Black, red, blue, and green represent FETs originate from the pristine CPPyNPs, Pt_CPPy_0.5, Pt_CPPy_2, and Pt_CPPy_10, respectively (V_G = 10 mV, V_{SD} = 10 mV).

The selectivity of the Pt_CPPy_10 FET towards the dopamine molecule was investigated for four organic molecules: ascorbic acid (AA) / uric acid (UA) that are present together in some biological tissues with dopamine (DA) and epinephrine (EP) / norepinephrine (NE) that have similar molecular structure to DA (Figure 74). The Pt_CPPy sensor shows no significant I_{SD} changes with the addition of each non-target molecules (100 pM: AA, UA, and EP; 50 pM: EP): however, considerable I_{SD} changes are evident upon the addition of 100 fM dopamine (Figure 75a). Additionally, to further confirm the selectivity of the FET sensors, real-time responses were conducted with the addition non-target molecule mixtures (100 pM: AA, UA, and EP; 50 pM: EP); some of the mixtures contained 100 fM dopamine, while other mixtures without dopamine. Figure 75b displays significant signal changes after the addition of mixtures containing dopamine, compared with the signal obtained for mixtures without dopamine. Additionally, Table 5 summarized sensing ability of Pt_CPPy_10 nanoparticle based FET electrode with different analytes. The pi-pi interaction between phenyl structure of DA and CPPy structure is attributed to the easy adsorbed DA molecules to the surface of Pt_CPPy-based electrode. On the other hand, AA and UA exhibit weaker adsorbed interactions than DA molecules due to absence of phenyl group in the molecular structure. Figure 76 suggests pi-pi interaction analysis of each bio-

molecules using XPS spectra. The C 1s spectra of before exposure are deconvoluted into six components as follows: the 284.3 eV for C=C bonds, the 285.3 eV for C-C bonds, the 286.6 eV for C-O bonds, the 284.9 eV for C-N bonds, the 287.8 eV for carbonyl, and the 289.0 eV for carboxyl groups, respectively. After exposed to 100 pM of ascorbic acid (AA) and uric acid (UA), the C 1s peaks of Pt_CPPys maintained its original value (Figure 76b and c). However, the C 1s spectra changed after exposed 100 pM of DAs with increasing peaks of the C=C (284.3 eV), the C-O (286.6 eV), and the C-N (284.9 eV) bonds owing to bonded DA molecules on the CPPy surface (Figure 76d). Therefore, DA molecules bonded to CPPy surface through specific interactions (pi-pi interaction) that caused higher sensitivity at FET sensor application than other two bio-molecules (AA and UA). However, despite of similar structure to DA, EP and NE reveal lower sensitivity than DA. The additional functional groups (–OH and $–CH_3$) at ethylamine group enlarged size of bio-molecules, so it might be restricted pi-pi interactions with CPPy surface and catalytic effect of Pt particles. As a result, the Pt_CPPy FET sensor exhibits high selectivity to the dopamine molecules in presence of excess interferents.

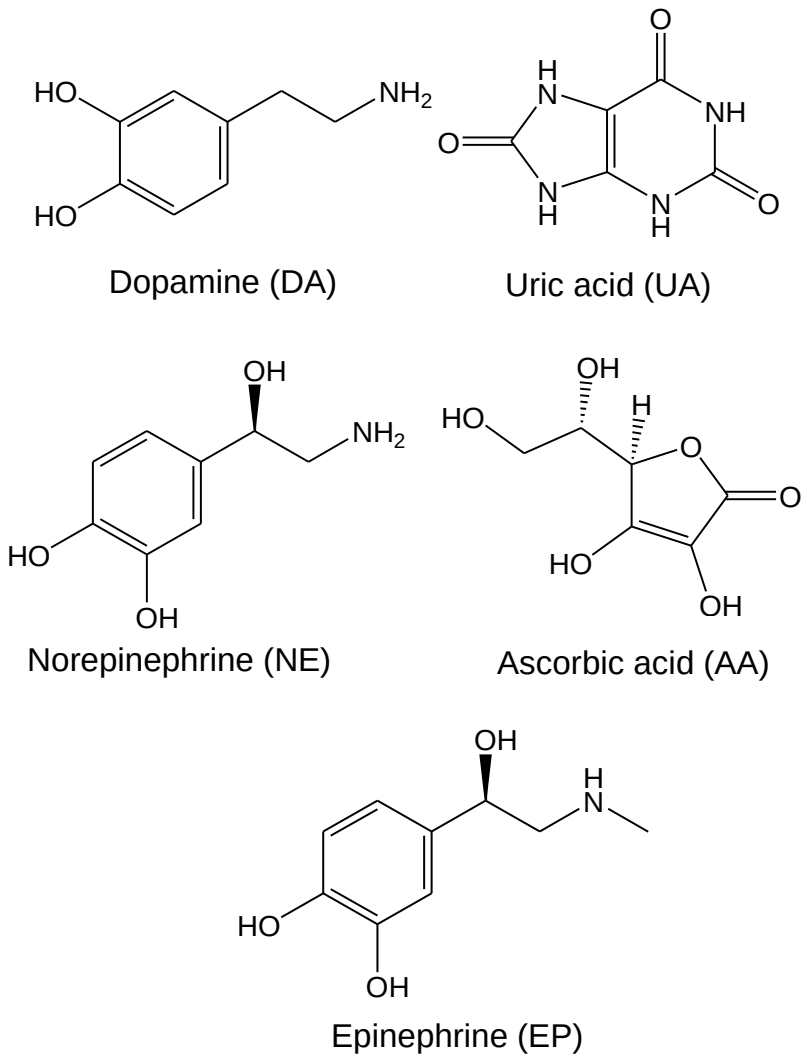

Figure 74. Molecular diagram of the different biomolecules.

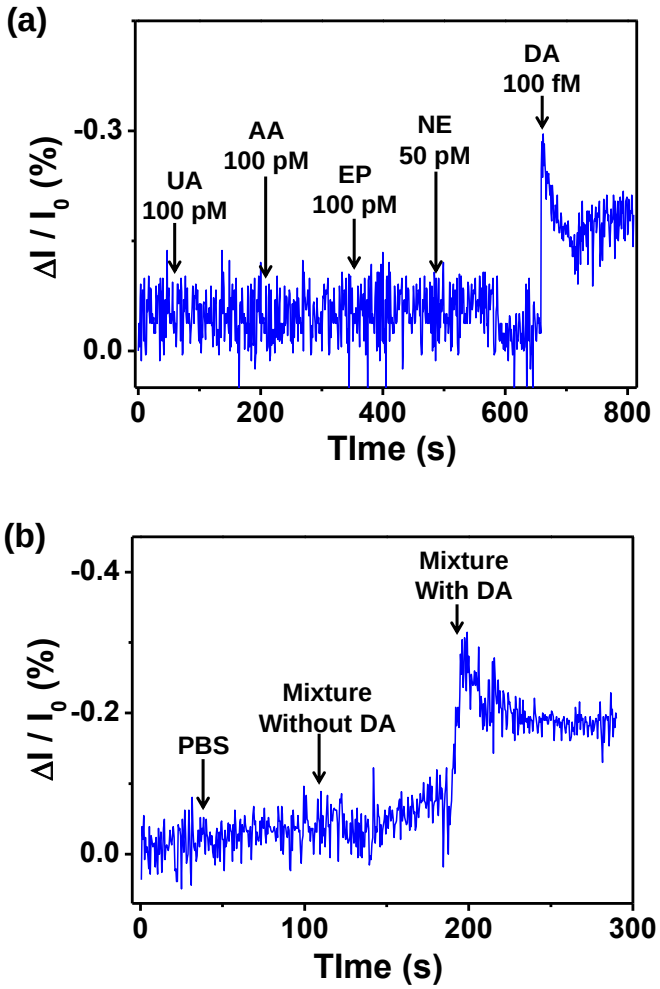

Figure 75. (a) Selectivity responses of the Pt_CPPy FET sensors toward non-target (ascorbic acid (AA), uric acid (UA), epinephrine (EP), and norepinephrine (NE)) and target (dopamine (DA)) analytes. (b) Real-time response of the non-enzyme sensor for various analytes, before and after being mixed with dopamine (V_G = 10 mV, V_{SD} = 10 mV).

Table 5. Sensing ability of Pt_CPPy_10 based-FET electrode with different biomolecules.

	MDL[a]	Response time (s)
Dopamine (DA)	100 fM[b]	0.4
Uric acid (UA)	150 pM[c]	1.2
Norephinephrine (NE)	140 pM	1.3
Acetic acid (AA)	210 pM	1.1
Epinephrine (EP)	70 pM	1.3

[a] Minumum detactable level,

[b] 10^{-15} M,

[c] 10^{-12} M

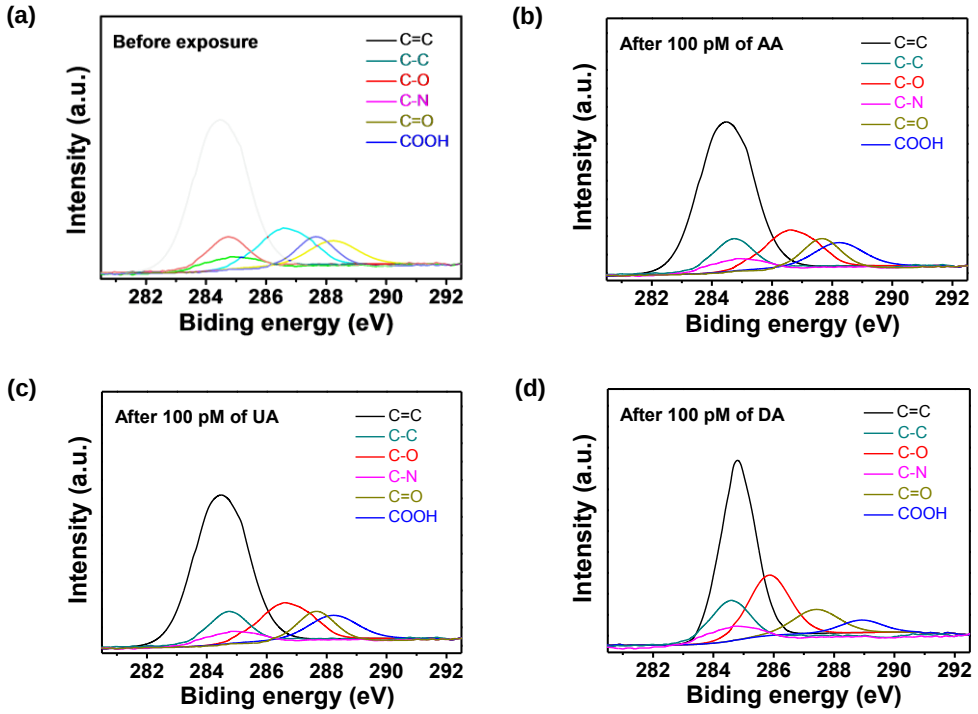

Figure 76. High resolution C 1s XPS spectra of Pt_CPPy FET sensor at (a) before exposure and after exposing of 100 pM (b) ascorbic acid (AA), (c) uric acid (UA), and (d) dopamine (DA), respectively.

The main advantage of the chemical-bonding-based FET system is the repeated use (*i.e.*, a longer lifetime); in contrast, adsorption-based systems that require washing/rinsing process for re-use. Figure 77 illustrates an estimation of the stability of the FETs based on Pt_CPPys of various Pt densities over several weeks. To confirm stability, the Pt_CPPy FETs were stored in a sealed vessel at 25℃ for 4 weeks under air-dried conditions. The response (S) of the various Pt_CPPy FETs is displayed with 100 pM dopamine concentration. Under this condition, the S maintain after 4 weeks on account of following reasons. First, the Pt_CPPy FET sensor systems are not concerned enzymatic bio-receptors (*e.g.*, aptamer and antibody) that caused inactivation at harsh conditions. Second, covalent chemical bonding (amide bond) between CPPyNPs and sensor electrodes prohibit destruction of the nanoparticle arrays. Furthermore, the Pt_CPPy FETs maintain their other sensing abilities, such as selectivity and minimum detectable level (MDL) of dopamine without any decrease in the response. Additionally, the morphology of Pt_CPPys remains after DA detection for four weeks (Figure 78). Therefore, the decorated Pt particles on the CPPy surface also maintain after DA detection process.

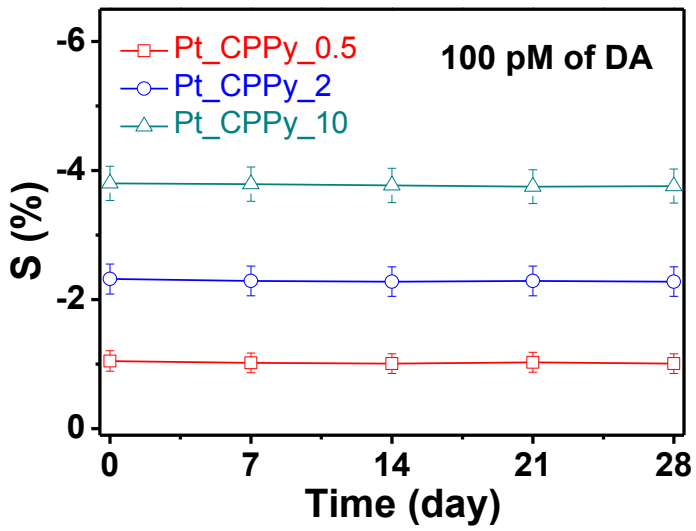

Figure 77. Sensing performance comparison of various hybrid CPPyNP-FET sensors during 4 weeks of storage. Measurements were obtained at 1-week intervals. The hybrid CPPyNPs are Pt_CPPy_0.5 (red), Pt_CPPy_2 (blue), and Pt_CPPy_10 (green), respectively.

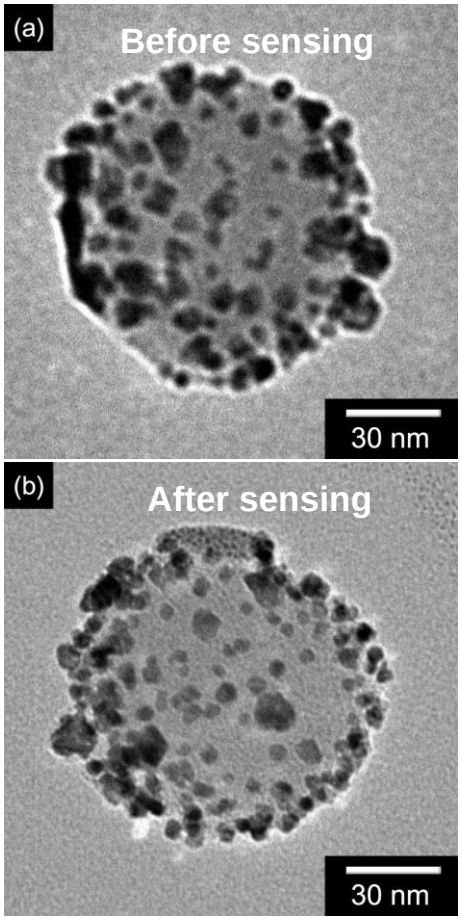

Figure 78. TEM images of Pt_CPPy_10 nanoparticle (a) before and (b) after dopamine sensing for 4 weeks.

3.2.2. Multidimensional porous palladium/carboxylated polypyrrole hybrid nanoparticles

3.2.2.1. Fabrication of multidimensional porous palladium/carboxylated polypyrrole hybrid nanoparticles

Figure 79 displays the overall procedure for the fabrication of multidimensional porous palladium decorated carboxylated polypyrrole nanoparticles (M_PdCPPys), based on chemical reduction process. First, aggregate-free 60 nm diameter of carboxylated polypyrrole nanoparticles (CPPyNPs) were prepared using a monodisperse method (Figure 80a and b). CPPyNPs were stirred in different alkylamine contained ethanol solution (hexylamine (C_6H_{13}-NH_2), decylamine ($C_{10}H_{21}$-NH_2), and hexadecylamine ($C_{16}H_{33}$-NH_2)) at room temperature. Then, the alkylamines were bonded to CPPyNPs through a condensation reaction between the carboxyl group (-COOH) of the nanoparticles and the $–NH_2$ of the alkylamines using the condensing agent (4-(4,6-dimethoxy-1,3,5-triazin-2-yl)-4-methylmorpholinium chloride (DMT-MM)). Subsequently, $PdCl_2$ ethanol solution was added to alkyl functionalized CPPyNP (A_CPPyNP) contained solutions to induce covalent bonding between the Pd^{2+} ions and the negative charge of O atom of the amide bonding in the A_CPPyNP structure. A small amount of $NaBH_4$ was added to mixed A_CPPyNP solutions with sonication for 2 h in order to reduce Pd^{2+} ions to Pd^0 nanoarchitectures, resultingly, multidimensional porous palladium

decorated carboxylated polypyrrole hybrid nanoparticles (M_PdCPPys) were formed. During reduction process, alkyl chain acted as nucleation site to form porous architecture of palladium structure. To confirm the role of alkyl chain for formation of porous palladium architecture, Pd^{2+} reduction process using without alkyl functionalized CPPyNPs was conducted. As shown in the Figure 80c and d, *ca*. 5 nm diameters of palladium particles were uniformly dispersed on the surface (denoted as PdCPPy) compared to M_PdCPPys. Additionally, palladium architectures without CPPyNPs suggested as largely aggregated (*ca*. 300 nm-diameter) particle morphology that also confirmed the effect of CPPyNPs during palladium formation process on the surface (Figure 81).

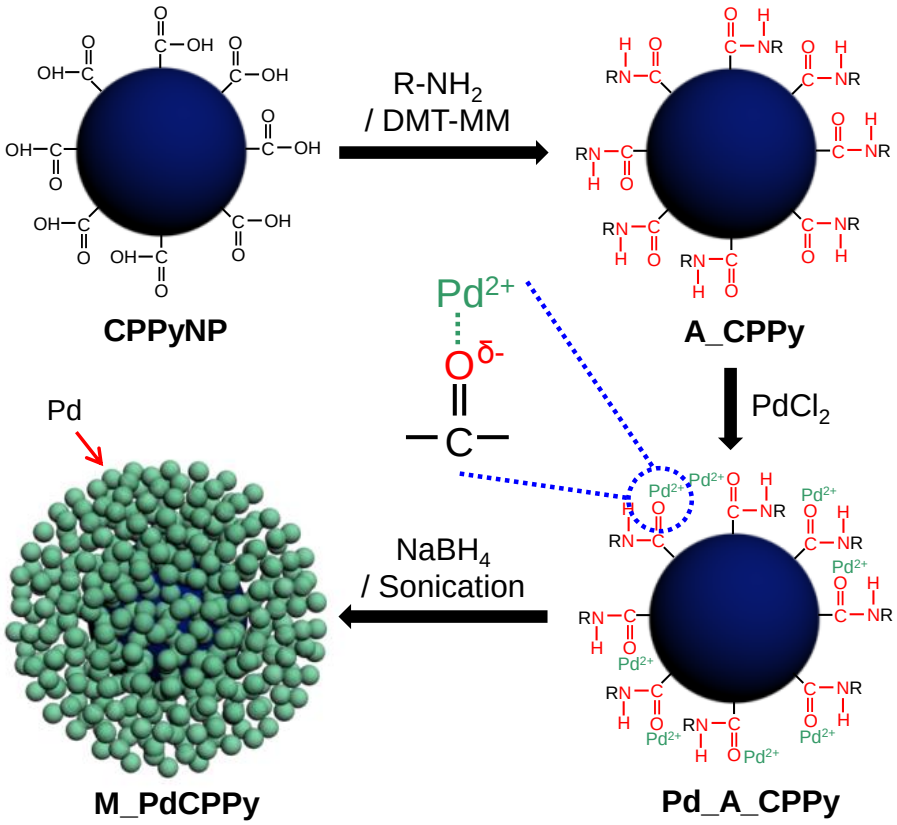

Figure 79. Illustrative diagram of the sequential fabrication steps for multidimensional palladium decorated carboxylated polypyrrole hybrid nanoparticles (M_PdCPPy).

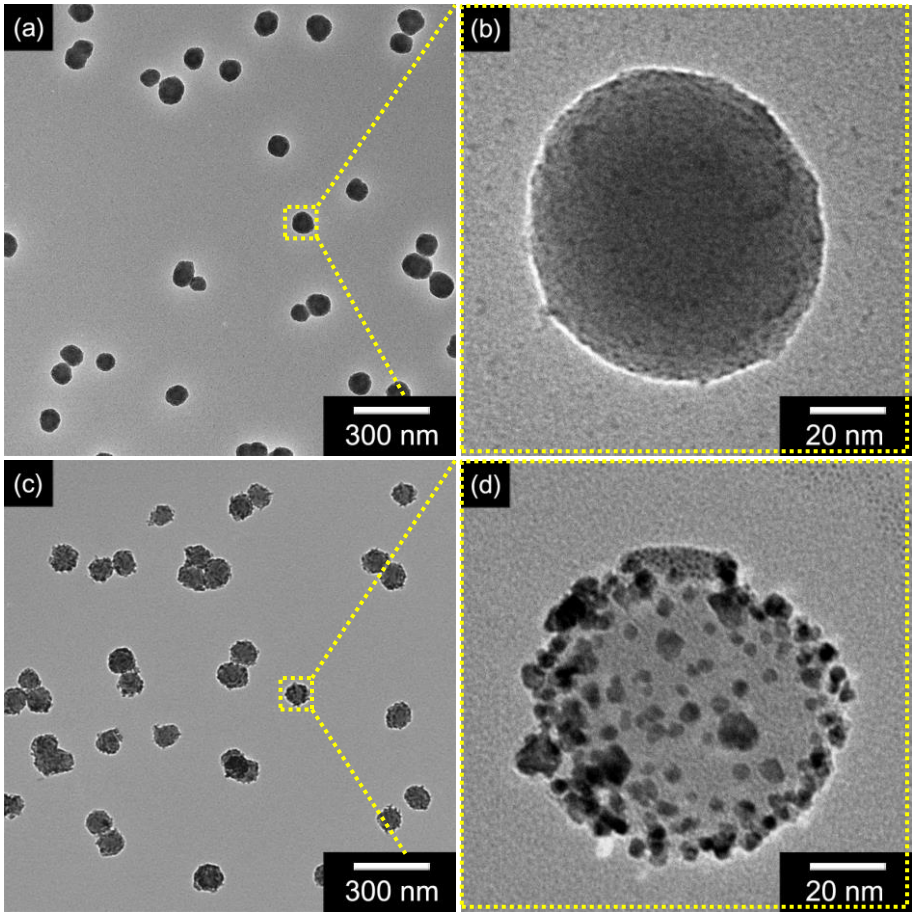

Figure 80. (a) Low- and (b) high-magnified transmission electron microscope (TEM) images of pristine carboxylated polypyrrole nanoparticles (CPPyNPs). (c) Low- and (d) high-resolution TEM images of palladium decorated carboxylated polypyrrole hybrid nanoparticles (PdCPPy).

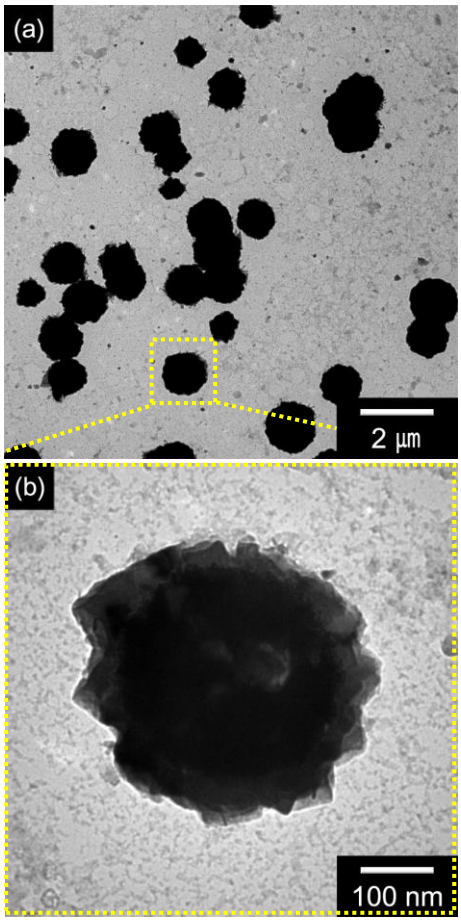

Figure 81. (a) Low- and (b) high-magnification TEM images of palladium architectures without CPPyNPs during fabrication step.

Furthermore, the size of the decorated palladium architectures was controlled by the length of alkyl chain, which varied from hexyl (C6) to hexadecyl (C16). The M_PdCPPys functionalized with hexylamine (C_6H_{13}-NH_2), decylamine ($C_{10}H_{21}$-NH_2), and hexadecylamine ($C_{16}H_{33}$-NH_2) solutions are denoted as M_PdCPPy_C6, M_PdCPPy_C10, and M_PdCPPy_C16, respectively. Figure 82 suggest transmission electron microscopy (TEM) images of the M_PdCPPys with increasing length of alkyl chains. At small length of alkyl chain (C6), thickness of porous palladium layer on the surface was *ca*. 10 nm. The thickness of decorated palladium layers increased to *ca*. 30 nm at C16 of alkyl chain. Additionally, to determine the atomic distribution, scanning TEM (STEM)/energy dispersive X-ray (EDX) line analysis was performed in M_PdCPPy_C16, as shown in Figure 83a. The hybrid nanoparticles exhibited regions rich in nitrogen (yellow) and palladium (pink) corresponding to the core (CPPy)/shell (palladium) regions, respectively. The line width difference between palladium and nitrogen revealed *ca*. 30 nm, which agreed with the TEM image. The high-resolution transmission electron microscopy (HR-TEM) image of palladium layer indicates interplanar spacings 0.23 nm and 0.20 nm for the (111) and (200) of face-centered-cubic fcc-Pd and confirms growth of pure crystalline nano-sized porous layered following treatment (Figure 83b).

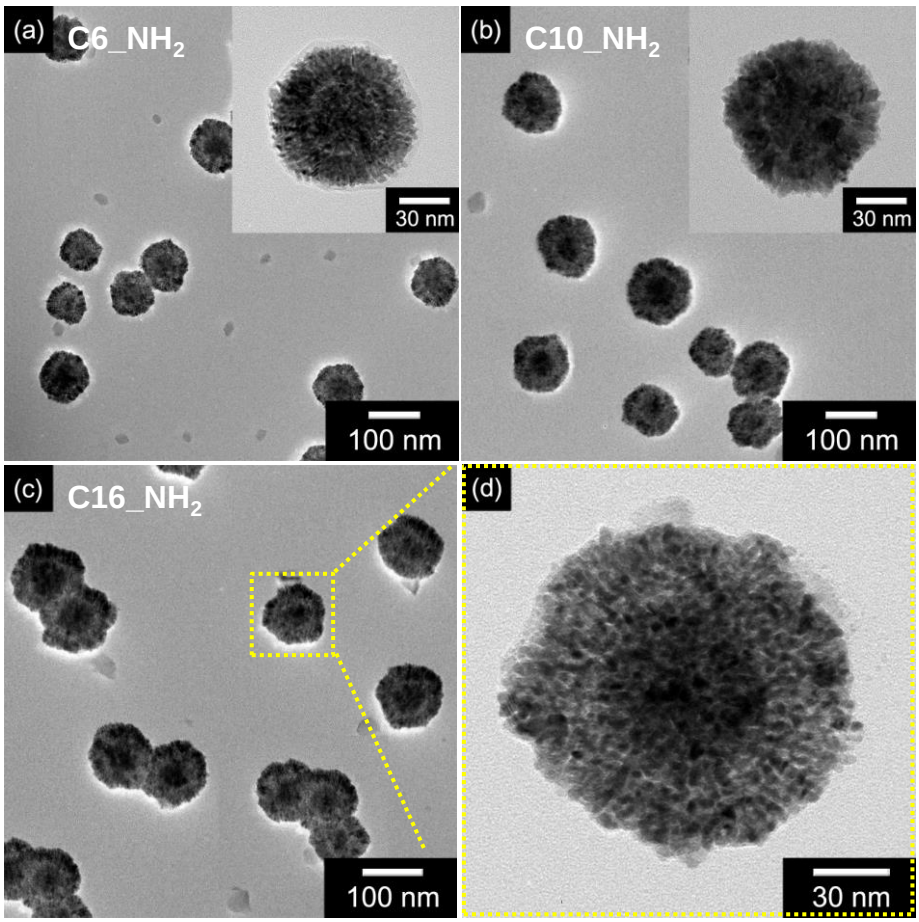

Figure 82. Low- and high-resolution (inset) transmission electron microscopy (TEM) images of M_PdCPPy with different length of bonding alkyl chains: (a) C6-NH_2 (M_PdCPPy_C6) and (b) C10-NH_2 (M_PdCPPy_C10). (c) Low- and (d) High-magnified TEM images of M_PdCPPy with C16-NH_2 bonding alkyl chain (M_PdCPPy_C16).

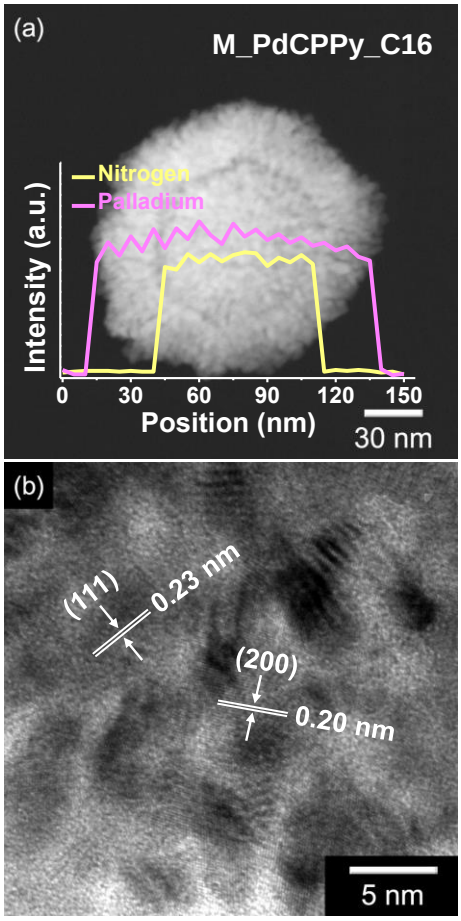

Figure 83. (a) Scanning TEM (STEM) and energy disperse X-ray (EDX) line analysis of M_PdCPPy_C16. (b) High-resolution TEM (HR-TEM) image of palladium architectures on the M_PdCPPy_C16 surface.

In addition, to confirm the crystallinity and composition of M_PdCPPys, X-ray diffraction (XRD) and X-ray photoelectron spectroscopy (XPS) were used, respectively. The x-ray diffraction (XRD) patterns of the particles are suggested in Figure 84. The peak of the inorganic materials in the PdCPPy and M_PdCPPy hybrid particles can be well indexed to the fcc-Pd (JCPDS 05-0681), indicating the formation of fcc-Pd nanostructures on the carboxylated polypyrrole (CPPy) surface. As expected, the peak intensities for the fcc-Pd architecture increased due to the enhancement of decorated palladium amount through alkyl functionalization. The broad diffraction peaks at 25.6 cm^{-1} were observed for all samples, indicating an identical crystalline CPPy structure for all of the samples. The chemical composition of the hybrid materials was also confirmed by X-ray photoelectron spectroscopy (XPS). Figure 85a shows the complete spectra over the range of 0-1200 eV. These overview spectra revealed that C, N, O, and Pd atoms were presented in the PdCPPy and M_PdCPPy samples, whereas only C, O, and N were represented in the CPPyNPs. The N 1s peak was attributed to the N component in the CPPy structure (pyrrolylium nitrogen component and the positively charged N atoms). The high-resolution XPS spectra of hybrid particles for the C 1s region around 285 eV are demonstrated in Figure 85b; this peak was deconvoluted into four components. The peak at 294.3 eV was attributed to C=C bonds and the 285.3 eV peak

corresponded to the C-C bond. In particular, the ratio of C-O (286.6 eV) and C-N (284.9 eV) groups were displayed enhancement at M_PdCPPy case owing to formation of amide group (-CONH-) during alkyl chain functionalization. The high resolution XPS spectra for Pd of PdCPPy and M_PdCPPy describe the Pd 3d peaks (*ca*. 335 – 341 eV). The Pd 3d core spectrum was fitted using two components, as shown in Figure 85c. The prominent peaks at 335 and 341 eV are assigned to the neutral Pd state, whereas the weaker features at 335 and 341 eV are attributed to PdO originated from bonding with oxygen atom at amide group. No obvious peak for Pd^{2+} species was founded (*ca*. 338 eV), indicating that most Pd cations of $PdCl_2$ were reduced to neutral Pd during reducing process.

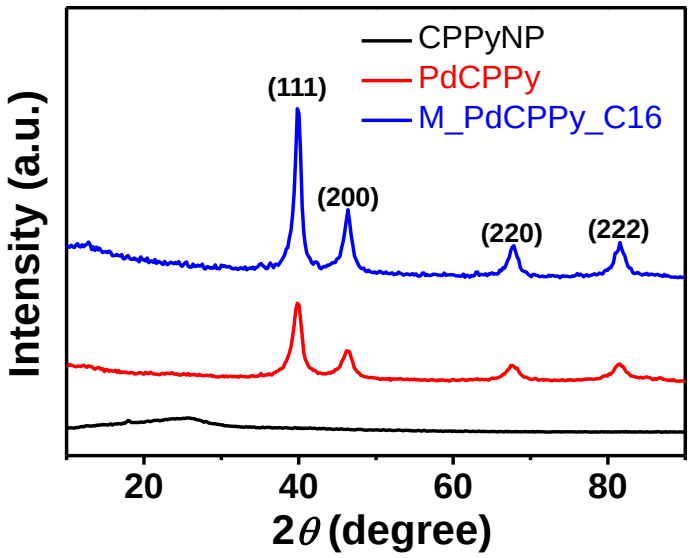

Figure 84. X-ray diffraction (XRD) spectra of various CPPys (black: CPPyNP; red: PdCPPy; blue: M_PdCPPy_C16).

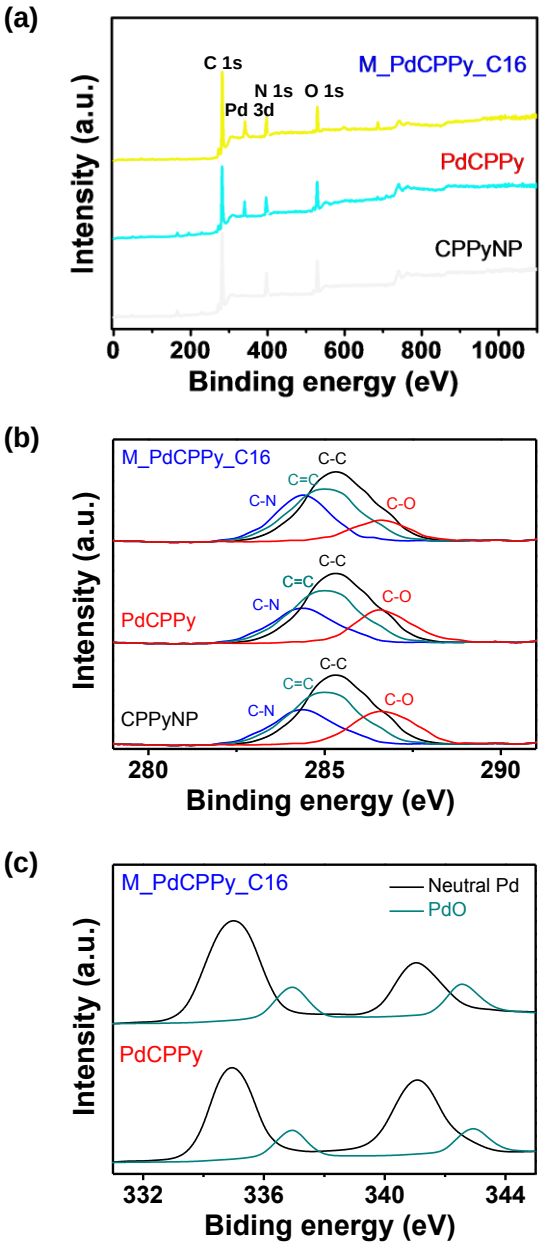

Figure 85. (a) Fully scanned and high resolution of X-ray photoelectron spectroscopy (XPS) with (b) C 1s and (c) Pd 3f of various CPPys. Black, red, and blue represent CPPyNP, PdCPPy, and M-PdCPPy_C16, respectively.

Figure 86 shows the N_2 adsorption/desorption isotherms obtained using the Brunauer-Emmett-Teller (BET) method for the CPPy hybrid nanoparticles. The surface area increased with enhancing decorated amount of porous palladium architecture on the surface as following: 50 m^2 g^{-1} for CPPyNP; 67 m^2 g^{-1} for PdCPPy; 182 m^2 g^{-1} for M_PdCPPy_C6; 215 m^2 g^{-1} for M_PdCPPy_C10; 251 m^2 g^{-1} for M_PdCPPy_C16, respectively. This increase in the surface area was caused by the enhancement metal porous architecture in the structure; specifically, the surface area of M_PdCPPy_C16 was about 5 times larger than that of the CPPyNPs. Therefore, the length of alkyl chain on the CPPy surface has a significant effect on the surface area of the CPPy hybrid nanoparticles, due to the enhancement of the decorated porous palladium structure. Moreover, pore distribution of different CPPy particles was suggested through Basset-Joyner-Halenda (BJH) method as described in Figure 87. The peak at 2.7 nm emerged at M_PdCPPys and increased with enhancing decoration amount of porous palladium structure. Therefore, this peak originated from porous structure caused dramatically increasing surface area of particles.

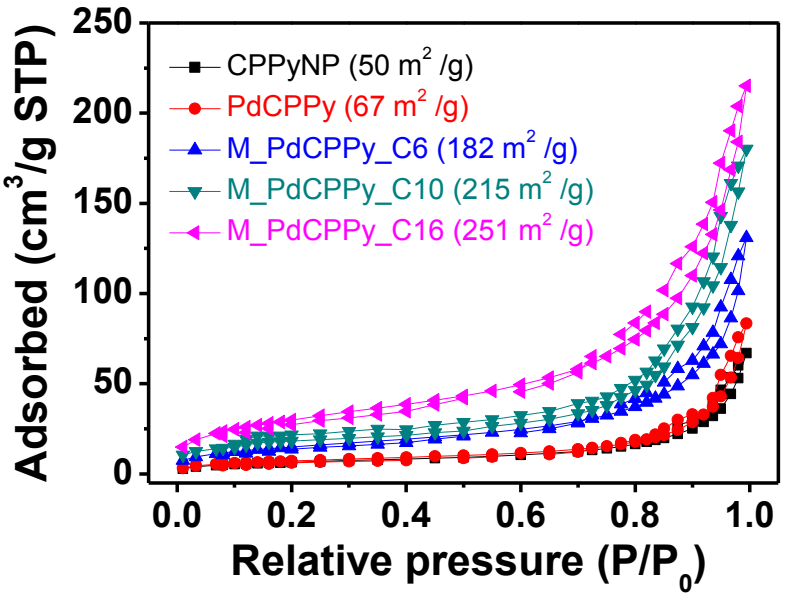

Figure 86. Nitrogen adsorption-desorption isotherm of various hybrid CPPys (CPPyNP: black; PdCPPy: red; M_PdCPPy_C6: blue; M_ PdCPPy_C10: green; M_ PdCPPy_C16: pink).

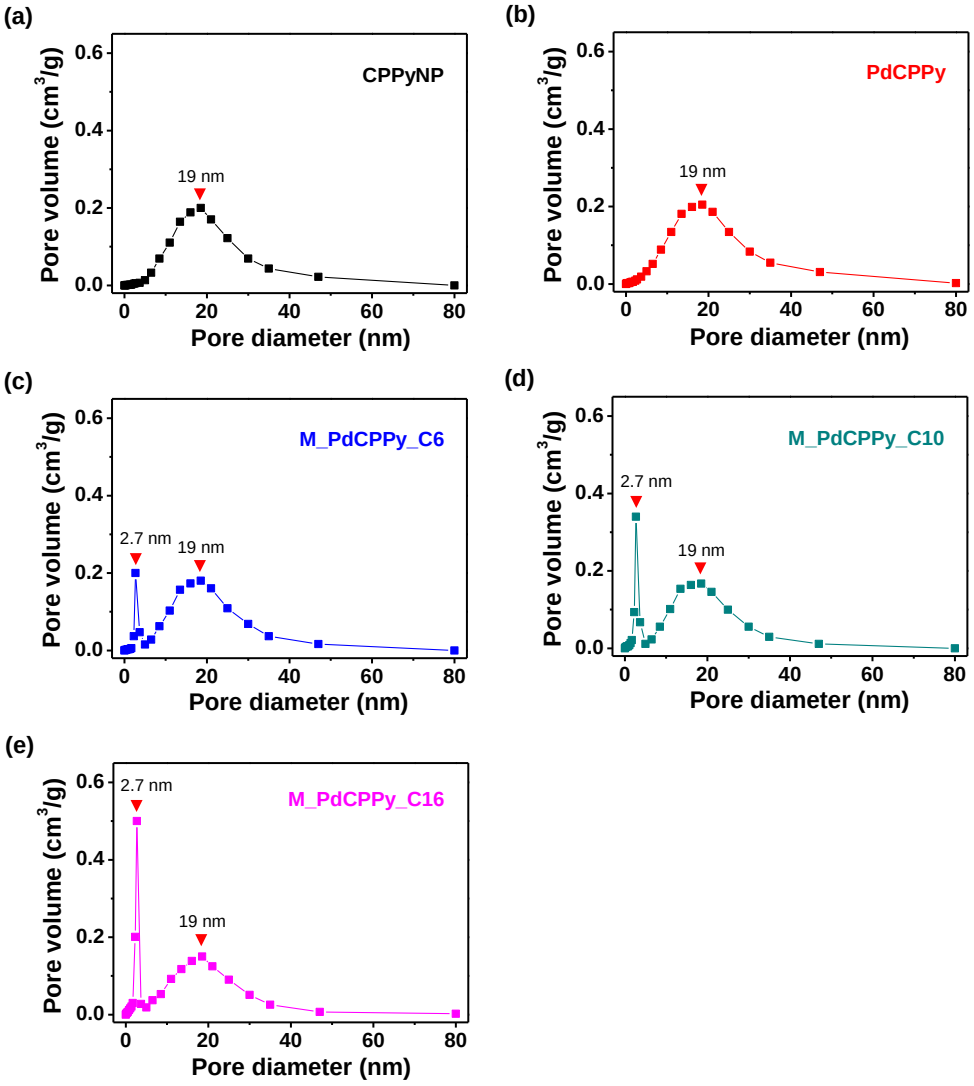

Figure 87. Pore size distribution curves of (a) CPPyNP, (b) PdCPPy, (c) M_PdCPPy_C6, (d) M_PdCPPy_C10, and (e) M_PdCPPy_C16.

3.2.2.2. Application for hydrogen gas chemical sensor

To characterize the electrical properties of CPPy hybrid nanomaterials, the hybrid particles were immobilized on the inter-digitated array (IDA) sensor electrode. Several approaches were explored to optimize the performance of sensor electrode, that is, the uniform conductive pathway and effective surface area. One of deposition methods, spin coating process was used to uniformly deposit hybrid particles, as presented in Figure 88. Figure 89a illustrates the current-voltage (I-V) curves of the hybrid CPPys; the results reveal linearity (*i.e.*, ohmic contact) for voltage range from -0.1 to 0.1 V, as opposed to the nonlinearity exhibition by Schottky barriers with poor electrical contact at the electrode. The dV/dI (= R) values of the electrodes decreased as porous palladium architecture on the CPPy surface owing to palladium enhanced conductivity of CPPyNPs. Additionally, increasing amount of porous palladium layer reduced dV/dI value as demonstrated in Figure 89b.

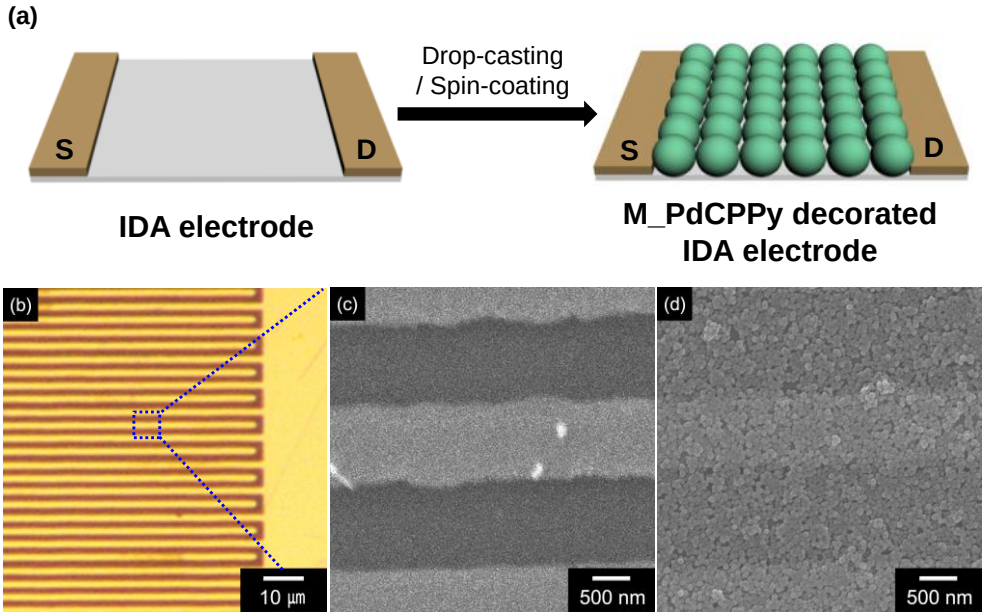

Figure 88. (a) Schematic illustration of inter-digitated array (IDA) electrode and M_PdCPPy deposited electrode by spin-coating method. (b) Optical micrograph and (c) field-emission scanning electron microscope (FE-SEM) images of bare IDA electrode. (d) FE-SEM image of M_PdCPPy deposited IDA electrode.

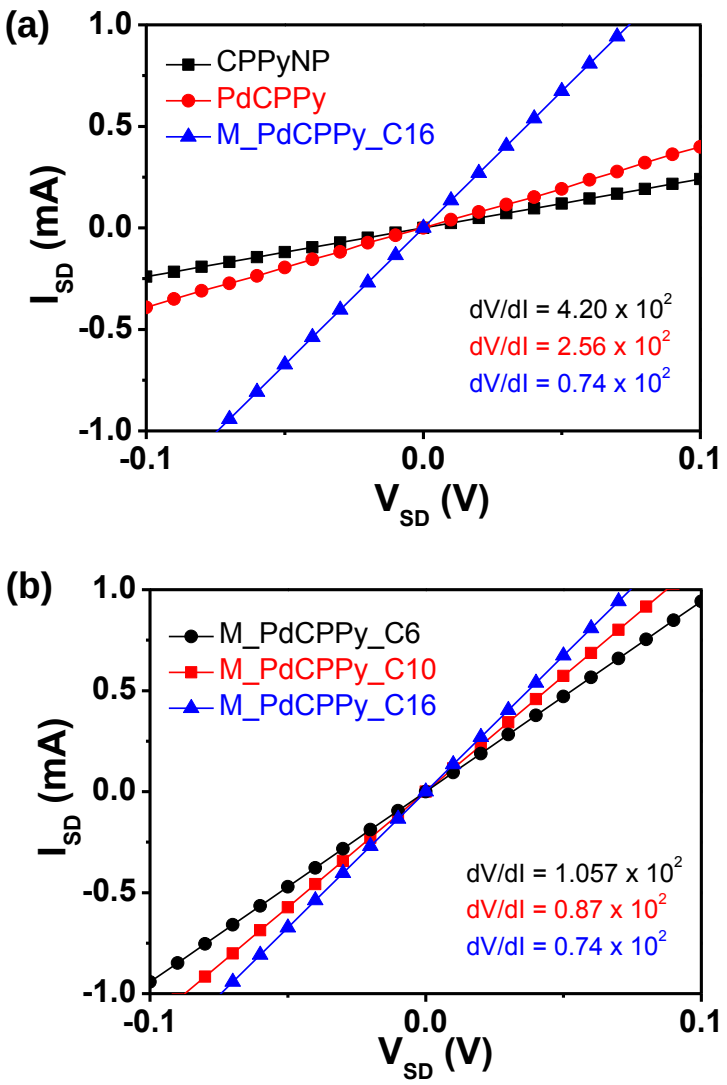

Figure 89. I-V curves of (a) different CPPys (black: CPPyNP; red: PdCPPy; blue: M_PdCPPy_C16) and (b) M_PdCPPys (black: M_PdCPPy_C6; red: M_PdCPPy_C10; blue: M_PdCPPy_C16).

The uniformly dispersed CPPy hybrid particles on the sensor electrode rapidly detected hydrogen gas at room temperature through catalytic chemical reaction between palladium and hydrogen gas (Figure 90). The sensing mechanism of the palladium decorated CPPy hybrid particles is described below. Initially, the hydrogen molecules adsorb to the palladium architectures on the CPPy surface. The two H atoms react with the palladium architectures to form the complex hybrid, PdH_x. The electrons generated move to the CPPy particles due to the lower work function of PdH_x compared with that of CPPy. The transferred electrons decrease the number of holes in the CPPy and increase its electrical resistance (*i.e.*, CPPy acts as a p-type transducer). Thus, the palladium architectures play a key role in hydrogen gas detection in the sensing mechanism. In the sensing mechanism, the palladium architectures bond to the hydrogen gas molecules *via* chemisorption interaction. The number of hydrogen-sensing active sites increases with the enhancing decorated amount of porous palladium layer on the CPPy surface.

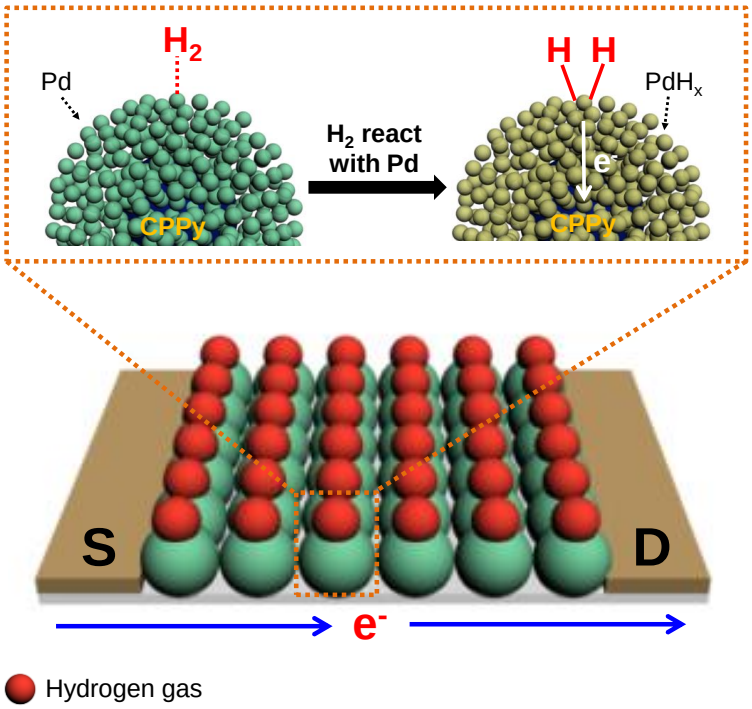

Figure 90. Hydrogen gas detection mechanism of M_PdCPPys at room temperature.

To investigate the sensing characteristics of the M_PdCPPy based sensor electrode, the real-time responsive resist changes were measured for different concentrations of hydrogen gas. Figure 91a shows the real-time response of the different CPPy (CPPyNP, PdCPPy, and M_PdCPPy_C16) based electrodes as a function of hydrogen sensors. Upon each exposure of hydrogen, palladium decorated CPPy (PdCPPy and M_PdCPPy_C16) based electrodes exhibited increasing of resistance rapidly over a 10 s period before its saturated value. However, in the CPPyNP case, there was no response to the hydrogen gas owing to absence of functional sites. The response of the palladium decorated CPPy electrodes increased as decoration of porous palladium architecture; the M_PdCPPy electrode was capable of detecting hydrogen gas as low as 0.1 ppm at room temperature that was the more sensitive than other palladium based materials (Table 6).[221-224] Moreover, real-time response of porous palladium decorated electrodes with different layer thickness was displayed in Figure 91b. The response amount of electrodes increased with enhancing thickness of porous palladium layer due to more active sites on the surface. Therefore, a better sensitive response was achieved with large amount of porous palladium architectures, as a result of the enhancing catalytic activity to the hydrogen gas.

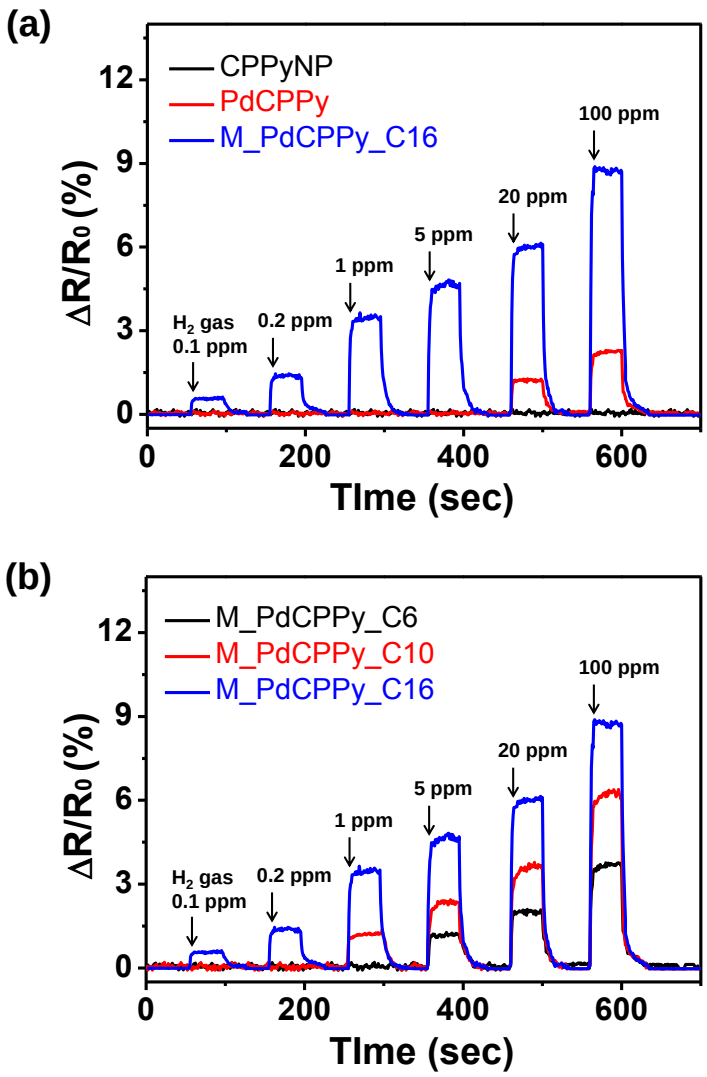

Figure 91. Normalized resistance changes upon sequential exposure to various concentrations of hydrogen: different (a) CPPys (black: CPPyNP; red: PdCPPy; blue: M_PdCPPy_C16) and (b) M_PdCPPys (black: M_PdCPPy_C6; red: M_PdCPPy_C10; blue: M_PdCPPy_C16).

Table 6. Hydrogen gas sensing ability of different palladium based sensing electrodes.

	MDL[a]	Working temperature (℃)	reference
Palladium nanowire	2 ppm	25	[221]
Pd-Au particle	10 ppm	25	[222]
Pd-NiO particle	30 ppm	150	[223]
Palladium film	0.5 vol%	25	[224]
M_PdCPPy_C16	0.1 ppm	25	this work

[a] Minumum detactable level

Figure 92 describes the changes in sensitivity as a function of palladium architecture amount for the hybrid particles, with respect to hydrogen concentration. The sensitivity (S) is determined from the saturation point of the normalized resistance change ($\Delta R/R_0 \times 100$), measured 20 s after the hydrogen exposure. At low concentrations (< 0.1 ppm), the M_PdCPPy sensors displayed nonlinear changes in sensitivity. Linear behavior was observed over a wide range of concentrations (0.1 – 100 ppm). Therefore, the M_PdCPPy based sensor electrodes demonstrated reversible, reproducible responses to different analyte concentrations, and their responses were more pronounced as the gas concentration increased.

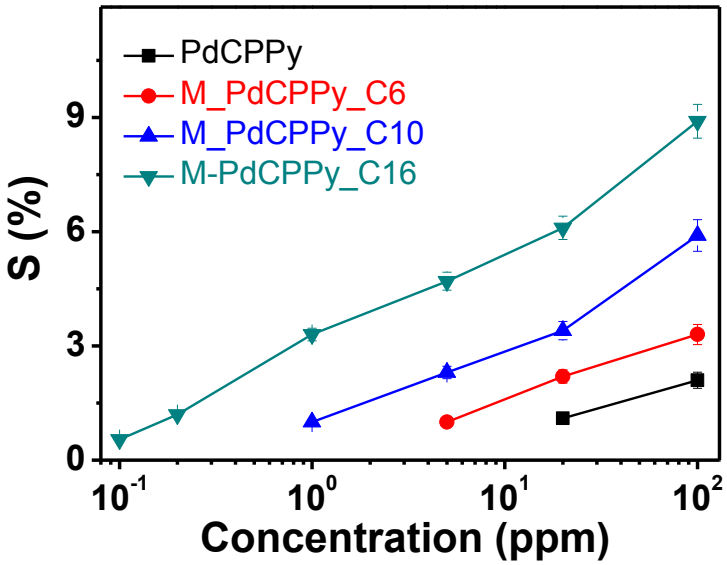

Figure 92. Calibration line as a function of hydrogen gas concentration (black: PdCPPy; red: M_PdCPPy_C6; blue: M_PdCPPy_C10; green: M_PdCPPy_C16).

Superb cycle stability is required for electrode materials in practical implementation of sensor device. Figure 93a presents the electrical response of various hybrid CPPy particles upon periodic exposure to 20 ppm of hydrogen gas at room temperature. With the exception of CPPyNPs, these particles revealed similar response sensitivity during enhanced sensing number without retardation of the response or recovery times. Moreover, hybrid CPPy based sensors maintained their sensing ability after 100 cycle exposure of 20 ppm hydrogen gas (Figure 93b). In addition, the morphology of M_PdCPPys after hydrogen exposure was maintained without collapse of porous palladium layer (Figure 94). During hydrogen detection, the porous structure of palladium layer prevents morphology collapse from phase transition of palladium halide (PdH_x). Therefore, M_PdCPPy based sensor electrodes exhibited highly stable for repetitive hydrogen gas detection.

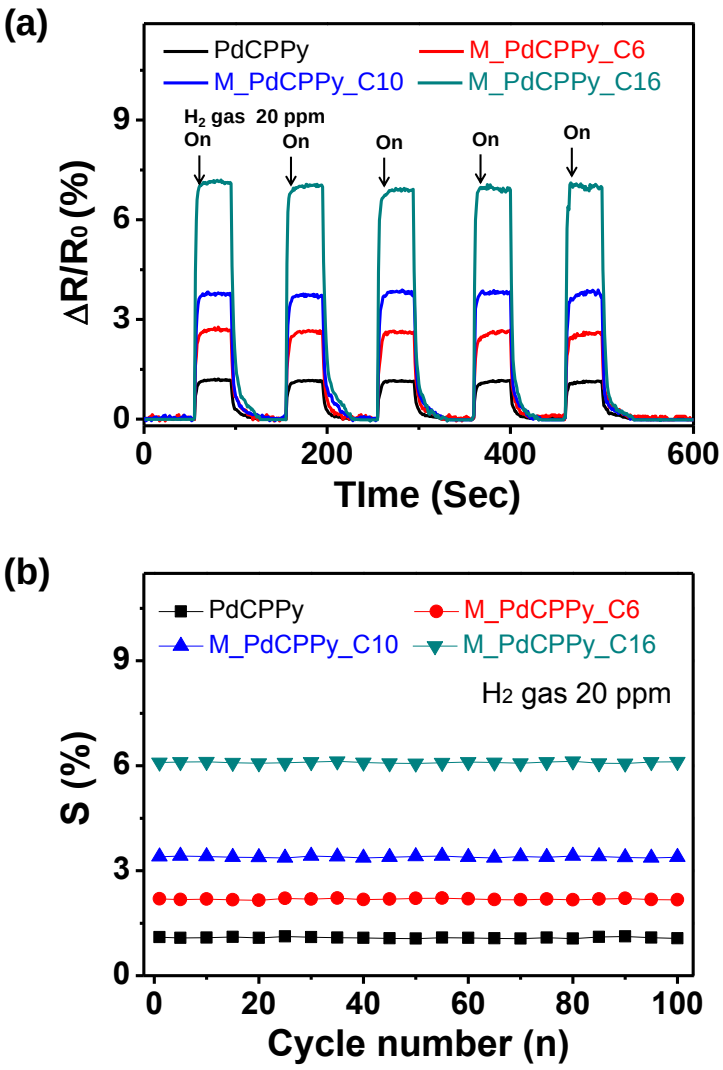

Figure 93. (a) Normalized resistance changes of different hybrid CPPys upon sequential periodic exposure to 20 ppm of hydrogen gas. (b) Sensitivity (S) changes of hybrid CPPys with periodic exposure to 20 ppm of hydrogen gas for 100 times (black: PdCPPy; red: M_PdCPPy_C6; blue: M_PdCPPy_C10; green: M_PdCPPy_C16).

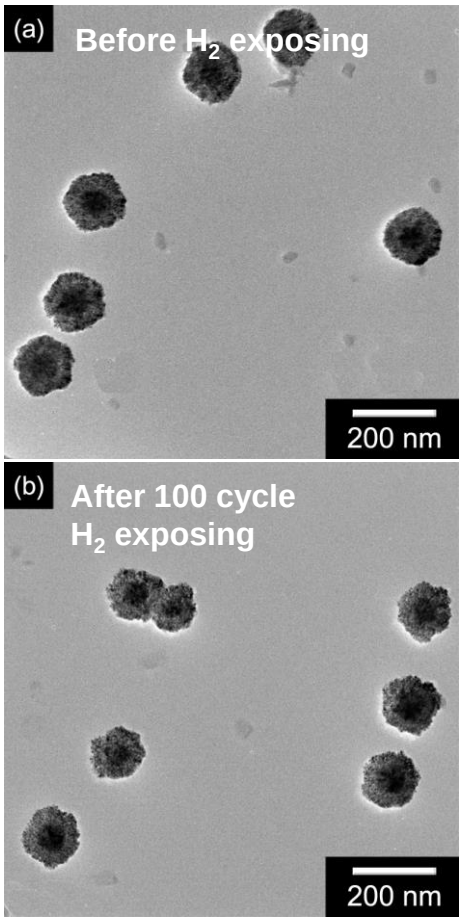

Figure 94. TEM images of M_PdCPPy_C16 (a) before and (b) after exposure to hydrogen gas of 20 ppm for 100 cycles.

4. CONCLUSIONS

The various multidimensional hybrid nanomaterials, composed of metal oxide/conducting polymer or noble metal/conducting polymer, were prepared from the simple and unique methods and the synthesized nanomaterials suggested potential properties in the deiverse sensing areas. The subtopics could be concluded as followings:

1. The multidimensional FeOOH nanoneedle-decorated polypyrrole hybrid nanoparticles (PFFs) were fabricated using a dual-nozzle electrospray technique. During the electrospray process, Fe^{3+} ions uniformly dispersed over the PPy surface; compressed air flow through the inner portion of the dual-nozzle prevented particle aggregation. These E_PPy nanoparticles were collected and converted into FeOOH nucleate sites by reacting with OH^- in the NaOH solution in the collector. E_PPy nanoparticles were stirred in an $FeCl_3$ aqueous solution at 70℃ for 4 h to induce growth of FeOOH needles on the surface. The resulting hybrid PFF nanoparticles were used in a gas sensor for the detection of the nerve agent simulant, DMMP, with ultrahigh sensitivity at room temperature. Enhanced sensitivity was observed as the size and number density of FeOOH needles on the PPy surface increased. In particular, the PFF_10 sensor transducer revealed a minimum detectable level (MDL) of 0.1

ppb compared with higher than other hybrid nanomaterial chemical sensors.

2. The multidimensional urchin-like polypyrrole (U_PPy) hybrid nanoparticles were synthesized using a dual-nozzle electrospray and vapor deposition polymerization (VDP) methods. During the electrospray process, aggregate-free FeOOH nucleated sites were fabricated on the PPy particles (E_PPy). Then, FeOOH nanoneedle-decorated PPy (PFF) particles were formed after heating and stirring. Lastly, U_PPy particles were fabricated using VDP. The resulting U_PPy nanoparticles were highly sensitive to various hazardous vapors. The U_PPy chemical sensor showed 10–100 times greater sensing ability to various vapors than pristine PPy particle sensors. The greatest sensitivity and selectivity were observed for NH_3. In particular, 30 nm diameter U_PPy nanoparticles exhibited an MDL of 0.01 ppm for NH_3, which was higher than that observed for other conducting polymer-based chemical sensors.

3. The multidimensional aptamer-functionalized carboxylated polypyrrole hybrid nanoparticle (A_M_CPPyNP) based-FET sensors were fabricated using electrospray, VDP, and the introduction of a binding aptamer on the surface. The maximized surface area of the M_CPPyNPs enhanced the amount of conjugated BPA-binding aptamers, increasing its affinity for BPA. As a result,

the A_M_CPPyNP FET sensors exhibited ultrahigh sensitivity (～1 fM) to BPA, 10–10^2 times higher than that of other FET sensors. Moreover, the A_M_CPPyNP sensor displayed specific selectivity to the BPA molecule, as well as a long lifetime (4 weeks in this study) with respect to the repeated use of the sensor. The reusability properties of the sensor were attributed to the covalent bonding used in the immobilization process for sensing.

4. The multidimensional platinum/carboxylated hybrid nanoparticle (Pt_CPPy) base-FET sensors were fabricated using chemical reduction and immobilization of the Pt_CPPys on the electrode surface. The decorated Pt particles enhanced oxidation amount of dopamine, increasing sensitivity to dopamine molecules. As a result, the Pt_CPPy FET sensors demonstrated ultrahigh sensitivity (100 fM) to dopamine, 10^2 –10^3 times higher than that of other nonenzyme sensors. Moreover, the Pt_CPPy sensor displayd selectivity to the dopamine molecule, as well as a long lifetime (4 weeks in this study) with respect to the repeated use of the sensor. The reusability properties of the sensor are attributed to the covalent bonding used in the immobilization process and without bioreceptors.

5. The multidimensional porous palladium decorated carboxylated polypyrrole hybrid nanoparticles (M_PdCPPys) were facilely fabricated using alkyl

functionalization and chemical reduction. The decorated thickness of porous palladium layer increased through enhancing alkyl chain length from hexyl (C6) to hexadecyl (C16). The as prepared M_PdCPPys were used in a gas sensor for the detection of the hydrogen gas with ultrahigh sensitivity at room temperature. In particular, porous palladium architecture suggested critical functions in the hydrogen sensing system as following: (1) maximization of active surface area to the hydrogen molecule; (2) maintaining morphology uniformity through phase transition of palladium halide during hydrogen detection. As a result, the M_PdCPPy sensors exhibited a minimum detectable level (MDL) of 0.1 ppm compared with more sensitive than other hybrid nanomaterial chemical sensors. Moreover, it also displayed superb reusability properties to hydrogen gas sensing originated from porous palladium sensing layer.

In summary, five different types of multidimensional metal/conducting polymer nanoparticles were fabricated through facile and unique prodesses. First, iron oxyhydroxide (FeOOH), one of metal oxide, nanoneedle decorated polypyrrole hybrid nanoparticles were synthesized through dual-nozzle electrospray and heat oxidation reaction methods. Then, multidimensional urchin-like polypyrrole hybrid nanoaprticles were formed *via* vapor deposition

polymerization of pyrrole monomer on the FeOOH needle surface. Binding aptamer-functionalized carboxylated polypyrrole nanoparticles were prepared using pyrrole-3-carboxylic acid monomer instead of pyrrole monomer and following catalytic conjugation reaction between carboxyl group and amine group of binding aptamer. Second, two types of noble metal (Pd and Pt) architecture decorated hybrid carboxylated polypyrrole nanoparticles were suggested by facile chemical reduction process. In particular, porous palladium architecture decorated by using alkyl chain functionalization on the carboxylated polypyrrole surface. The as prepared diverse hybrid nanoparticles displayed ultrahigh ability in the chemical/bio sensor application due to its large active surface area originated from multidimensional structure. In addition, these prepared materials can be also utilized in other applications such as energy storage and biotherapy.

References

[1] A. G. MacDiarmid, *Angew. Chem. Int. Ed*. **2001**, *40*, 2581.

[2] H. Shirakawa, *Angew. Chem. Int. Ed*. **2001**, *40*, 2574.

[3] A. J. Heeger, *Angew. Chem. Int. Ed*. **2001**, *40*, 2591.

[4] J. Jang, *Adv. Polym. Sci*. **2006**, *199*, 189.

[5] P. Camurlu, *RSC Adv*. **2014**, *4*, 55832.

[6] E. M. Genies, G. Bidan, *J. Electroanal. Chem*. **1983**, *149*, 101.

[7] J. Jang, J. H. Oh, X. L. Li, *J. Mater. Chem*. **2004**, *14*, 2872.

[8] A. O. Patil, A. J. Heeger, F. Wudl, *Chem. Rev*. **1988**, *88*, 183.

[9] M. Yamaura, T. Hagiwara, K. Iwata, *Synt. Met*. **1988**, *26*, 209.

[10] Q. Q. Zhao, A. Boxman, U. Chowdhry, *J. Nanopart. Res*. **2003**, *5*, 567.

[11] M. Lazzari, M. A. Lopez-Quintela, *Adv. Mater*. **2003**, *15*, 1583.

[12] C. N. R. Rao, A. K. Cheetham, *J. Mater. Chem.* **2001**, *11*, 2887.

[13] V. V. Pokropivny, V. V. Skorohold, *Physica E* **2008**, *40*, 2521.

[14] J. Wang, *Analyst* **2005**, *130*, 421.

[15] A. Erdem, *Talanta* **2007**, *74*, 318.

[16] E. G. Barbagiovanni, D. J. Lockwood, P. J. Simpson, Appl. Phys. Rev. 2014, 1, 011302.

[17] C-C. Chen, S. R. Hwang, W-H. Li, K-C. Lee, G-C. Chi, H-T. Hsiao, C-G. Wu, *Polym. J.* **2002**, *34*, 271.

[18] N. E. Kamchi, B. Belaabed, J-L. Wojkiewicz, S. Lamouri, T. Lasri, *J.*

Appl. Polym. Sci. **2013**, *127*, 4426.

[19] S. Cho, S. H. Hwang, C. Kim, J. Jang, *J. Mater. Chem*. **2012**, *22*, 12164.

[20] M. Rippa, R. Capasso, L. Petti, G. Nenna, A. D. G. D. Mauro, M. G. Maglione, C. Minarini, *J. Mater. Chem. C* **2015**, *3*, 147.

[21] H. Gao, Q. Lu, N. Liu, X. Wang, F. Wang, *J. Mater. Chem. A* **2015**, *3*, 7215.

[22] K-H. Shin, J. Cho, J. Jang, H. S. Jang, E. S. Park, K. Song, S. H. Kim, *Org. Electron*. **2012**, *13*, 715.

[23] H. Yoon, J-Y. Hong, J. Jang, *Small* **2007**, *3*, 1774.

[24] H. Yoon, M. Chang, J. Jang, *Adv. Funct. Mater*. **2007**, *17*, 431.

[25] J. Jang, K. J. Lee, Y. Kim, *Chem. Commun*. **2005**, 3847.

[26] S. Ko, J. Jang, *Angew. Chem. Int. Ed*. **2006**, *45*, 7564.

[27] S-J. Choi, S-M. Park, *Adv. Mater*. **2000**, *12*, 1547.

[28] Y. Yang, M. Wan, *J. Mater. Chem*. **2001**, *11*, 2022.

[29] F. S. Bates, *Science* **1991**, *251*, 898.

[30] D. Zhao, J. Feng, Q. Huo, N. Melosh, G. H. Fredrickson, B. F. Chmelka, G. D. Stucky, *Science* **1998**, *279*, 548.

[31] J. Raez, R. Barjovanu, J. A. Massey, M. A. Winnik, I. Manners, *Angew. Chem. Int. Ed*. **2009**, *39*, 3862.

[32] P. Leclere, A. Calderone, D. Marsitzky, V. Francke, Y. Geerts, K.

Mullen, J. L. Bredas, R. Lazzaroni, *Adv. Mater*. **2000**, *12*, 1042.

[33] I. Manner, *Chem. Commun*. **1999**, 857.

[34] Z. Wei, Z. Zhang, M. Wan, *Langmuir* **2002**, *18*, 917.

[35] H. Qiu, M. Wan, *J. Polym. Sci. A Polym. Chem*. **2001**, *39*, 3485.

[36] M. S. Spector, R. R. Price, J. M. Schnur, *Adv. Mater*. **1999**, *11*, 337.

[37] M. Trau, N. Yao, E. Kim, Y. Xia, G. M. Whitesides, I. A. Aksay, *Nature* **1997**, *390*, 674.

[38] C. T. Kresge, M. E. Leonowicz, W. J. Roth, J. C. Vartuli, J. S. Beck, *Nature* **1992**, *359*, 710.

[39] J. M. Schnur, *Science* **1993**, *262*, 1669.

[40] D. M. Antonelli, *Adv. Mater*. **1999**, *11*, 487.

[41] M. R. Ghadiri, J. R. Granja, L. K. Buehler, *Nature* **1994**, *369*, 301.

[42] J. Huang, S. Nirji, B. H. Weiller, R. B. Kaner, *J. Am. Chem. Soc*. **2003**, *125*, 314.

[43] J. J. Langer, I. Czajkowski, *Adv. Mater. Opts. Electronics* **1997**, *7*, 149.

[44] J. J. Langer, *Adv. Mater. Opts. Electronics* **1999**, *9*, 1.

[45] J. Liu, M. Wan, *J. Mater. Chem*. **2001**, *11*, 404.

[46] S. K. Pillalamarri, F. D. Blum, A. T. Tokuhiro, J. G. Story, M. F. Bertino, *Chem. Mater*. **2005**, *17*, 227.

[47] J. Jang, J. H. Oh, *Adv. Funct. Mater*. **2005**, *15*, 494.

[48] J. Jang, J. H. Oh, *Adv. Mater*. **2003**, *15*, 977.

[49] J. Jang, X. L. Li, J. H. Oh, *Chem. Commun*. **2004**, 794.

[50] J. Jang, J. H. Oh, G. D. Stucky, *Angew. Chem. Int. Ed*. **2002**, *41*, 4016.

[51] J. Jang, J. H. Oh, *Langmuir* **2004**, *20*, 8419.

[52] M. R. Simmons, P. A. Chaloner, S. P. Armes, *Langmuir* **1998**, *14*, 611.

[53] A. Y. Men'shikova, B. M. Shabsel's, T. G. Evseeva, *Russ. J. Appl. Chem*. **2003**, *76*, 822.

[54] A. Zelenev, W. Sonnenberg, E. Matijevic, *Colloid Polym. Sci*. **1998**, *276*, 838.

[55] J-Y. Hong, H. Yoon, J. Jang, *Small* **2010**, *6*, 679.

[56] J. Han, B. Kim, J-Y. Shin, S. Ryu, M. Noh, J. Woo, J-S. Park, Y. Lee, N. Lee, T. Hyeon, D. Choi, B-S. Kim, *ACS Nano* **2015**, *9*, 2805.

[57] H. Li, L. Jiang, Q. Cheng, Y. He, V. Pavlinek, P. Saha, C. Li, *Electrochim. Acta* **2015**, *164*, 252.

[58] Q. Yu, J. Zhu, Z. Xu, X. Huang, *Sensor Actuat. B-Chem*. **2015**, *213*, 27.

[59] W. Lei, W. Min, D. Hui, L. Tun, X. An, *J. Nanosci. Nanotechnol*. **2015**, *15*, 5184.

[60] I. T. Matos, B. Bosch-Santos, G. A. Cabrera-Pasca, A. W. Carbonari, *J. Appl. Phys*. **2015**, *117*, 17D511.

[61] J. G. Lu, P. Chang, Z. Fang, *Mater. Sci. Eng. R* **2006**, *52*, 49.

[62] X. Liu, X. Wu, H. Cao, R. P. H. Chang, *J. Appl. Phys*. **2004**, *95*, 3141.

[63] J. Park, J. Joo, S. G. Kwon, Y. Jang, T. Hyeon, *Angew. Chem. Int. Ed*. **2007**, *46*, 4630.

[64] J. C. Hulteen, C. R. Martin, *J. Mater. Chem*. **1997**, *7*, 1075.

[65] M. J. Zheng, L. D. Zhang, G. H. Li, W. Z. Shen, *Chem. Phys. Lett.* **2002**, *363*, 123.

[66] Y. W. Chen, Y. C. Liu, S. X. Lu, C. S. Xu, C. L. Shao, C. Wang, J. Y. Zhang, T. M. Lu, D. Z. Shen, X. W. Fan, *J. Chem. Phys*. **2005**, *123*, 134701.

[67] D. Zhu, H. Zhy, Y. Zhang, *J. Cryst. Growth* **2003**, *249*, 172.

[68] M-C. Daniel, D. Astruc, *Chem. Rev*. **2004**, *104*, 293.

[69] N. L. Rosi, C. A. Mirkin, *Chem. Rev*. **2005**, *105*, 1547.

[70] J. L. Elechiguerra, J. L. Burt, J. R. Morone, A. Camacho-Bragado, X. Gao, H. H. Lara, M. J. Yacaman, *J. Nanobiotechnol*. **2005**, *3*, 6.

[71] J. Greeley, J. K. Norskov, M. Mavrikakis, *Annu. Rev. Phys. Chem*. **2002**, *53*, 319.

[72] X. Wang, M. Waje, Y. Yan, *J. Electrochem. Soc*. **2004**, *151*, A2183.

[73] M. T. Reetz, E. Westermann, *Angew. Chem. Int. Ed*. **2000**, *39*, 165.

[74] Y. Nishihata, J. Mizuki, T. Akao, H. Tanaka, M. Uenishi, M. Kimura, T. Okamoto, N. Hamada, *Nature* **2002**, *418*, 164.

[75] A. Zuttel, *Mater. Today* **2003**, *6*, 24.

[76] S. Chen, D. L. Carroll, *Nano Lett.* **2002**, *2*, 1003.

[77] G. S. Metraux, C. A. Mirkin, *Adv. Mater.* **2005**, *17*, 412.

[78] R. Jin, C. Cao, E. Hao, G. S. Metraux, G. C. Schatz, C. A. Mirkin, *Nature* **2003**, *425*, 487.

[79] C. A. Jr. Foss, G. L. Hornyak, J. A. Stockert, C. R. Martin, *J. Phys. Chem.* **1994**, *98*, 2963.

[80] R. Jin, S. Egusa, N. F. Scherer, *J. Am. Chem. Soc*. **2004**, *126*, 9900.

[81] S. Zhu, F. Li, C. Du, Y. Fu, *Sens. Actuator B-Chem.* **2008**, *134*, 193.

[82] A. J. Haes, R. P. Van Duyne, *J. Am. Chem. Soc*. **2002**, *124*, 10596.

[83] D. B. Cairns, M. A. Khan, C. Perruchot, A. Riede, S. P. Armes, *Chem. Mater*. **2003**, *15*, 233.

[84] S. F. Lascelles, S. P. Armes, *J. Mater. Chem.* **1997**, *7*, 1339.

[85] Y. Bao, W. An, C. H. Turner, K. M. Krishnan, *Langmuir* **2010**, *26*, 478.

[86] M. Logar, B. Jancar, A. Recnik, D. Suvorov, *Nanotechnology* **2009**, *20*, 275601.

[87] J. Hu, Y. Liu, *Langmuir* **2005**, *21*, 2121.

[88] J. S. Lee, O. S. Kwon, S. J. Park, E. Y. Park, S. A. You, H. Yoon, J. Jang, *ACS Nano* **2011**, *5*, 7992.

[89] G. Yu, X. Xie, L. Pan, Z. Bao, Y. Cui, *Nano Energy* **2013**, *2*, 213.

[90] P. J. Hagrman, D. Hagrman, J. Zubieta, *Angew. Chem. Int. Ed*. **1999**, *38*, 2638.

[91] M. Wright, A. Uddin, *Sol. Energy Mater. Sol. Cells* **2012**, *107*, 87.

[92] L. Chen, Z. Song, G. Liu, J. Qiu, C. Yu, J. Qin, L. Ma, F. Tian, W. Liu, *J. Phys. Chem. Solids* **2013**, *74*, 360.

[93] V. K. Thakur, G. Ding, J. Ma, P. S. Lee, X. Lu, *Adv. Mater*. **2012**, *24*, 4071.

[94] S. Kim, W-K. Oh, Y. S. Jeong, J. Jang, *Adv. Funct. Mater*. **2013**, *23*, 1947.

[95] D. Ma, G. Shi, H. Wang, Q. Zhang, Y. Li, *J. Mater. Chem. A* **2014**, *2*, 13541.

[96] D. H. Shin, J. S. Lee, J. Jun, J. Jang, *J. Mater. Chem. A* **2014**, *2*, 3364.

[97] P. Li, Y. Yang, E. Shi, Q. Shem, Y. Shang, S. Wu, J. Wei, K. Wang, H. Zhu, Q. Yuan, A. Cao, D. Wu, *ACS Appl. Mater. Interfaces* **2014**, *6*, 5228.

[98] L. Wang, L. chen, B. Yan, C. Wang, F. Zhu, X. Jiang, Y. Chao, G. Yang, *J. Mater. Chem. A* **2014**, *2*, 8334.

[99] Kh. Ghanbari, N. Hajheidari, *Anal. Biochem*. **2015**, *473*, 53.

[100] D. W. Hatchett, M. Josowicz, *Chem. Rev*. **2008**, *108*, 746.

[101] Z. Liu, L. Zhang, S. Poyraz, X. Zhang, *Curr. Org. Chem*. **2013**, *17*,

2256.

[102] Y. Li, Y. Wu, B. S. Ong, *J. Am. Chem. Soc*. **2005**, *127*, 3266.

[103] Y. Lu, G. L. Liu, L. P. Lee, *Nano Lett*. **2005**, *5*, 5.

[104] T. Peng, W. Sun, C. Huang, W. Yu, B. Sebo, Z. Dai, S. Guo, X_Z. Zhao, *ACS Appl. Mater. Interfaces* **2014**, *6*, 14.

[105] L. Nicolais, G. Carotenuto, Metal-Polymer Nanocomposites, John Wiley & Sons, 2004, Ch.5.

[106] P. Prins, L. P. Candeias, A. J. J. M. van Breemen, J. Sweelssen, P. T. Herwig, H. F. M. Schoo, L. D. A. Siebbeles, *Adv. Mater*. **2005**, *17*, 718.

[107] S. Porel, S. Singh, S. S. Harsha, D. N.Rao, T. P. Radhakrishnan, *Chem. Mater*. **2005**, *17*, 9.

[108] X. Wang, K. Naka, H. Itoh, S. Park, Y. Chujo, *Chem. Commun*. **2002**, 1300.

[109] V. A. Zinovyeva, M. A. Vorotyntsev, I. Bezverkhyy, Denis Chaumont, J-C. Hierso, *Adv. Funct. Mater*. **2011**, *21*, 1064.

[110] G. A. Shaw, J. S. Trethewey, A. D. Jhonson, W. J. Drugan, W. C. Crone, *Adv. Mater*. **2005**, *17*, 1123.

[111] B. Florinel-Gabridl, *Chemical Sensors and Biosensors: Fundamentals and Applications*, Jhon Wiley & Sons, Inc.: UK, 2012, p576.

[112] A. K. Batra, A. K. Chilvery, P. Guggilla, M. Aggarwal, J. R. Currie, *J.*

Nanosci. Nanotechnol. **2014**, *14*, 2065.

[113] H. Yoon, M. Chang, J. Jang, *J. Phys. Chem. B* **2006**, *110*, 14074.

[114] S. Ko, J. Jang, *Biomacromolecules* **2007**, *8*, 182.

[115] O. S. Kwon, S. J. Park, H. Yoon, J. Jang, *Chem. Commun*. **2012**, *48*, 10526.

[116] C. M. Hangarter, N. Chartuprayoon, S. C. Hernandez, Y. Choa, N. V. Myung, *Nano Taday* **2013**, *8*, 39.

[117] H. Yoon, J. Jang, *Adv. Funct. Mater*. **2009**, *19*, 1567.

[118] E. Park, O. S. Kwon, S. J. Park, J. S. Lee, S. You, J. Jang, *J. Mater. Chem*. **2012**, *22*, 1521.

[119] V. Pavlov, Y. Xiao, I. Willner, *Nano Lett*. **2005**, *5*, 649.

[120] S. Royo, R. Martinez-Manez, F. Sancenon, A. M. Costero, M. Parra, S. Gil, *Chem. Commun*. **2007**, 4839.

[121] S. Cho, O. S. Kwon, S. A. you, J. Jang, *J. Mater. Chem. A* **2013**, *1*, 5679.

[122] T. J. Dale, J. Rebek, *Angew. Chem. Int. Ed*. **2009**, *48*, 7850.

[123] X. Ji, J. Zheng, J. Xu, V. K. Rastogi, T-C. Cheng, J. J. Defrank, R. M. Leblanc, *J. Phys. Chem. B* **2005**, *109*, 3793.

[124] C. Hartmann-Thompson, J. Hu, S. N. Kaganove, S. E. Keinath, D. L. Keeley, P. R. Dvornic, *Chem. Mater*. **2004**, *16*, 5357.

[125] F. Wang, H. Gu, T. M. Swager, *J. Am. Chem. Soc*. **2008**, *130*, 5392.

[126] E. S. Snow, F. K. Perkins, E. J. Houser, S. C. Badescu, T. L. Reinecke, *Science* **2005**, *307*, 1942.

[127] K. Wetchakun, T. Samerjai, N. Tamaekong, C. Liewhiran, C. Siriwong, V. Kruefu, A. Wisitsoraat, A. Tuantranont, S. Phanichphant, *Sens. Actuator B-Chem*. **2011**, *160*, 580.

[128] J. Jang, M. Chang, H. Yoon, *Adv. Mater*. **2005**, *17*, 1616.

[129] N. S. Ramgir, Y. Yang, M. Zacharias, *Small* **2010**, *6*, 1705.

[130] G. Xiao, Y. Zeng, Y. Jiang, J. Ning, W. Zheng, B. Liu, X. Chen, G. Zou, B. Zou, *Small* **2013**, *9*, 793.

[131] J. S. Lee, O. S. Kwon, D. H. Shin, J. Jang, *J. Mater. Chem. A* **2013**, *1*, 9099.

[132] L. Shi, A. J. T. Naik, J. B. M. Goodall, C. Tighe, R. Gruar, R. Binions, I. Parkin, J. Darr, *Langmuir* **2013**, *29*, 10603.

[133] G. Mattei, P. Mazzoldi, M. L. Post, D. Buso, M. Guglielmi, A. Martucci, *Adv. Mater*. **2007**, *19*, 561.

[134] T. Fu, *Electrochim. Acta* **2013**, *112*, 230.

[135] S. Mikhaylov, N. Ogurtsov, Y. Noskov, N. Redon, P. Coddeville, J.-L. Wojkiewicz, A. Pud, *RSC Adv.* **2015**, *5*, 20218.

[136] Y-L. Tang, Z-J. Li, J-Y. Ma, H-Q. Su, Y-J. Guo, L. Wang, B. Du, J-J.

Chen, W. Zhou, Q-K. Yu, Z-T. Zu, *J. Hazard. Mater*. **2014**, *280*, 127.

[137] G. N. Chaudhari, S. V. Jagtap, N. N. Gedam, M. J. Pawar, V. S. Sangawar, *Talanta* **2009**, *78*, 1136.

[138] N. V. Hieu, L. T. B. Thuy, N. D. Chien, *Sens. Actuator B-Chem*. **2008**, *129*, 888.

[139] G. Korotcenkov, S. D. Han, J. R. Stetter, *Chem. Rev*. **2009**, *109*, 1402.

[140] S. K. Arya, S. Krishnan, H. Silva, S. Jean, S. Bhansali, *Analyst* **2012**, *137*, 2743.

[141] Y. H. Hu, L. Zhang, *Adv. Mater*. **2010**, *22*, E117.

[142] J. L. Johnson, A. Behnam, S. J. Pearton, A. Ural, *Adv. Mater*. **2010**, *22*, 4877.

[143] C. Fournier, K. Rajoua, M-L. Doublet, F. Favier, *ACS Appl. Mater. Interfaces* **2013**, *5*, 310.

[144] M. Yang, J. Dai, *Photonic Sensors* **2014**, *4*, 300.

[145] X. Chen, G. Wu, Z. Cai, M. Oyama, X. Chen, *Microchim. Acta* **2014**, *181*, 689.

[146] O. A. Sadik, *Electroanalysis* **1999**, *11*, 839.

[147] K-I. Chen, B-R. Li, Y-T. Chen, *Nano Today* **2011**, *6*, 131.

[148] L. Liu, Q. Ma, Y. Li, Z. Liu, X. Su, *Biosens. Bioelectron*. **2015**, *63*, 519.

[149] B. N. Johnson, R. Mutharasan, *Analyst* **2014**, *139*, 1576.

[150] K. Ariga, Q. Ji, T. Mori, M. Naito, Y. Yamauchi, H. Abe, J. P. Hill, *Chem. Soc. Rev.* **2013**, *42*, 6322.

[151] M. Ates, *Mater. Sci. and Engin. C* **2013**, *33*, 1853.

[152] J. A. Hagen, S. N. Kim, B. Bayraktaroglu, K. Leedy, J. L. Chavez, N. Kelley-Loughnane, R. R. Naik, M. O. Stone, *Sensors* **2011**, *11*, 6645.

[153] J-I. Hahm, *Sensors* **2011**, *11*, 3327.

[154] E. Lahiff, C. Lynam, N. Gilmartin, R. O'Kennedy, D. Diamond, *Anal. Bioanal. Chem.* **2010**, *398*, 1575.

[155] O. S. Kwon, T-J. Hong, S. K. Kim, J-H. Jeong, J-S. Hahn, J. Jang, *Biosens. Bioelectron*. **2010**, *25*, 1307.

[156] A. K. Wanekaya, M. A. Bangar, M. Yun, W. Chen, N. V. Myung, A. Mulchandani, *J. Phys. Chem. C* **2007**, *111*, 5218.

[157] J. Jang, J. Bae, M. Choi, S-H. Yoon, *Carbon* **2005**, *43*, 2730.

[158] H. Yoon, J-H. Kim,N. Lee, B-G. Kim, J. Jang, *ChemBioChem* **2008**, *9*, 634.

[159] H. Yoon, S. H. Lee, O. S. Kwon, H. S. Song, E. H. Oh, T. H. Park, J. Jang, *Angew. Chem. Int. Ed*. **2009**, *48*, 2755.

[160] S. M. Rappaport, M. T. Smith, *Science* **2010**, *330*, 460.

[161] S. Boue, H. D. Leon, W. K. Schlage, M. J. Peck, H. Weiler, A. Berges, G. Vuillaume, F. Martin, B. Friedrichs, S. Lebrun, *Toxicology* **2013**,

314, 112.

[162] A. F. Hernandez, F. Gil, M. Lacasana, M. Rodriguez-Barranco, A. Gomez-Martin, D. Lozano, A. Pla, *Food Chem. Toxicol.* **2013**, *61*, 164.

[163] D. E. Vidal-Dorsch, R. C. Colli-Dula, S. M. Bay, D. J. Greenstein, L. Wiborg, D. Petschauer, N. D. Denslow, *Environ. Sci. Technol.* **2013**, *47*, 11268.

[164] R. Chalasani, S. Vasudevan, *ACS Nano* **2013**, *7*, 4093.

[165] M. P. Leese, F. Jourdan, W. Dohle, M. R. Kimberley, M. P. Thomas, R. Bai, E. Hamel, E. Ferrandis, B. V. L. Potter, *ACS Med. Chem. Lett.* **2012**, *3*, 5.

[166] H. Kuang, H. Yin, L. Liu, L. Xu, W. Ma, C. Xu, *ACS Appl. Mater. Inter.* **2014**, *6*, 364.

[167] S. Hansen, C.-M. Lehr, U. F. Schaefer, *Adv. Drug Deliver. Rev.***2013**, *65*, 251.

[168] N. V. Tusar, D. Maucec, M. Rangus, I. Arcon, M. Mazaj, M. Cotman, A. Pintar, V. Kaucic, *Adv. Funct. Mater.* **2012**, *22*, 820.

[169] Yamada, M.; Kato, K.; Shindo, K.; Namizu, M.; Haruki, M.; Sakairi, N.; Ohkawa, K.; Yamamoto, H.; Noshi, N. *Biomaterials* **2001**, *22*, 3121.

[170] A. Ballesteros-Gomez, S. Rubio, D. Perez-Bendito, *J. Chromatogr. A* **2009**, *1216*, 449.

[171] J.-H. Kang, F. Kondo, Y. Katayama, *Toxicology* **2006**, *226*, 79.

[172] H. H. Le, E. M. Carlson, J. P. Chua, S. M. Belcher, *Toxicol. Lett.* **2008**, *176*, 149.

[173] R. S. J. Alkasir, M. Ganesana,; Y.-H. Won, L. Stanciu, S. Andreescu, *Biosens. Bioelectron.* **2010**, *26*, 43.

[174] W. Dekant, W. Volkel, *Toxicol. Appl. Pharm.* **2008**, *228*, 114.

[175] Z. Mei, H. Chu, W. Chen, F. Xue, J. Liu, H. Xu, R. Zhang, L. Zheng, *Biosens. Bioelectron.* **2013**, *39*, 26.

[176] S. Salian, T. Doshi, G. Vanage, *Reprod. Toxicol.* **2011**, *31*, 359.

[177] Z. C. Sanchez-Acevedo, J. Riu, F. X. Rius, *Biosens. Bioelectron.* **2009**, *24*, 2842.

[178] K. V. Ragavan, L. S. Selvakkumar, M. S. Thakur, *Chem. Commun.* **2013**, *49*, 5960.

[179] S. Jiao, J. Jun, L. Wang, *Talanta*, **2014**, *122*, 140.

[180] M. Jo, J-Y. Ahn, J. Lee, S. Lee, W. Hong, J-W. Yoo, J. Kang, P. Dua, D-K. Lee, S. Hong, S. Kim, *Oligonucleotides*, **2011**, *21*, 85.

[181] K. Inoun, K. Kato, Y. Yoshimura, T. Makino, H. Nakazawa, *J. Chromatogr. B* **2000**, *749*, 17.

[182] Y. Watabe, T. Kondo, M. Morita, N. Tanaka, J. Haginaka, K. Hosoya, *J. Chromatogr. A* **2004**, *1032*, 45.

[183] N. Kuroda, Y. Kinoshita, Y. Sun, M. Wada, N. Kishikawa, K. Nakashima, T. Makino, H. Nakazawa, *J. Pharmaceut. Biomed.* **2003**, *30*, 1743.

[184] A. D. Ellington, J. W. Szostak, *Nature* **1990**, *346*, 818.

[185] C. Tuerk, L. Gold, *Science* **1990**, *249*, 505.

[186] O. S. Kwon, S. J. Park, J. Jang, *Biomaterials* **2010**, *31*, 4740.

[187] O. S. Kwon, S. J. Park, J-Y. Hong, A-R. Han, J. S. Lee, J. S. Lee, J. H. Oh, J. Jang, *ACS Nano* **2012**, *6*, 1486.

[188] J. H. An, S. J. Park, O. S. Kwon, J. Bae, J. Jang, *ACS Nano* **2013**, *7*, 10563.

[189] K. Muteryka, *Biosens. Bioelectron.* **2014**, *54*, 393.

[190] T. Pradhan, H. S. Jung, J. H. Jang, T. W. Kim, C. Kang, J. S. Kim, **2014**, *43*, 4684.

[191] T. C. Sudhof, *Neuron* **2013**, *80*, 675.

[192] D. L. Robinson, B. J. Venton, M. L. A. V. Heien, R. M. Wightman, *Clin. Chem.* **2003**, *49*, 1763.

[193] F. Mora, S. Segorio, A. D. Arco, M. D. Blas, P. Garrido, *Brain Res.* **2012**, *1476*, 71.

[194] V. Hefco, K. Yamada, A. Hefco, L. Hritcu, A. Tiron, T. Nabeshima, *Eur. J. Pharmacol*. **2003**, *475*, 55.

[195] B. E. K. Swmara, B. J. Venton, *Analyst*, **2007**, *132*, 876.

[196] K. Jackowska, P. Krysinski, *Anal. Bioanal. Chem.* **2013**, *405*, 3753.

[197] A. Galvan, T. Wichmann, *Clin. Neurophysiol*. **2008**, *119*, 1459.

[198] J. M. Swanson, N. D. Volkow, *J. Child Psycol. Psychiatry* **2009**, *50*, 180.

[199] J. S. Markowitz, A. B. Straughn, K. S. Patrick, *Pharmacotherapy* **2003**, *23*, 1281.

[200] J. W. Dalley, J. P. Roiser, *Neuroscience* **2012**, *215*, 42.

[201] E. Baldrich, R. Gomez, G. Gabriel, F. X. Munoz, *Biosens. Bioelectron.* **2011**, *26*, 1876.

[202] M. Marinelli, J. E. Mccutcheon, *Neuroscience* **2014**, *28*, 176.

[203] J-M. Beaulieu, *J. Psychiatry Neurosci*. **2012**, *37*, 7.

[204] J. Zheng, X. Zhou, *Bioelectrochemistry* **2007**, *70*, 408.

[205] N. F. Atta, M. F. El-Kady, *Sens. Actuator B-Chem.* **2010**, *145*, 299.

[206] N. Ye, T. Gao, J. Li, *Anal. Methods* **2014**, *6*, 7518.

[207] A. El-Beqqali, A. Kussak, M. Abdel-Rehim, *J. Sep. Sci*. **2007**, *30*, 421.

[208] B-R. Li, Y-J. Hsieh, Y-X. Chen, Y-T. Chung, C-Y. Pan, Y-T. Chen, *J. Am. Chem. Soc.* **2013**, *135*, 16034.

[209] W-S. Li, P-X. Hou, C. Liu, D-M. Sun, J. Yuan, S-Y. Zhao, L-C. Yin, H. Cong, H-M. Cheng, *ACS Nano* **2013**, *7*, 6831.

[210] T. J. Castilho, A. D. P. T. Sotomayor, L. T. Kubota, *J. Pharm. Biomed. Anal*. **2005**, *37*, 785.

[211] L. Stoica, A. Lindgren-Sjolander, T. Ruzgas, L. Gorton, *Anal. Chem*. **2004**, *76*, 4690.

[212] S. J. Park, H. S. Song, O. S. Kwon, J. H. Chung, S. H. Lee, J. H. An, S. R. Ahn, J. E. Lee, H. Yoon, T. H. Park, J. Jang, *Sci. Rep*. **2014**, *4*, 4342.

[213] H.-M. Xiao, W.-D. Zhang, S.-Y. Fu, *Compos. Sci. Technol*. **2010**, *70*, 909.

[214] B. Tang, C. Wang, L. Zhuo, J. Ge, L. Cui, *Inorg. Chem*. **2006**, *45*, 5196.

[215] T. A. Ho, T.-S. Jun, Y. S. Kim, *Sens. Actuators, B* **2013**, *185*, 523.

[216] S. J. Park, O. S. Kwon, J. Jang, *Chem. Commun*. **2013**, *49*, 4673.

[217] O. S. Kwon, J.-Y. Hong, S. J. Park, Y. Jang, J. Jang, *J. Phys. Chem. C* **2010**, *114*, 18874.

[218] L. Wetchakun, T. Samerjai, N. Tamaekong, C. Liewhiran, C. Siriwong, V. Kruefu, A. Wisitsoraat, A. Tuantranont, S. Phanichphant, *Sens. Actuators B* **2011**, *160*, 580.

[219] R. Rezg, S. El-Fazaa, N. Gharbi, B. Mornagui, *Environ. Int*. **2014**, *64*, **83**.

[220] L. Qiu, B. Liu, Y. Peng, F. Yan, *Chem. Commun*. **2011**, *47*, 2934.

[221] F. Yang, D. K. Taggart, R. M. Penner, *Nano Lett*. **2009**, *9*, 2177.

[222] T. Shegai, P. Johansson, C. Langhammer, M. Kall, *Nano Lett*. **2012**, *12*, 2464

[223] P. V. Tong, N. D. Hoa, N. V. Duy, V. V. Quang, N. T. Lam, N. V. Hieu, *Int. J. Hydrog. Energy* **2013**, *38*, 12090.

[224] J. Lee, W. Shim, E. Lee, J-S. Noh, W. Lee, *Angew. Chem. Int. Ed*. **2011**, *50*, 5301.

초 록

최근 우수한 물성과 성능을 보이는 새로운 물질의 개발이 재료과학분야에서 활발하게 진행되고 있다. 특히 무기물과 유기물이 공존하는 복합나노재료는 각 성분물질의 상호작용으로 인하여 우수한 물성을 보일 뿐만 아니라 경제적, 환경적 요구에 부합하여 산업분야에서 많은 연구가 진행중이다. 그 중 금속을 포함한 고분자 복합 나노물질은 에너지 저장 시스템, 촉매, 센서 등 다방면에서 주목을 받고있고 실제로 많은 연구가 수행중이다. 현재 진행중인 나노복합재료에 관한 연구는 다양한 조합의 무기물/고분자 나노재료를 만드는 것으로, 복합 나노물질의 모양 조절에 따른 표면적 향상을 통한 물질성능의 극대화에 대한 연구는 미진한 실정이다.

본 학위 논문에서는 전도성 고분자의 일종인 폴리피롤 나노입자위에 귀금속 또는 금속산화물 나노구조물이 올라간 다양한 다차원 구조의 하이브리드 복합 나노재료를 간단하고 창의적인 방법을 이용하여 제조하고, 이들의 전기적 물성을 체계적으로 고찰하여 센서용 트랜스듀서로 적용하는 연구를 기술하였다. 우선, 금속산화물의 일종인 산화수산화철 나노침상이 올라간 폴리피롤 나노입자를 듀얼노즐 전기방사와 열적 산화반응을 이용하여 제조하였고 이를

신경 유도체인 디메틸 메틸포스포네이트 분자 검출용 화학센서 트랜스듀서로 적용하였다. 또한, 상기 산화수산화철 나노침상 표면에 폴리피롤 단량체를 기상으로 도입하여 성게모양의 다차원적 폴리피롤 나노입자를 제조하였고, 침상으로 인하여 암모니아와 메탄올등 유해한 가스를 검출하는 화학센서 트랜스듀서로 적용하였다. 뿐만 아니라, 산화수산화철 나노침상위에 관능기를 가지는 폴리피롤 단량체를 기상으로 도입하여 관능기를 가지는 다차원적 폴리피롤 나노입자를 제조하고, 환경호르몬 결합압타머를 도입하여 환경호르몬의 일종인 비스페놀 A 검출을 위한 전계효과 트랜지스터 바이오센서를 제작하였다. 두번째로, 귀금속의 일종인 백금 나노입자가 부착된 다차원적 폴리피롤 나노입자를 관능기를 가지는 폴리피롤 나노입자가 분산된 백금나노입자 전구체 수용액의 화학적 환원을 이용하여 제조하였으며, 신경전달 물질중의 하나인 도파민에 대한 비표지식 액체 이온 게이트 전계효과 트랜지스터 센서로 적용하였다. 그 밖에, 상기 방법을 확장하여 관능기를 가지는 폴리피롤 나노입자위에 화학반응을 이용하여 작용기의 길이를 확장한 후, 팔라듐 전구체 수용액과 혼합하여 화학적 환원과정을 이용하여 다공성 팔라듐셀이 부착된 폴리피롤 나노입자를 제조하여 수소가스 측정용 화학센서 트랜스듀서로 적용하였다.

본 학위논문에서는 표면적이 극대화된 다양한 다차원적 구조의

복합나노재료를 제조하고 이를 화학 및 바이오센서로 응용하는 가능성에 대한 연구를 수행하였다. 본 학위논문에서 제조된 나노물질들은 화학가스센서, 전계효과 트랜지스터 압타머 센서, 비표지식 바이오센서 등 다양한 센서 시스템에 응용이 가능하며, 간단하고 독창적인 제조방법들은 다양한 나노 물질의 제조에도 사용될 수 있을 것으로 기대된다.

주요어: 전도성 고분자; 무기물; 귀금속; 금속산화물; 나노복합재료; 센서; 수소; 신경가스유도체; 도파민; 환경호르몬

학 번: 2010-24101